Research Activities

Several-MeV gamma-ray generation at NewSUBARU by laser Compton backscattering

S.Amano[1], K.Horikawa[1], S.Miyamoto[1], T.Hayakawa[2], T.Shizuma[2], T.Mochizuki[1]
LASTI / UH[1], [a)]JAEA[2]

Abstract

A new laser Compton gamma ray source in the energy range of several MeV was developed using a CO_2 laser at the NewSUBARU electron storage ring. When the electron energies were 974, 1220 and 1460 MeV, the maximum gamma ray energies were measured to be 1.72, 2.72, and 3.91 MeV. The luminosity of the gamma rays was 7300 photon/mA/W/s and a flux of $5.8x10^6$ photon/s was achieved. A gamma beam divergence of 0.5 mrad and its pattern were also measured. These performances agreed with calculations. This generation of gamma rays is in a no-loss mode for the storage electrons, and the maximum flux was limited only by the power of the laser. A flux of up to 10^{11} photon/s will be achieved using a 30 kW class CO_2 laser. Several MeV gamma ray sources at NewSUBARU are capable of generating such high power.

Introduction

A Laser Compton gamma ray beam is a very unique light source having the positive characteristics of tunable energy, quasi-monochromaticity, tunable polarization and beam directivity. It is generated by backward Compton scattering with relativistic electrons and photons. The gamma rays have been generated at several high-energy-electron-accelerating facilities around the world. Gamma photon energies ranged from several MeV to several GeV, depending on the electron energy at each facility. Gamma rays in the energy range of a few tens MeV are useful in the study of nuclear physics. Although the peak energy of giant resonance mildly depends on the atomic mass of the targets' nuclei, it is around 15-25 MeV. The NewSUBARU electron storage ring is suitable for producing this energy gamma ray because its electron energy condition allows for the use of a Nd-doped laser having a wavelength of 1.064 μm and such a laser has been developed for stable and high-power operation. With NewSUBARU operating at an electron energy of 1-1.5 GeV, laser Compton gamma rays of 17-34 MeV have been successfully generated using a commercial Nd:YVO_4 laser with wavelengths of 1.064 μm and 0.532 μm. The gamma ray is used in various studies: nuclear physics, nuclear astrophysics, nuclear transmutation and CT-imaging for industrial applications.

Several applications, however, demand gamma ray energies of several MeV. For example, gamma rays of 1-4MeV are useful in studies of nuclear structures using the nuclear resonance fluorescence (NRF) measurement technique. Using the polarized gamma ray beam, we can determine the parity of excited states of nuclei. In addition, these gamma rays are used in studying a nondestructive assay of materials hidden by heavy shields. For these applications, we have expanded the energy range of the gamma ray using a CO_2 laser with a wavelength of 10.52 μm. The CO_2 laser is also capable of operating in a high-power region. A new transport system transmitting the CO_2 laser was added and a focusing optic in it was designed to have a collision point different from that of the Nd-doped laser. The gamma ray produced by the CO_2 laser demonstrated an energy range of 1-4 MeV and flux of $5x10^6$ photon/s in testing; this was consistent with the designed values. The gamma ray flux can be increased easily using a higher powered CO_2 laser. It is easy to generate a high flux gamma ray in the range of several to a few tens MeV because a high-powered Nd-doped laser and CO_2 laser can be used with NewSUBARU operating at an electron energy around 1 GeV.

Experiments

The NewSUBARU ring has two long straight sections of 14 m and its whole shape resembles a racetrack with a circumference of 119 m. Laser Compton scattering experiments were conducted for one of the straight sections combined with beam line 1 (BL 1). (Fig.1).

A laser was set in the experimental hall and its beam was introduced by mirrors inside a shield tunnel into a vacuum tube of the ring through a focusing lens. The laser beam was bent by a mirror inside the tube and collided head-on into an electron beam. The gamma ray was scattered only in the direction of the electron beam and was extracted from the shield tunnel into a shielding hutch. The extracted gamma ray beams were measured by NaI and a Ge detector in the hutch.

The CO_2 laser beam passing through the new beam transport system was scattered by relativistic electrons in NewSUBARU and gamma rays were generated. For this experiment, the incident laser power and electron beam current were set to 1 W and 1-2 mA, respectively. Energy of the gamma ray was measured by a Ge detector (64 mm ϕ x 60 mm) with a high energy-resolution and the flux was measured by a NaI scintillation counter (5 inch ϕ x 5 inch) with relatively high absorption. Signals from these detectors were processed by a multi-channel analyzer and energy channels were calibrated absolutely using radioisotopes of Co-60, K-40, Y-88, and Tl-208.

Results and Discussions

The energy spectra measured by the Ge detector at electron energies E_e of 974, 1220, and 1460 MeV are shown in Fig.3. There was a lead collimator with a 3 mm ϕ hole in the front of the detector, 8.6 m from the collision point. It should be noted these spectra represent the convolution of the detector response function with the gamma ray energy distribution. As the full-energy peaks are visible in Fig.1, we determined the maximum energies at electron energies E_e of 974, 1220 and 1460 MeV to be 1.72, 2.72, and 3.91 MeV, respectively. These energies are in agreement with values calculated.

The flux of the gamma ray can be obtained by integrating the energy spectrum measured by the NaI scintillation counter. Absorption efficiencies in this energy range of the counter were calculated to be 94-80% using XCOM software. Taking account of these efficiencies, the flux and luminosity were obtained. The luminosity at the electron energies E_e of 974, 1220 and 1460 MeV was measured to be 7300 photon/W/mA/s without a collimator. When the 3mm φ collimator was inserted, the luminosity became to 480 (1.5-1.7MeV), 530 (2.3-2.7MeV) and 890 (3.1-3.9MeV) photon/W/mA/s at each electron energy level. Taking into account the attenuation of photons by several media and the tolerance of the laser beam alignment, we calculated these luminosities to be 7000 photon/W/mA/s without a collimator, 500 (1.5-1.7MeV), 750 (2.3-2.7 MeV) and 1000 (3.1-3.9 MeV) photon/W/mA/s with the collimator. When the collimator was used, the luminosities increased with increasing electron energy because the gamma beam divergence (1/γ) decreased.

If we use a 30 kW power CO_2 laser at NewSUBARU with a current of 500 mA, a high flux gamma ray of ~10^{11} photons/s is achieved in several-MeV energy ranges. Even if such high flux gamma rays are generated, the operation of the NewSUBARU electron storage ring is not affected. Because the energy acceptance of the 1 GeV stored electron beam is 9 MeV, which is higher than gamma ray energies in the several-MeV regions, the storage electrons are not lost in the scattering process and do not decrease the beam lifetime. Thus, in principle, several-MeV gamma ray sources at NewSUBARU, combined with the CO_2 laser, do not have flux limitations. Because CO_2 lasers are considered the most successful lasers at high power generation, the gamma ray source is expected to be the highest-power light source in this energy region of the laser Compton gamma ray.

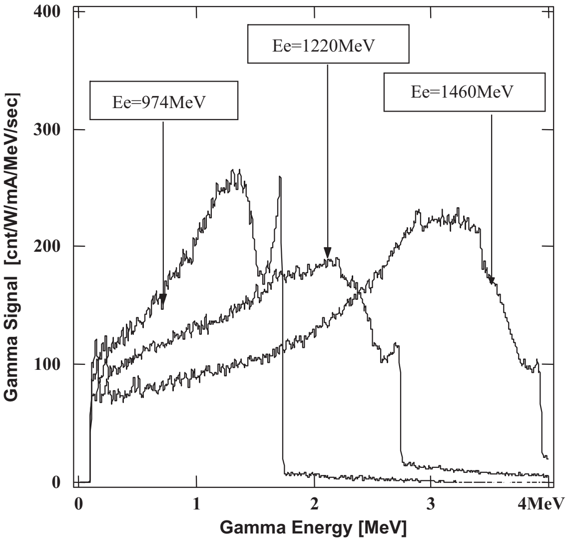

Fig.1 Gamma ray spectra measured by the Ge-detector at electron energies of 974, 1220 and 1460 MeV. The beam current was 1-2 mA and the laser power was 1 W.

Acknowledgments

This work was supported by Grants-in Aid of Scientific Research (C) no. 19540419 in 2008 from the Ministry of Education, Culture, Science and Technology (MEXT), Japan.

References

[1] S.Amano *et al.*, Nucl.Instr.and Meth. A 602 (2009) 337-341.

Measurements of Flux of Laser Compton Scattering Gamma Ray Photons Generated in BL01

Ken Horikawa
LASTI, University of Hyogo

Abstract

Absolute measurements of flux of laser Compton scattering gamma ray photons generated in an electron storage ring, NewSUBARU, with a Nd laser (1.064μm) beam was carried out by using a GSO detector. The maximum normalized flux of gamma ray photons was found to be $6.0\times10^3\pm5\%$photons/W/mA/sec at the beam hatch. The value obtained above was well reproduced by theoretical calculations.

Introduction

Until recently, radioisotopes have been used as a source of mono-energetic gamma ray, while the bremsstrahlung by high energy electrons has been used as a source of radiation that has a continuum energy spectrum. In 1963 Milburn, Arutynian, and Tumanian proposed a gamma ray source using laser Compton scattering. The idea came into reality in the last decade as a practical radiation source as the electron accelerator technology and laser technology were improved. [1], [2] The gamma ray source has not only a semi-monochromaticity, but also a remarkable advantage that it forms a highly directional and polarized beam. Therefore, a variety of applications are expected, especially for the gamma ray photons of MeV. The laser Compton scattering gamma ray sources are now regularly operated in TERAS, HIγS and NewSUBARU. [3], [4] In NewSUBARU, studies on nuclear transformation treatment of nuclear waste and gamma ray imaging were started. [5]

In this paper, we report the absolute measurement of the gamma ray photon flux in NewSUBARU. Laser beam intensity distribution is also discussed for maximizing the photon flux to be generated.

Absolute measurement of gamma ray photon flux

A gamma ray attenuation rate in the GSO detector was evaluated to exceed 99% at the photon energies of more than 6MeV by calculating the probability of energy dissipation due to photoelectric effect, Compton scatterings and pair creations [6]. Therefore it was concluded that the flux of gamma ray photons could be observed with the accuracy of within 1% without correcting the signal. A scattering angle of the gamma ray to be observed is limited theoretically within a solid angle which is determined by an absoreber (ABS) in the beam line in the case of NewSUBARU. The ABS is a shutter protecting a duct from radiations. An aperture size of the ABS is 30x20mm. The gamma ray beam size at the hatch was limited within 30mm which was smaller than 36mm of the size of the GSO detector. Therefore, we could make absolute measurements of the gamma ray photon at the hatch by using the GSO detector.

The normalized photon flux was measured to be $6.0\times10^3\pm5\%$photons/W/mA/sec.

Calculated photon fluxes of the laser Compton scattering gamma ray, and optimum laser focusing condition

Theoretical values of a total gamma ray photon flux and a net gamma ray photon flux are shown as a function of laser focus position in Fig. 1.

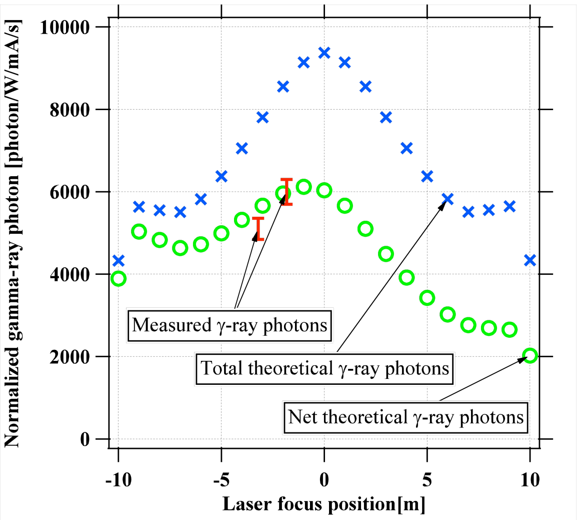

Fig. 1 Dependence of theoretical normalized photon number on laser focus position.

The total gamma ray photon flux is a theoretical value of the gamma ray photon flux which is generated in the whole of the interaction region. The net gamma ray photon flux is a theoretical value of gamma ray photon flux which can be taken out in the gamma ray hatch. The measured normalized gamma ray photon flux is also shown in Fig. 1 for different laser focus positions

In Fig. 1, the x symbol and the circular symbol indicate the theoretical maximum values of the total flux and the net flux available at the hatch, respectively. The bar symbols indicate measured values at the hatch. The theoretical value of the net flux has a hump which is located at the focus position of about -1 m. This accords well with that of the measured value. The net flux as a function of the laser focus position is considered to have a distribution whose peak is shifted to the negative side from the center in the interaction region because the acceptance solid angle for gamma ray increases at the negative side.

It is concluded that by taking into account the acceptance angle the measured net flux agrees well with the theoretical one and the optimum laser focus position for maximizing gamma ray generation can be well predicted by the theoretical calculation described above.

Conclusion

The absolute measurement photon flux of Nd laser Compton scattering gamma rays was carried out by using a GSO detector in which the gamma ray attenuation rate was over 99%. The maximum normalized photon flux of the gamma ray was found to be $6.0\times10^{3}\pm5\%$photon/W/mA/sec at the hatch. Theoretical calculations of laser Compton scattering gamma ray photon flux were done by taking into account various parameters, and the measured net flux agreed well with the theoretical one. It is concluded that the optimum laser focus position for maximizing gamma ray generation can be well predicted by the theoretical calculation obtained in this study.

Reference

[1] Richard H. Milburn, Phys.Rev.Lett.10, 75 (1963).

[2] F. R. Arutyunian, V. A. Tumanian, Phys.Lett.4, 176 (1963).

[3] H. Toyokawa, H. Ohgaki, T. Mikado, K. Yamada, Rev.Sci.Instrum.73, 3358 (2002)

[4] S. Miyamoto, Y. Asano, S. Amano, D. Li, K. Imasaki, H. Kinugasa, Y. Shoji, T. Takagi, T. Mochzuki, Radiation Measurements 41, 179 (2007)

[5] D. Li, K. Imasaki, S. Miyamoto, S. Amano, T. Mochizuki, J. Nucl. Sci. Technol., 42, 259 (2005)

[6] XCOM: Photon Cross Sections Database (http://physics.nist.gov/PhysRefData/Xcom/Text/XCOM.html)

Characteristics of EUV light and ion emissions from a micro lithium target

Akihisa Nagano and Takayasu Mochizuki
LASTI, University of Hyogo

Abstract

Characteristics of extreme ultraviolet light and ion emissions from a micro lithium target were investigated by using a double pulse irradiation. The EUV and ion emissions were enhanced by a factor of about 2~3 with a pre-pulse against that without the pre-pulse. Additionally, a number of fast ions were reduced at the pre-pulse. These results confirm that the double pulse method is useful to obtain a uniform plasma and optimize the plasma size.

1. Introduction

A high power 13.5 nm light source is under development for the application to extreme ultraviolet (EUV) lithography[1]. Major technical issues on the EUV source are improving an EUV conversion efficiency (CE) and suppressing the degradation of a condenser mirror by target debris, as well as developing a high-average-power pulsed laser. In a tin target, the CE is intrinsically high because major EUV emissions from the tin ions of Sn^{8+} to Sn^{13+}, concentrate around 13.5 nm[2]. However debris deposition or damage on the mirror, thus cleaning of the mirror would be the most critical issue to be solved in case of heavy metal targets such as tin targets. Alternatively, lithium (Li) metal debris will not deposit on the mirrors if they are maintained at ~ 400 ℃[3,4] and in addition a Li target has intrinsically a high spectral efficiency because of an intense line emission (1s-2p) in excited Li^{2+} ions at 13.5nm. In the case of using Li planar target, We demonstrated an improvement of CE by a forced recombination scheme and optimization of incidence laser wavelength[5,6].

Figure 1 shows an example of the practical forced recombination target. In this system, target materials are supplied continuously as liquefied Li such as filament jet or micro droplet. The recombination emissions near the wall can be also utilized. Therefore the target plasma should be uniformly heated because it needs to generate the plasma flowing toward the wall. In this paper, we report on characteristics of both EUV light and ion emissions from lithium micro targets by using a double pulse method[7].

2. Experiments and results

Figure 2 shows an experimental set-up. The experiments were carried out by using two commercial Nd:YAG lasers which were a Spectra-Physics Quanta-ray Pro-230 Series (SP) and a Quantel YG981C-10 (Quantel). The SP laser and the Quantel laser delivered a 1064nm wavelength laser pulse with pulse durations of 10~12 nsec and about 8 nsec, at full width at half maximum, respectively. Laser pulses were focused on micro Li target through a focal lens which had a focal length of 500mm in a vacuum chamber kept at about 4×10^{-3} Pa. Li-coated glass micro balloons (GMB) with a diameter of about 100μm were used as the micro targets. Li layer was formed on GMB surface with a thickness of 5~8μm by a vacuum deposition. EUV intensities were measured by calibrated EUV calorimeters. They were mounted at angular positions of -15˚, -90˚, 60˚, 125˚, and 160˚ to measure angular distributions of the emission. The emitted ions were measured by using charge collectors mounted at angular positions of 20˚, 70˚, and -160˚ at a distance of 140mm from the target. The EUV emission image at 13.5nm was monitored by an EUV camera which was consisted of imaging optics using two Mo/Si multilayered mirrors and a back-illuminated x-ray charge coupled device camera. An emission spectrum was monitored by a grazing incidence spectrometer mounted at angular position of 40˚ to the laser axis.

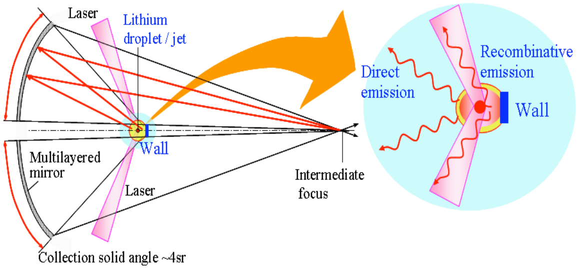

Fig. 1 An example of practical forced recombination target geometry.

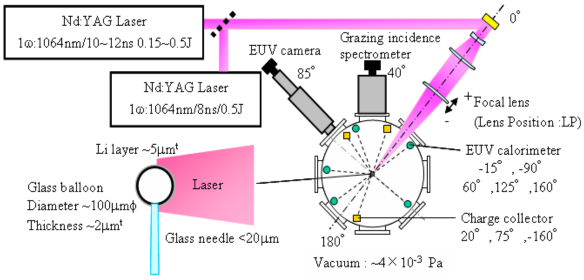

Fig.2 Experimental set-up.

Characteristics of EUV and ion emissions were investigated by using a double pulse irradiation. The incident energies of pre (SP) and main (Quantel) pulses were 0.15 and 0.5J, respectively. In this experiment, both laser pulses irradiated the target coaxially from the same direction with an about 400μm focal spot diameter.

The optimum pulse separation in time was found to be about 50 nsec. Angular distributions of EUV and ion emissions are shown in Fig. 3. With the pre-pulse, the EUV and ion emissions were enhanced by a factor of about 2 at the region from -60° to 60°and a factor of about 3 at the rear side of the target against laser illumination. We evaluated the kinetic energy spectra of the Li ions from the charge collector signals with and without the pre-pulse. The maximum kinetic energies are ~1.5keV and ~1.7keV with and without the pre-pulse, respectively. Furthermore a number of fast ions were reduced at the pre-pulse. At the energy of 1keV, they were found to be about one third of that without the pre-pulse. EUV emission images were obtained with and without the pre-pulse. The image size with the pre-pulse was about two times larger at the delay of 50 nsec than that without the pre-pulse.

These results confirm that the double pulse method is useful to obtain a uniform plasma and optimize the plasma size.

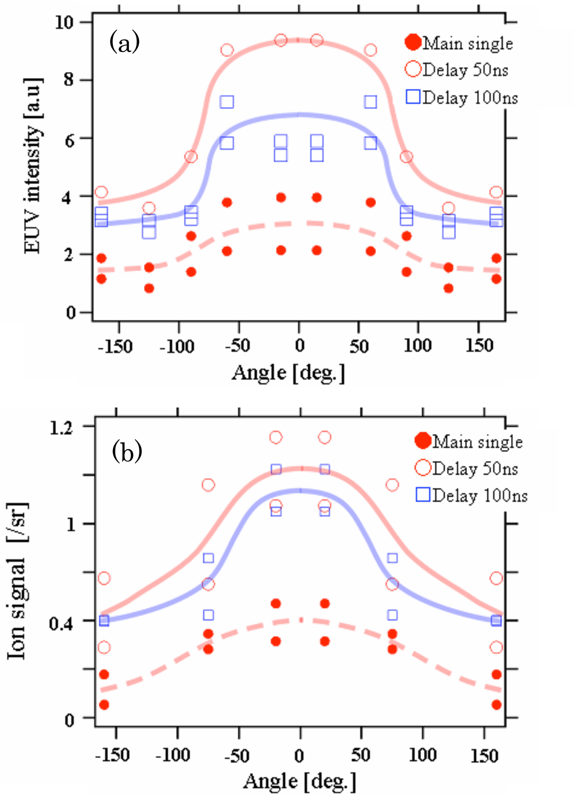

Fig. 3 Angular distributions of EUV(a) and ion(b) emissions.

References

[1] EUV sources for Lithography, edited by V. Bakshi SPIE, Washington, 1-1044, ISBN: 0-8194-5845-7 (2005)

[2] P. Hayden, A. Cummings, L. Gaynor, N. Murphy, G. O'Sullivan, P. Sheridan, E. Sokell, J. White, and P.Dunne, Proc. of SPIE 5751, 919 (2005)

[3] H. Takenaka, T. Kawamura, and T. Haga, OSA TOPS Extreme Ultraviolet Lithography 4, 169 (2005)

[4] D.W. Myers, I.V. Fomenkov, B.V.M. Hansson, B.C. Klene, and D.C Brandt, Proc. of SPIE 5751, 248 (2005)

[5] A. Nagano, T. Inoue, P. E. Nica, S. Amano, S. Miyamoto, and T. Mochizuki, Appl. Phys. Lett. **90**, 151502 (2007)

[6] A. Nagano,T. Mochizuki, S. Miyamoto, and S. Amano, Appl. Phys. Lett. **93**, 091502 (2008)

[7] R. Kodama, T. Mochizuki, K.A. Tanaka, and C. Yamanaka, Appl. Phys. Lett. **50**, 720 (1987)

Mitigation effect of plasma debris from cryogenic xenon target by argon buffer gas

T. Inoue, K. Masuda, S. Amano, T. Mochizuki
LASTI / UH

Abstract

In order to mitigate the sputtering effect on collection mirror which was caused by xenon fast debris, mitigation effect on plasma debris from the rotating drum xenon cryogenic target by an argon buffer gas and also absorption of soft X-ray from the plasma investigated. The sputtering caused by the fast xenon debris was reduced by 1/18 with an argon buffer gas of 8 Pa. The damping of the X-ray by introducing the argon buffer gas was measured to be about 0.75 % /Pa for a flight pass of 190 mm on these argon pressures. These results suggest that the plasma debris are well mitigated by an argon buffer gas without suffering from a serious loss of X-ray due to the optical absorption by the argon buffer gas.

Introduction

X-ray source generated from laser produced xenon plasma has a broad-band spectrum, and it would become a compact and high power soft X-ray source. In order to use this light source for a lot of applications, high average output power and reduction of condenses mirror damage by plasma debris are required. A high average output power was achieved by using a rotating drum xenon cryogenic target[1] and a 100W/320pps Nd:YAG slab laser system[2]. That was 20W into 2π for a wavelength range of 5 nm to 17 nm. Furthermore a focusing of soft X-ray was accomplished by using a cylindrical ruthenium mirror system under the condition of single laser pulse radiation. By setting up the system at a place that could collect the X-ray power, soft X-ray intensity at a focal point was improved by 46-times of that without the system[3]. However to use this mirror system at the operation condition of 100W/320pps, the mirror sputtering effect must be mitigated. Because, if we would operate the laser at 100W/320pps without debris mitigation, the mirror would be sputtered at a high rate of about 10nm/min[4]. To mitigate the sputtering effect, we introduce an argon buffer gas. Argon has a spectral peak at 3.2nm[5] which deviates from xenon peak of 10.8nm. Thus an absorption ratio of soft X-ray from xenon plasma by argon gas was about 1/10 of a self-absorption ratio of soft X-ray from xenon plasma by xenon gas on the same pressure.

In this paper, we report on a mitigation effect on plasma debris from the rotating drum xenon cryogenic target by an argon buffer gas and also report on the absorption of soft X-ray from the plasma by argon.

Experiments and Results

Fig.1 shows the experimental setup. A Q-switched 1.06μm Nd:YAG laser pulse was focused on a rotating drum xenon cryogenic target at incident normal. Laser pulses were irradiated with a energy of 0.3 J, a pulse duration of 8 ns, a focusing spot size of about 500μmΦ, and 10pps or single pulse operation. A drum was operated at a rotating speed of 130rpm and a vertical velocity of 3mm/s in 30mm width. A thickness of xenon layer was adjusted about 500μm and fresh surfaces were supplied in each shot. An argon buffer gas was supplied from a top of vacuum chamber. To evaluate a debris mitigation effect by the gas, we measured a sputtering rate in a gold film coated on a Quartz Crystal Micro-balance (QCM) which was mounted at 45 degree and a distance of 77 mm from a plasma source point. Soft X-ray energy was measured by an X-ray calorimeter at -22.5deg and a distance of 190mm from the source. The positions of these two instruments were determined, where a collection mirrors system should be set up. The xenon partial pressure was kept less than 0.2Pa during the experiment by a turbo-molecular pump mounted on the underside of a vacuum chamber.

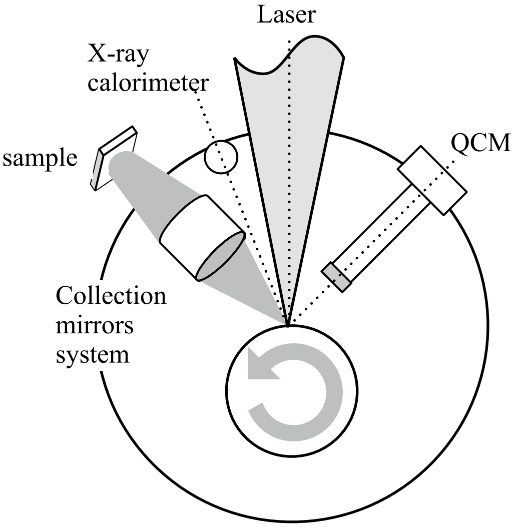

Fig.1 Experimental setup

Fig.2, 3 show the sputtering mitigation effect and the X-ray attenuation rate as a function of the argon partial pressure. The sputtering by the fast xenon debris was reduced by 1/18 with an argon buffer gas of 8 Pa. The attenuation of the X-ray by the argon buffer gas was measured to be about 0.75 % /Pa for a flight pass of 190 mm on these argon pressures. These results suggest that the plasma debris are well mitigated by a argon buffer gas without suffering from a serious loss of X-ray due to the optical absorption by ones.

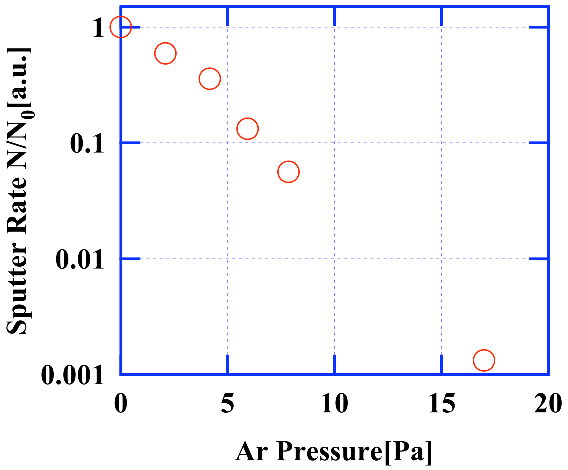

Fig.2 mitigation effect on gold film sputtering rate as a function of argon partial pressure. The vacuum pressure was corrected as argon gas.

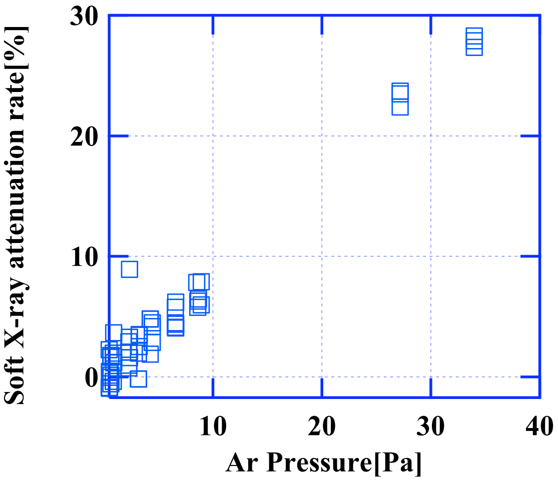

Fig.3 soft X-ray attenuation rate as a function of partial pressure.

References

[1] K.Fukugaki *et al* , Rev. Sci. Instrum. **77**, 063114 (2006)
[2] S.Amano *et al* , *Rev. of Laser Engineering*, Vol. **29**, pp.679-682 (2001)
[3] K.Masuda *et al* , *Lasti Annual Report*, vol.**9**, pp40-41 (2007)
[4] K.Masuda *et al* , *The Japan Society of Applied Physics and Related Societies, The 56th Spring Meeting*, 30p-ZR-9 (2009)
[5] T.Mochizuki et al , Proc. SPIE **3886**, 306 (2000)

PTFE Processing Characteristics of High-energy X-ray and Application to a bio-microdevice

Yoshiaki Ukira and Yuichi Utsumi

Abstract

This paper reports the smoothing effect of poly-tetrafluoroethylene(PTFE) by using high-energy X-ray. The roughness of surface was drastically decreased down to (Ra=5.6nm) form native surface roughness (Ra=93.5). The another attempt of the application to bio-microdevices is reported. The immunoassay for poly-chlorinatedbiphenil (PCB) is demonstrated by immobilizing 1st antibody on the surface of PTFE microstructure.

Introduction

Poly-tetrafluoroethylene (PTFE) is very attractive material for various fields including micro-electro mechanical systems (MEMS), RF-MEMS, and lab on a chip, because of its chemically stable, thermal and electrical good insulating, bio-convertible and low friction properties. However, it is difficult to fabricate PTFE microstructures with conventional techniques such as semiconductor process or micromachining. On the other hand we had succeeded in the fabrication of high-aspect-ratio microfluidic parts of PTFE by direct in-vacuum photo-etching using synchrotron radiation (SR) with high-energy of soft X-ray ranging in 2-12keV [1]. This paper reports a new finding of processing characteristics brought by using relatively high-energy X-ray irradiation on to the PTFE and application to the immunoassay system.

Smoothing of PTFE Induced by X-ray irradiation

It is known that SR induces the scission of polymer chain of polymers due to inner shell and valence electron photo excitation [2]. The decomposed photochemical products, which generated by high-energy x-ray irradiation, continually desorb from surface of the substrate, which results in the ablation of PTFE, while there induced recombination of radials in the bulk. It has been known that CFx ions are the dominant decomposed species of soft x-ray irradiated PTFE from mass spectrometry (MS) investigation [3]. We found the stoichiometry of PTFE is maintained even after the exposure as shown by the result of x-ray photoelectron spectroscopy. Next notable property is that the roughness of PTFE surface is greatly decreased by SR irradiation at the elevated temperature above 100 oC as shown in Fig. 1 and Fig.2. The origin of these phenomena are investigated in this work. We considered that the melting point of PTFE during SR irradiation becomes lower than normal (327oC) due to continual photo-fragmentation in the deep PTFE bulk induced by high-energy x-ray, and this leads the liquescence of the solid PTFE. The liquefied PTFE flows into porous textures of the bulk and only irradiated part of material is continuously etched specifically. It is speculated highly decomposed photoproducts such as CF, CF2 will be generated due to inner shell excitation, which leads to the sustain of stoichiometry and achievement of remarkable high aspect ratio of etching above 100, which confirmed for the first time by using the high energy x-rays of SR.

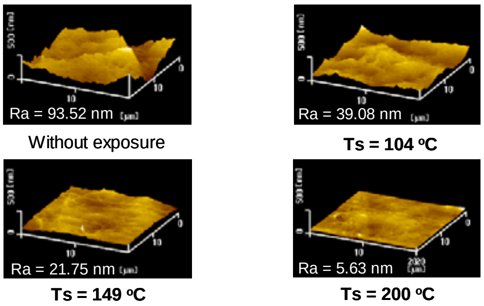

Figure 1 AFM images of x-ray irradiated PTFE surfaces. The dose condition were fixed at 200 mAhr

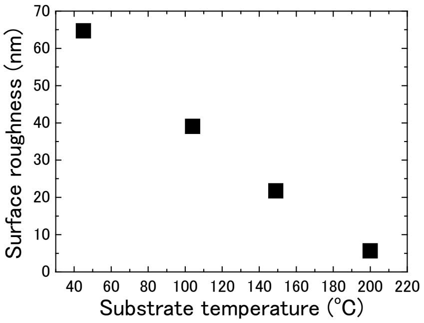

Figure 2 Dependence of surface roughness on substrate temperature

Application to a Bio-microdevice

In the case of conventional ELISA, polystyrene (PS) is standard material to immobilize the antibody, and it is also used for the lab on a chip as solid phase by using PS microbeads. However, it is expected that the use of PTFE microstructures bring great benefit for the application of lab on a chip to the system

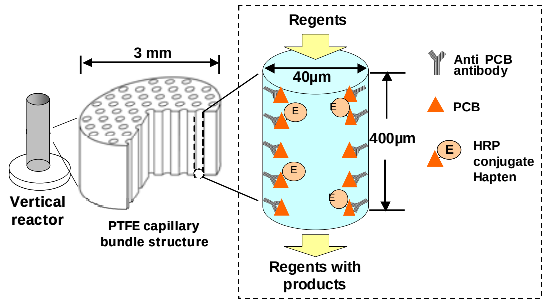

Figure 3 Schematic illustration of antibody-bound capillary bundle structure and vertical microreactor unit

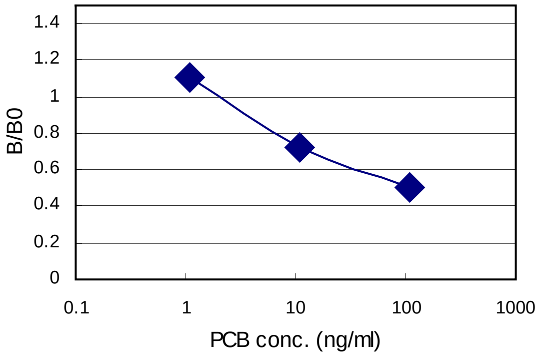

Figure 4 Calibration curve of PCB obtained by competitive ELISA

using organic solvent, such as immunoassay of poly-chlorinatedbiphenyl (PCB). On the other hand we proposed the high-sensitive immunoassay system using capillary bundle structure [4]. In this system the high-aspect ratio polymethylmethachryrate (PMMA) capillary bundle structure is fabricated by deep x-ray lithography and antibodies are immobilized on the PMMA capillary bundle structure. In this paper PTFE capillary bundle structure is used for better stability in organic solvent. As shown in the Fig. 3, anti-PCB antibody-bound PTFE capillary bundle structure is stacked into vertical microreactor and competitive ELISA is carried out in the vertical microreactor [4]. The large surface area of capillary bundle structure is effective to immobilize much antibody than normal microchips using microbeads or microchannels. For the competitive ELISA the standard sample of PCB is prepared by solving into organic solvent (dimethylsulfoxide: DMSO). The sample is mixed with hapten (enzyme-labeled PCB like matter) solution. Then mixture is injected into the antibody-bound capillary bundle structure and incubated for competitive antigen-antibody reaction. After the reaction, the substrate (tetramethylbenzidin: TMBZ) is injected into the capillary bundle structure and enzyme catalyze the degradation of TMBZ. After the incubation of enzyme reaction the reaction is aborted by 1N H_2SO_4 solution and amount of product is measured in the microchip. Figure 4 shows the obtained calibration curve, and decreasing signal with concentration of PCB suggests successful detection of PCB.

References

[1] Y. Ukita, K Kanda, S. Matsui, M. Kishihara, and Y. Utsumi, Jpn. J. Appl. Phys., Vol. 47, No. 1A , 337 – 341, (2007).

[2] M. C. K. Tinone, K, Tanaka, J. Murayama, N. Ueno, M. Imamura, and N. Matsubayashi, J. Chem. Phys. 100, 5988 (1994)

[3] J. K. Simons, S.P. Frigo, J.W .Tayler, R.A .Rosenberg, J. Vac. Sci. Tachnol. A 12 681-689,(1994)

[4] Y. Utsumi, T. Asano, Y. Ukita, K. Matsui, M. Takeo, and S. Negoro, J. Vac. Sci. Technol. B, 23, 2903-2908 (2006)

High density cell culture using micro 3D scaffold With capillary bundle structure

Tomoya Omukai*, Atsushi Kinoshita**, Fusao Komada** and Yuichi Utsumi*
*Laboratory of Advanced Science and Technology for Industry, University of Hyogo, Japan
**Faculty of Pharmaceutical Sciences, Himeji Dokkyo University, Japan

Abstract

We have proposed a method for high cell culture throughput by means of a micro 3D scaffold and density with high surface-to-volume ratio, and have successfully demonstrated that the throughput and density of cell culture significantly increased under a finite regime of scaffold size and figuration. We have succeeded in obtaining high density cell culture and also found that the size and figuration of capillaries in the micro 3D scaffolds significantly affect cell culture and surface adhesion.

Introduction

The conventional cell culture method for producing monoclonal antibody and therapeutic protein has remained the batch process, a process which is very time consuming due to its sorting and refinement complexity. Therefore cell culture throughput using a flat cell culture dish is limited. We have proposed a method for high cell culture throughput by means of a micro 3D scaffold and density with high surface-to-volume ratio, and have successfully demonstrated that the throughput and density of cell culture significantly increased under a finite regime of scaffold size and figuration. The scaffold can also be used as a bioreactor with combinatorial systems of cells and their useful products.

Evaluation qualitatively of 3D cell culture

We qualitatively evaluated the property of cell adhesion to a micro 3D scaffold of Poly Methyl Methacrylate (PMMA) fabricated by deep X-ray lithography as shown in Fig. 1 [1]. The scaffold consists of capillaries with different cross sectional sizes and figurations — honeycomb, diamond, pentagon, and circle. HepG2 cells transfected with pEGFP vector encoding Enhanced Green Fluorescent Protein (EGFP) were used to evaluate cell culture density by laser scanning microscope. As shown in Fig. 2 (a), (b), (c), and Fig.3, cultivated cells adhered to the inner-surface of the capillaries of the scaffold; however, cells did not adhered to the surface of the circle shape capillaries (Fig. 2 (d), 4). Thus, cross sectional figuration is shown to strongly influence cell adhesion. We also found the cross sectional size of the scaffold affects cell cultivation and adhesion. These findings suggest that competition between the supply of medium culture and excretion of metabolic products affects cell activities.

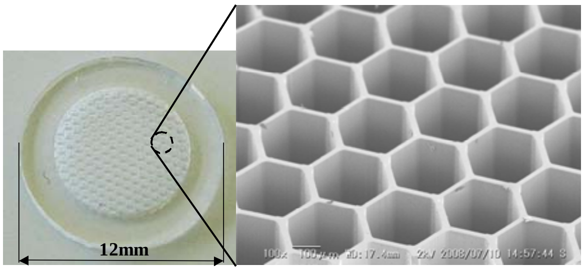

Fig.1 SEM image of PMMA 3D microstructure with cross sectional figuration of honeycomb capillary bundle.

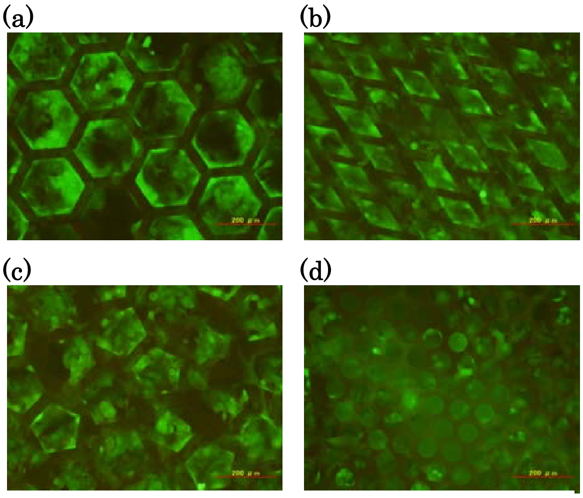

Fig. 2 Fluorescence images of 3D-cultivated cell adhered on scaffolds from various capillaries with cross sectional figuration of (a) honeycomb, (b) diamond, (c) pentagon, and (d) circle on day 3.

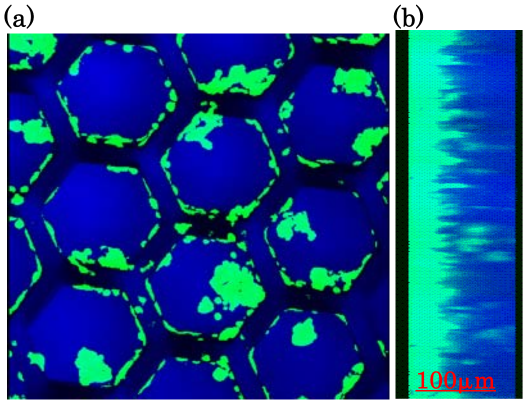

Fig.3 Fluorescence images of 3D-cultivated cell adhered to honeycomb capillaries by laser scanning microscope on day 4. (a) bottom view, (b) side view.

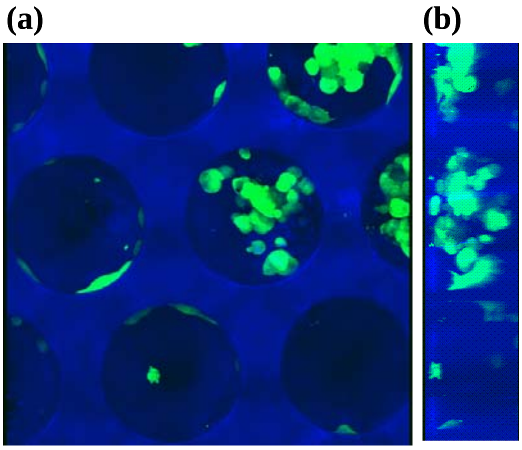

Fig.4 Fluorescence images of 3D-cultivated cell adhered to circle capillaries by laser scanning microscope on day 4. (a) bottom view, (b) side view.

Evaluation quantitatively of the 3D cell culture

Based on the above results, we evaluated the quantity of 3D cell culture in the capillaries of the micro 3D scaffolds with honeycomb and diamond cross sectional figurations over the course of several days. By determining the amount of GFP in cells, we measured the quantity of 3D cell culture which we then compared with flat plate PMMA results, as control. As shown Fig. 5, when using micro 3D scaffolds the cell number and the amount of GFP tend to increase, for the smaller size honeycomb capillaries; smaller the pattern, the greater the number of capillaries and the larger the surface area. All patterns showed a peak GFP amount at 10 or 12 days, suggesting the depletion of medium culture in the capillaries after the maximum cell multiplication. Moreover, we calculated the amount of GFP in each figuration per surface area of capillary and found that the amount of GFP per surface area of capillary increases for the smaller size cross sectional capillaries in the scaffolds.

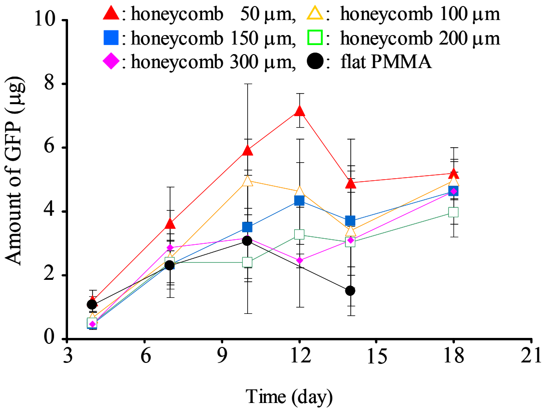

Fig.5 Time course for the quantity of cell culture with scaffolds from capillaries with honeycomb cross sectional figurations. (each point represent mean ± SD, n=3-8) The honeycomb capillary pattern has a side length of 50 to 300

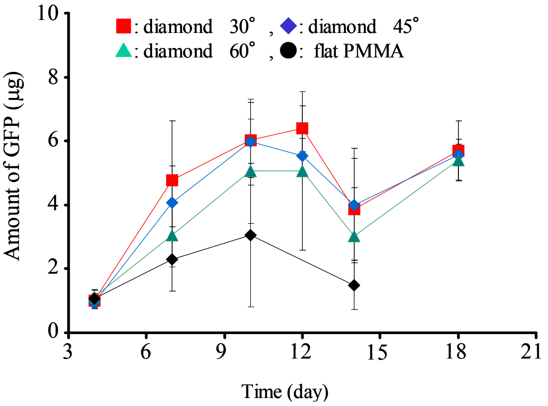

Fig.6 Time course for the quantity of cell culture with scaffolds from capillaries with diamond cross sectional figurations. (each point represent mean ± SD, n=3-8) The diamond capillary pattern has a inner angle of 30 to 60 degree.

Conclusion

We have succeeded in obtaining high density cell culture and also found that the size and figuration of capillaries in the micro 3D scaffolds significantly affect cell culture and surface adhesion. These results suggest that micro 3D scaffolds consisting of capillaries with optimized structure parameters are able to control cell culture figuration and increase culture density.

References

[1] Y. Ukita, T. Asano, and Y. Utsumi, Microsystem Technology, **13**, 435 (2007).

Fabrication of electrodes for multiplex nerval interface

M. kato[1], Eric. Blasius[2], Y. Ukita[1,3],K. Mabuchi[4], Y. Utsumi[1]
[1]Laboratory of Advanced Science and Technology for Industry, University of Hyogo
[2] University Karlsruhe
[3]Research Fellow (PD), Japan Society for the Promotion of Science
[4] The University of Tokyo

Abstract

The "flexible regeneration type nerve electrode" is an interface device for nerves, connecting nerve fibers to signal conducting lines on a micro structure, making it usable for "Microneurography". Our chips buildup is based on multiple PDMS (Polydimethylsiloxane)-layers.

1, Introduction

"Microneurography", developed by Karl-Erik Hagbarth and Ake B. Vallbo, is a technique for reading and manipulating nerve signals by tools, acting as "nerve signal interfaces" [1]. Today's applied "Microneurography" uses needle shaped tungsten structures as electrodes measuring nerve signals. This is achieved by penetrate a nerve fiber, intending to reach the core of the nerve with the tip of these structures. Commonly applied "Microneurography" has disadvantages such as difficult implantation, difficult positioning and unprecise readout of nerve signals due to macroscopic scale. Mentioned disadvantages render these methods unusable for practical medical services. The "flexible regeneration type nerve electrode" proposed by K Mabuchi from Tokyo University is an interface device for nerves, connecting nerve fibers to signal conducting lines on a micro structure, making it usable for "Microneurography" [2]. We rely on the regeneration ability of nerves by cutting one, putting our chip between the nerve ends and force it to grow together through our chip structure. Figure.1 shows the model of nerve reproduction electrode.

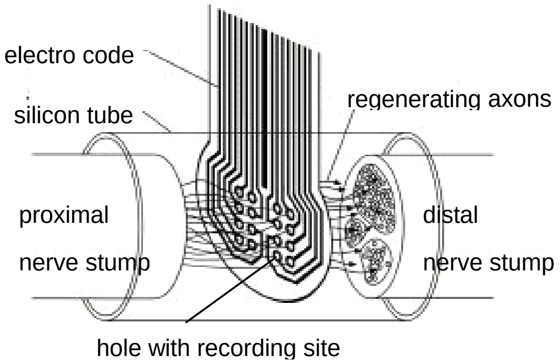

Figure.1 Model of nerve reproduction electrode

2. Design

Figure 2 shows the outline of the nerve regeneration electrode It is difficult to integrate many electrodes by using single layer due to small area. Thus the electrode shape is designed to be stacked allowing three-dimensional (3D) crossing of multiple electrode lines. For the first attempt, designed electrode structures have 12 channels electrode on a single layer and total 24 channels are realized by stacking two layers, however the electrode lines are not crossing due to coupling to our connector. Next, the capillary diameter is designed. 30 µm in diameter capillary structures were designed to allow the nerves to pass through due to minimum diameter (20 µm) of nerve fibers. Moreover, the capillary diameter of 60 µm and 90 µm were designed, which capable two or three nerves in a capillary.
The width of the electrode line was designed as 20µm by considering impedance and capillary density. Moreover, lines are spaced 20 µm to avoid the influence of noise such as leak current. It is also important for better detection of signals to realize good insulation between three-dimensionally stacked layers.

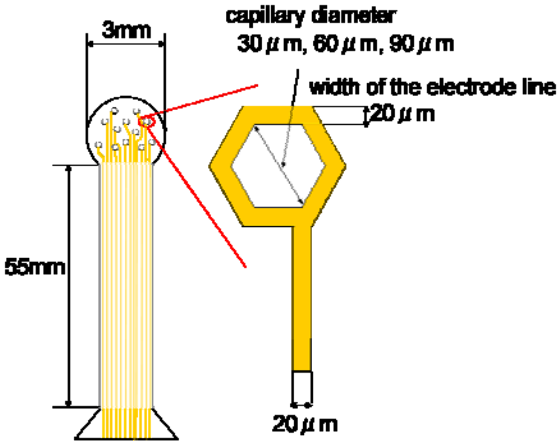

Figure, 2 Outline of electrode

3. Experiment

To form PDMS through hole structure pillar pattern is formed to transfer the opposite pattern on the PDMS film, by replication process. First of all, 40 nm thick Ti film is deposited on brass substrate by means of spatter for chemically stable surface and better adhesion of photoresist. Photoresist (AZP4903: AZ Erectronic Materials co. Ltd) is courted on the Ti layer and electrode line pattern is formed on the layer. Next 5 µm thick Au electrode line structure is filled in the line by means of electro plating. After removal of AZ resist, photoresist (KMPR1010 :KAYAKU Microchem Co. Ltd) is courted on the electrode pattern with thickness of 40 µm. Then pillar pattern (opposite capillary pattern) is formed on the electrode pattern by aligning the photomask on the electrode pattern. After photolithography PDMS resin is spincourted on the pillar pattern to cover 30 µm in thickness and cured. To form through hole structure, by removing PDMS thin film on the pillar pattern, PDMS is etched by reactive ion etching (RIE) with CHF3 and O2 gas source.

For accurate processing depth control of PDMS, we investigate the processing properties of PDMS by using RIE etching. [3] Especially processing rate of the PDMS layer strongly depends on the relaxation process time, which is interval time between curing of PDMS and etching process. As shown in figure 3 the etching rate is exponentially decreasing with relaxation.

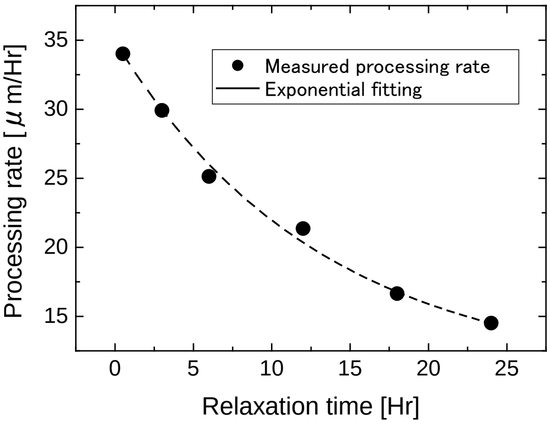

Figure.3 PDMS etching Graph Processing rate-Relaxation time

This is speculated that unstable chemical property of PDMS is contributing on the shift of etching properties. In the early stage of relaxation, there is a lot of monomer, which does not cross-linking by polymerization and the small monomer expected to be much volatile than polymerized structures.

Then KMPR pillar pattern is removed by removing process. In the removing process the substrate is dipped into Remover PG(KAYAKU Microchem Co. Ltd) then dipped again into Remover K(KAYAKU Microchem Co. Ltd). Finally brass substrate is etched in etchant (Cu-3931: Meltex .Inc) and freestand PDMS electrode chip is fabricated.

As shown in the figure 30 µm thick through hole structures are successfully formed on the PDMS thin film, and optical image o the electrode is shown in the figure 4.

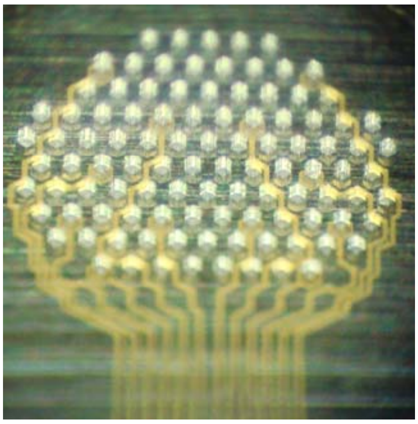

Figure.4 optical image on the electrode

4. Conclusion

The 3D stacked type regenerated nerve electrodes are proposed and trial fabrication is demonstrated. The through hale structure is formed on the PDMS thin film. The dry etching processing rate was strongly depends on the interval time between the PDMS curing and etching process. We are aiming to bond multiple electrode layers to complete the process for the application to the nerval interface.

Reference

[1] Åke B. Vallbo, Karl-Erik Hagbarth, and B. Gunnar Wallin, J. Appl. Physiol., "Microneurography: how the technique developed and its role in the investigation of the sympathetic nervous system" ,96,1262–1269 (2004)

[2] Takafumi Suzuki, Takashi Saito, Kunihiko Mabuchi, "Development of a multi-channel nerve electrode for peripheral nervous system" ,Technical report of IEICE, 100, 63-66 (2000)

[3] Nara, Y. Sugino, H. Arakawa, T. Shirasaki, Y. Funatsu, T. Shoji, S. , " High Through-Put Parallel Biomolecules Sorting Microsystem with Three Dimensional PDMS Stack" , 10.1109/SENSOR. 257-260 (2007).

Cross-linked capillary micromixer for high-sensitive immunoassay

Saki Kondo[1] , Yosiaki Ukita[1], Kuniyo Fujiwara[1], and YuichiUtsumi[1]
Laboratory of Advanced Science and Technology for Industry University of Hyogo[1],
3-1-2 Kouto, Kamigori, Ako-gun, Hyogo, 678-1205, JAPAN, Tel: +81-791-58-0232,

Abstract

A novel micromixer is proposed, fabricated and verified. The new concept of the micromixere is to cross-link the many capillaries in three-dimensional structure. The characteristic flow behaviors are simulated by using computational fluid dynamics (CFD) software"FLUENT". The results of the CFD shows unique mixing behavior in three-dimensionally cross-linked capillaries. The mixing performance of the micromixer is strongly influenced by controlling the three-dimensional crossing condition. The micromixer is fabricated by means of deep X-ray lithography with multi step exposure. The cross-linked capillary structures are successfully fabricated with controlled cross-link conditions. The performance of micromixer is evaluated by using a kind of enzyme reaction. By comparing mixture, mixed with cross-linked fluid filter and fluid filter without cross-linked capillaries, we found out the speeding up of the reaction by using new micromixer.

Introduction

The micromixing is one of the most important issues in the field of lab on a chip [1,2]. The quality of mixing will be very influential for the result of analysis; the use of non-uniform mixture will result in non-reproducible results and the use of uniform mixture will result in better results. This paper shows a unique micro mixing behavior in three-dimensional microstructure and its application to chemical reaction.

Simulation and Result

The new concept of this paper is to cross capillaries by controlling overlap level of crossing capillaries. The computational fluid dynamics (CFD) using CFD software 'FLUENT' is carried out to estimate the performance of the micromixer. To trace the mixing behavior, chemical species is assumed in initial condition. We assumed two crossing patterns which totally overlapping (fig. 1(b',d)) and half overlapping (fig. 1(c',e)) patterns and capillaries without crossing for control (not shown). Figure 1 shows initial condition of water (Fig. 1(a)) with chemical species (the property is the same as water) and mixed waters through cross-linked capillaries (Fig.1(b,c), the close ups of the cross-linked structure are shown in Fig.1(b',c')), and fig. 2 shows the time shift of the standard deviations (SD) of mass fraction of chemical species in the mixture. The results indicate that the crossing structure has much better mixing performance and half overlapped structure provides the best mixing, because it induces branch of flows around the cross (fig. 1(e)) while totally overlapped one does not exhibit such behavior because it maintains the stable laminar flow (fig. 1(d)).

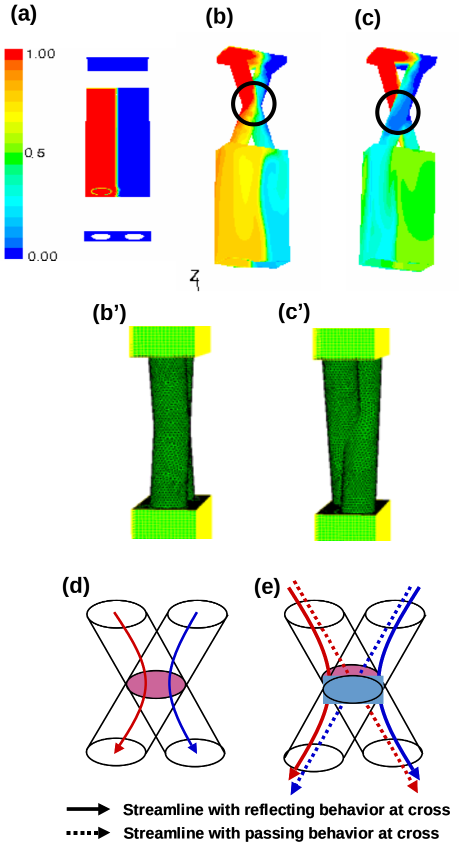

Fig.1 Simulated mixing behavior using CFD. Color bar indicates mass fraction of chemical species. (a) Chemical species is imaginary separated from water at initial condition. (b) Mixture obtained totally overlapped cross capillary structure and (c) mixture obtained half overlapped cross capillary structure. (b')(c') is showed enlarged view part of (b)(c) circle. (d) illustrates flow behavior in totally overlapped cross capillary structure ,(e) illustrates half overlapped cross capillary structure. Half overlapped structure induce branch of streamline due to un-overlapped part of cross.

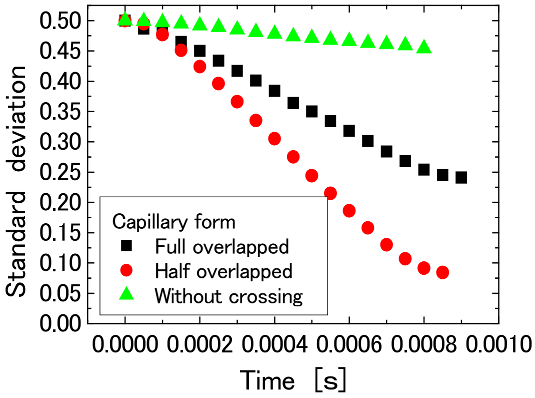

Fig.2 Time shift of standard deviation of mass fraction of red species.

Fabrication and Evaluation

Typical micromachining is not suitable to fabricate the cross-linked capillary structure, because it needs very complex processes control the level of overlap. To generate the cross-linked structure, deep X-ray lithography is applied. The PMMA resist attached with X-ray masks are tilted up to X-ray beam for first exposure and then tilted down for second exposed. The level of overlap is controlled by slightly rotating the masks around normal axis. Figure 3 shows the scanning electron microscope (SEM) image of fabricated micromixer with half over lapped structure. The complex 3D microstructure with twice crossing is successfully formed on thick PMMA resist by just exposing twice and developing.

To verify the mixing effects on chemical reaction, we applied this micromixer to enzyme reaction. Enzyme and substrate are mixed by passing the micromixer and the product of the enzyme reaction is measured by spectroscopy. Figure 4 indicates time consumption for saturation of reaction yield. The speed of the reaction is drastically speeded up and the error bar is drastically decreased by using cross-linked structure, and it means that cross-linked structure reproducibly provides uniform mixture.

Conclusion

These results indicate that the micromixter with cross-linked capillary structure has much higher mixing performance. It is considered that the characteristics of this micromixer is effective not only speed up of the reaction but also reproducibility and sensitivity of the assay by using reproducible mixing. And this micromixier is considered that very useful for pre mixing module for biological reaction such as enzyme linked immunosorbent assay (ELISA). Further more, the antibodies for immunoassay can be immobilized onto the surface of cross-linked capillary structure. By using the large surface area of cross-linked capillary structures the enzyme reaction of the ELISA will effectively amplified and it can result in higher sensitivity [3, 4].

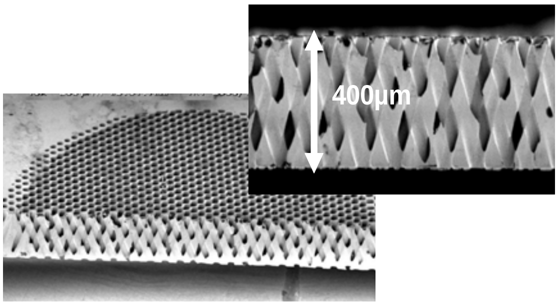

Fig.3 SEM images of cross-linked capillary bundle structure (half overlapped type)

Fig.4 The time of saturation. The error bars indicate standard deviation. Groups are 4 and 5 for with cross and without cross, respectively.

References

[1] Chien-chong Hong *et al.*, Lab Chip,**4**, pp.109(2004)
[2] Robin H. Liu et al., jmemsv, **9**, pp.190(2000)
[3] Y. Utsumi et al., J. Vac. Technol. B, **24**, pp.2606(2006)
[4] Y. Ukita et al., Sens. Actuators A, **145**, pp.499(2008)

Resolution enhancement of EUV microscope using an EUV beam splitter

Masafumi Osugi[1,3] Kazuumi Tanaka[1,3] Noriyuki Sakaya[2,3] Kazuhiro Hamamoto[2,3]
Takeo Watanabe[1,3] and Hiroo Kinoshita[1,3]
[1] LASTI/UH, [2] HOYA Corporation R&D Center, [3] CREST-JST
E-mail: kinosita@lasti.u-hyogo.ac.jp

Extreme ultraviolet lithography (EUVL) has been proposed as a next generation lithography at the 32 nm node around 2009. In the technology, defect-free mask is one of the critical issues. Consequently, we developed EUV phase-shift microscope (Figure 1) to detect such as phase-defect in multilayer mask[1)]. And we have developed the EUV beam splitter, which is critical component of phase-shift inspection or resolution enhancement. The optical system portion of an EUV microscope is shown in Figure 2. In this optics, as NA becomes different number between longitudinal and tangential direction, resolution decreases in one direction. However, by installing EUV beam splitter above Schwarzschild optics, NA becomes uniform for all planar direction and resolution improves (Figure 3).

Figure 4 shows fabrication process of EUV beam splitter[2)]. In this process, stress control is important at depositing multilayer. We controlled by changing of RF power, DC power, and the Ar working pressure. We could fabricate multilayer of low tensile stress by counteracting tensile stress of molybdenum film and compressive stress of silicon film.

Figure 5 shows the exposure results of elbow pattern of 300 nm in size. Before installing beam splitter, lines of vertical direction could not be resolved(a). However, after installing beam splitter, the 300-nm L&S elbow pattern for all planar direction(b) has been clearly resolved. Figure 6 shows the close up of these patterns in horizontal(a) and vertical(b) directions.

We have developed an EUV microscope with a beam splitter for the first time and succeeded in the highly precise pattern inspection.

References
1. K. Hamamoto, Y. Tanaka, S.Y.Lee, N.Hosokawa, N.Sakaya, M.Hosoya, T,Shoki, T. Watanabe and H. Kinoshita,J. Vac. Sci. Technol, B23(6), Nov/Dec (2005) 2852
2. Y. Mizuta, M. Osugi, J. Kishimoto, N. Sakaya, K. Hamamoto, T. Watanabe, H. Kinoshita SPIE 6517 (2007) 113

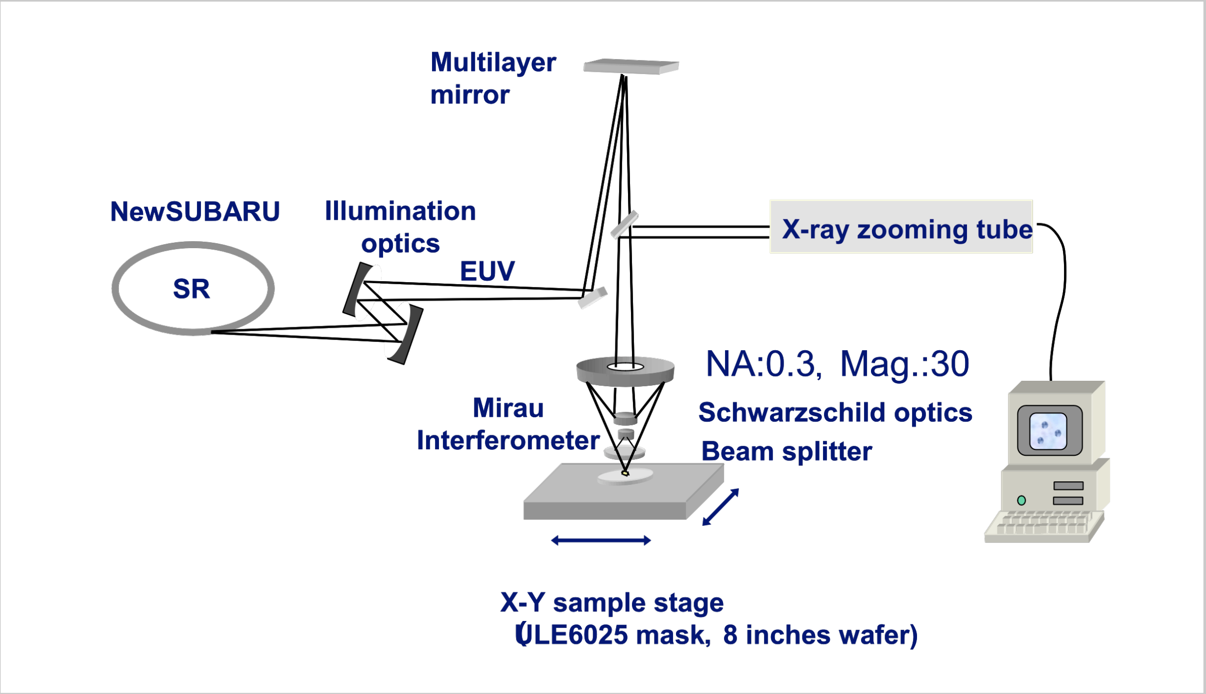

Fig. 1. Configuration of EUV phase-shift microscope.

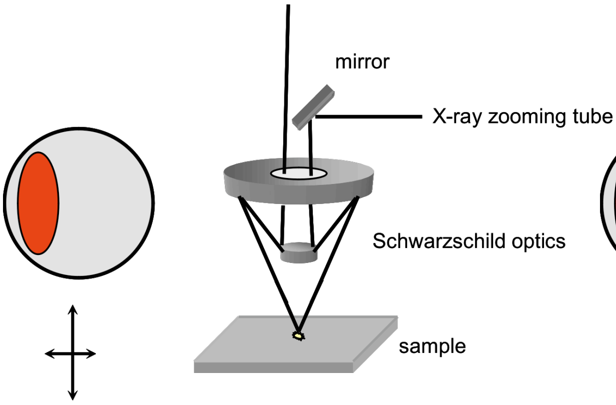

Figure 2. Configuration of Schwarzschild optics

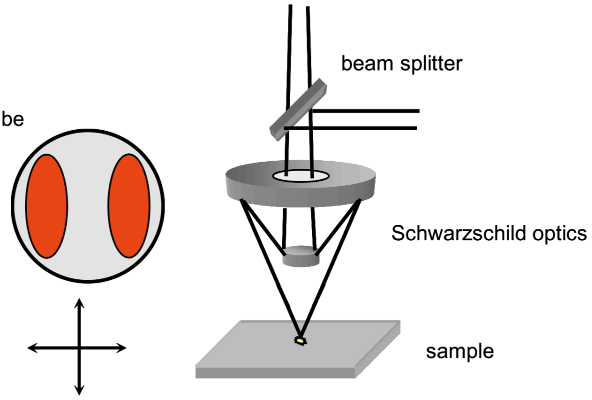

Figure 3. Configuration of Schwarzschild optics installed EUV beam splitter

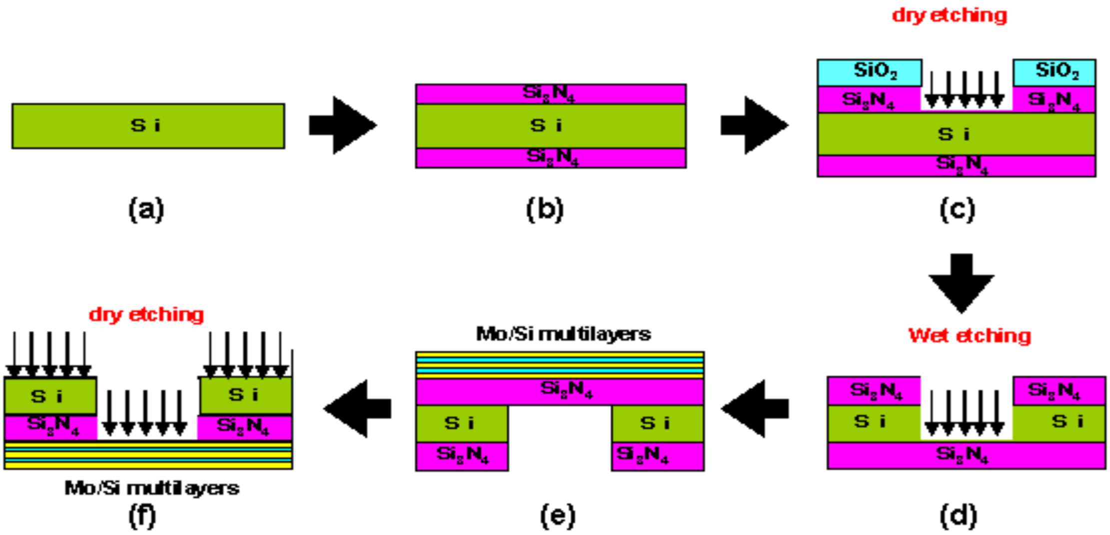

Figure 4. Fabrication process of EUV beam splitter splitter

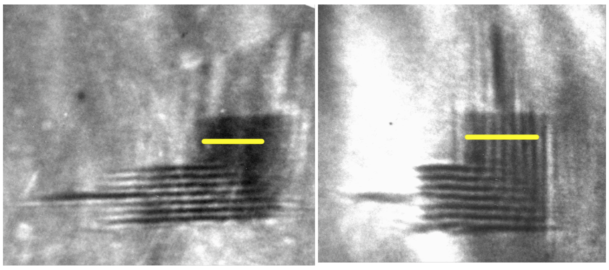

(a)Turning mirror

(b)Installed beam splitter

Figure 5 300-nm elbow pattern before(a) and after(b) installing EUV beam splitter

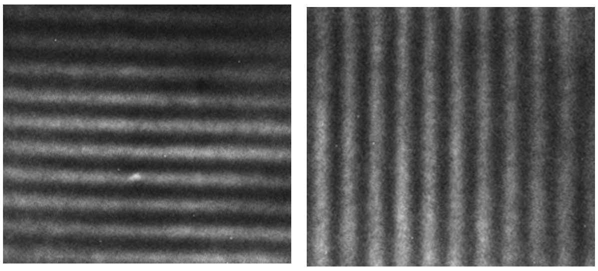

(a)Horizontal lines

(b)Vertical lines

Figure 6 Close up of Figure 5(b)

Dual grating interferometric lithography for 22-nm node

Hideaki Shiotani [1], Shota Suzuki [1], Dong Gun Lee [2], Patrick Naulleau [3],
Takeo Watanabe [1], Yasuyuki Fukushima [1], Ryuji Ohnishi [1], and Hiroo Kinoshita [1]
[1] LASTI/UH, [2] Photomask Team, Memory Development Business Division, Semiconductor Business,
Samsung Electronics Co., LTD, [3] Laurence Berkeley National Laboratory
E-mail:takeo@lasti.u-hyogo.ac.jp

An EUV resist with high sensitivity and low line edge roughness (LER) is required. LER of a resist is strongly affected by an aberration and a flare of an imaging optics. The flare of less than 10% is required for LER evaluation in an exposure tool. Thus, since an EUV interference lithography has no aberration and no flare, LER evaluation is necessity to utilize EUV interference lithographic exposure tool.[1,2]

We propose a dual grating interferometric (DGI) lithography which can be operate in the usage of an incoherent EUV light source. Thus, the DGI exposure method can combine with a stand alone EUV source, such as laser produced plasma and discharge produced plasma. Therefore, this exposure system becomes a compact one for the evaluation of resolution and LER in a EUV resist. Figure 1 shows the configuration of a DGI exposure setup which can use incoherent EUV light source. In this interferometric optical system, two transparent-type diffraction gratings are employed. An cherent light is produced by 1st-grating from an incoherent light source. Then, an interference fringe patterns on a wafer are made by 2nd-grating. A replicated pitch width of a resist pattern is a half-pitch width of 2nd transparent-type diffraction grating pattern. The calculated intensity distributions on a wafer obtained by a computer simulation (a) for an incident coherent light and (b) for an incident incoherent light are shown in Fig. 2. It indicates that DGI exposure method works well even if the usage of incoherent light instead of coherent light.

This diffraction grating using for DGI system was fabricated through by an electron beam writing and dry etching process. In our setup, bending magnet of SR storage ring is employed as a light source, and light from a bending magnet is monochromated to the EUV wavelength region. The photograph of the exposure tool using DGI system is shown in Fig. 3. The exposure tool consists of a main chamber which includes wafer stage and diffraction gratings. And load lock chamber is attached to the exposure chamber to exchange a wafer. It is believed that the developed EUV interference lithographic system is a beneficial tool to develop EUV resist which satisfies the specification of 32 nm and below.

References

[1] H. H. Solak ; J. Phys. D: Appl. Phys. 39, 171 (2006).
[2] A. M. Goethals, R. Jonckheere, G. F. Lorusso, J. Hermans, F. Van Roey, A. Myers, A. Niroomand, I. Kim, F. Iwamoto, N. Stepanenko, and K. Ronse, J. Photopolym. Sci. Technol. 20, 383 (2007).

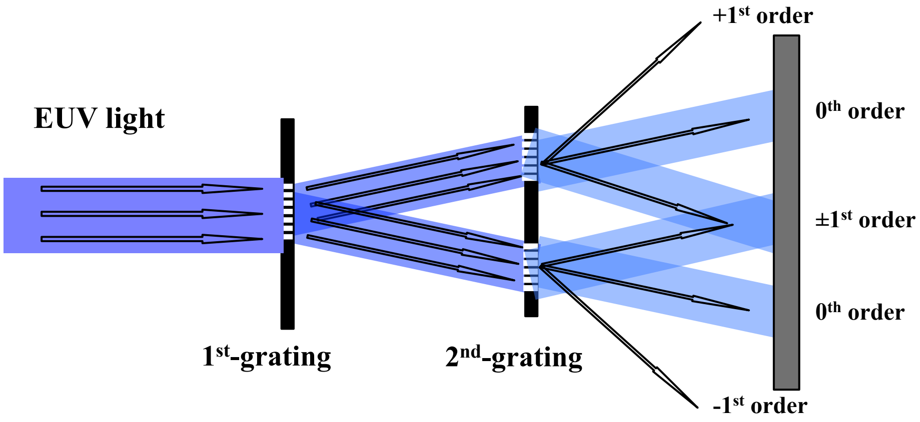

Fig.1. Dual grating interferometric system.

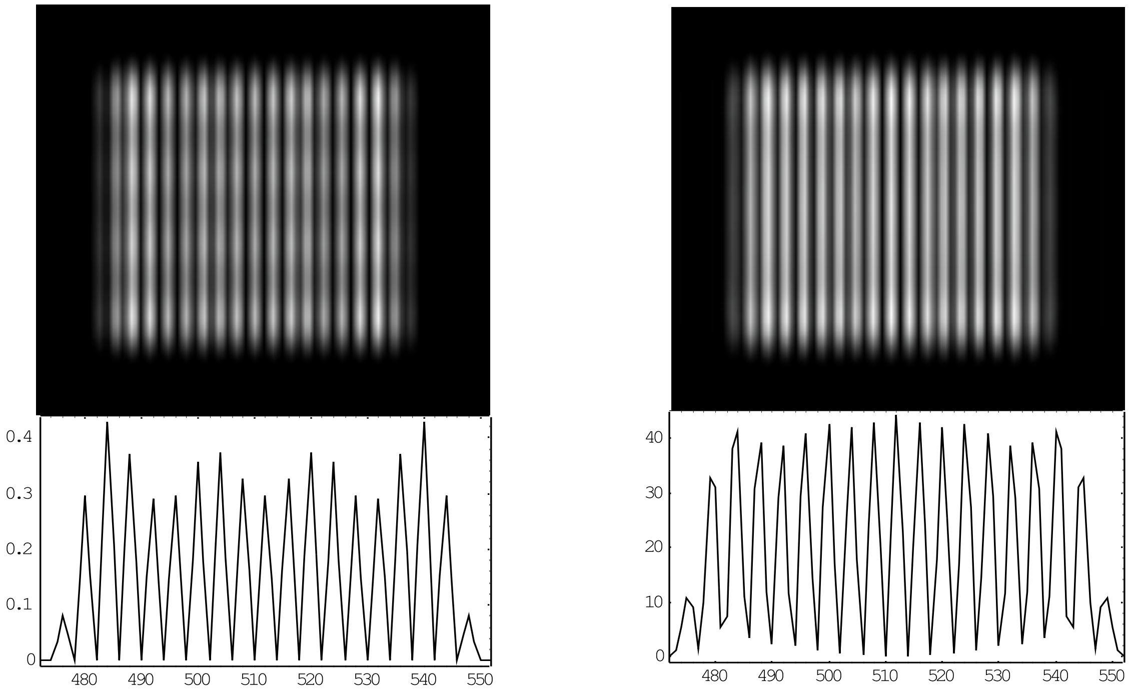

(a) **Coherent Monochromatic Beam**

(b) **Incoherent Δλ= 8nm (11 nm~ 19 nm)**

Fig. 2. The calculated intensity distributions on a wafer
(a) for an incident coherent light, and (b) for an incident incoherent light.

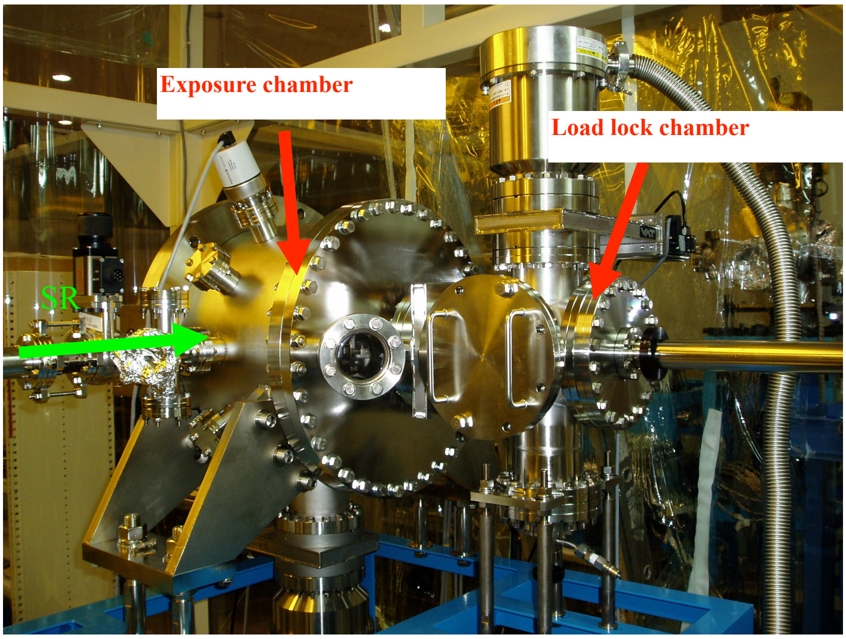

Fig. 3. The DGI exposure tool

Pattern Replication in EUV Interference Lithography

Shota Suzuki, Yasuyuki Fukushima, Ryuji Ohnishi,
Takeo Watanabe, and Hiroo Kinoshita

LASTI/UH

EUV interference lithography (EUVIL) beamline which employed a single grating was constructed at the BL3 beamline in NewSUBARU synchrotron radiation facility. Using this system, 400-nm L&S resist pattern by single grating interferometric lithography system which employed a bending magnet as a light source was replicated on a wafer.

In the otherwise design of EUVIL gratings, a dual grating interferometric system which is useful for a bending magnet as a light source was designed and constructed at BL3 beamline. Dual grating interferometric lithography has a capability for the replication of 28 nm line and space pattern on a basis of the interference-fringes calculation in the condition of partial coherence light source such as a bending magnet. In dual grating interference optical system, two transparent-type gratings were employed.

Keyword: EUV resist, chemically amplified resist, interference lithography

1. Introduction

Extreme ultraviolet (EUV) lithography[1] is the most promising technology for 32 nm node, and it is required for the high volume manufacturing lithographic technology around 2011. Resist materials and process technologies are one of the three top issues.[2] High sensitive and low line edge roughness (LER) have to be achieved simultaneously. In a stand view of resist material development, the exposure characteristics of resist material itself should be studied to design and synthesis of EUV resist which can satisfy the EUV resist specification. From this point of view, since LER is affected by aberration and flare of the imaging optics, aberration and flare of the exposure tool for the EUV resist evaluation have to avoid. The flare of less than 10% is required for LER evaluation for an exposure tool for 32 nm node beyond[3]. On the other hand, in the interference lithography (IL), since IL does not require complicated and expensive high numerical aperture imaging optics, IL has no aberration and no flare for the imaging optics.

EUV light from an undulator as a light source at synchrotron radiation facilities has long been recognized as a possible source for interference lithography in this regime[4]. A periodic pattern can be replicated on a wafer by IL using a coherent light source such as an undulator. [5, 8] Lloyd's mirror interferometer systems [5, 6] and single grating interference (SGI) system[7, 8] are proposed. The Lloyd's mirror interferometer (LMI) system is based on a single mirror. Replicated resist resolution of LMI is limited by temporal coherence ($l_c \approx \lambda^2 / \Delta\lambda$, where λ is an exposure wavelength).[9] On the other hand, replicated resolution of SGI is limited strongly by spatial coherence and SGI had been usually used with a coherent light source such as laser and an undulator. In synchrotron radiation, a bending magnet is more compact, more simple and cheaper than an undulator. Thus, in this paper, we would like to discuss an EUV interference lithography using a single grating interference (SGI) system and a dual grating interference (DGI) system for the usage of a bending magnet as a source.

2. Single Grating System

Figure 1 shows a configuration of a final structure a fabricated transparent grating with two windows. Figure 2(a) shows seven transparent gratings with two windows which was fabricated on a 4-inches wafer. And Figure 2(b) shows a photograph of 800-nm-L&S Si_3N_4 grating pattern observed by an optical microscope.

In the fabrication process of a transparent two window grating, 1) a 4-inches silicon wafer which had been coated with Si_3N_4 layers on the both sides of a wafer in 300-nm thickness was prepared. 2) tantalum layer was sputtered on a Si_3N_4 layer. 3) ZEP520 resist was coated with 650-nm thickness. 4) Resist pattern was replicated by electron beam lithography. 5) The resist pattern was transferred to the tantalum and Si_3N_4 layer by a dry-etching using CF3 gas. 6) Resist was removed by dry etching process using O2 gas. 7) Backside of Si_3N_4 of a demanded aperture was removed by a CF3-dry-etching process using glass mask. 8) Aperture area on silicon substrate was removed by a wet etching process using KOHaq. During this process, Si_3N_4 layer acts as an etching mask. Then the transparent

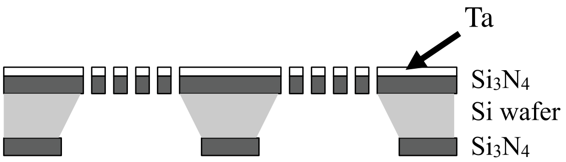

Fig.1 Configuration of a final structure a fabricated transparent grating with two windows.

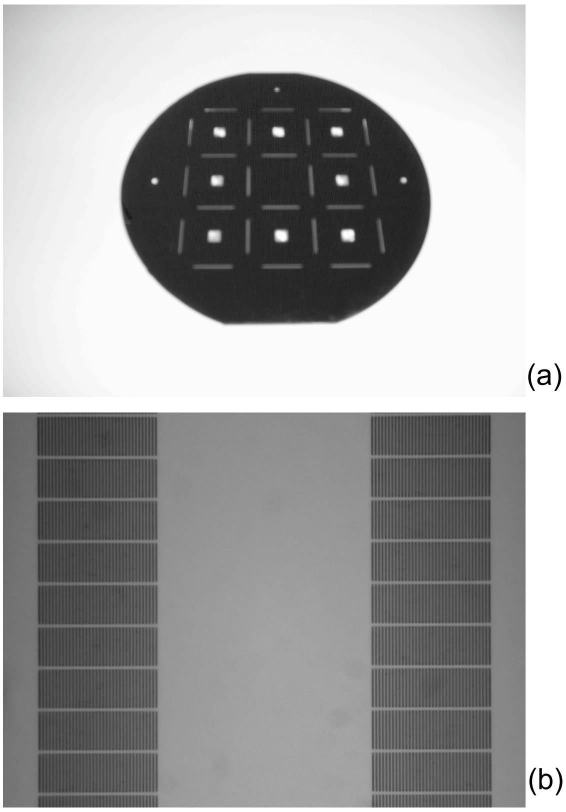

Fig.2 (a) Photograph of transparency grating and (b) photograph of 800-nm-L&S Si_3N_4 grating pattern.

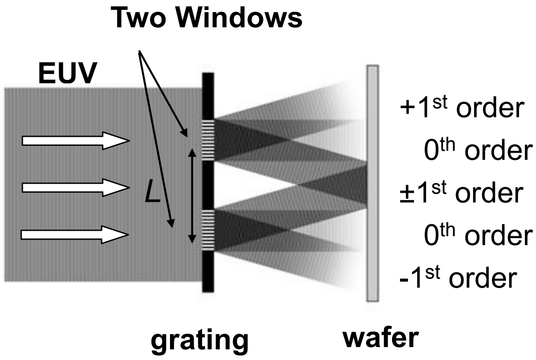

Fig.3 Principle of SGI system.

grating which can be used in interference lithography was fabricated.

Fig.3 shows the principle of SGI system. 0th order, 1st order, and -1st order are produced by a transparent grating. As shown in Fig. 3, if two grating is used, 1st order ray produce from one window grating interfere in -1st order ray produced from another window of a grating, and an interference fringes is created at the suitable position. Then if the resist inserted at the suitable position, periodic pattern of a resist will replicated on a basis of an interference fringes. In principles, capable-replicated-pattern size is limited to a half size of the wavelength.

SR light which is produced from the bending magnet of the electron beam storage ring is led to the glancing mirrors M1 and M2. After these mirrors, the beam size and divergence become to be 20 mm in diameter and divergence of ±0.75 mrad respectively. Then the SR light is led through the 4 jaw slits, shutter, a 0.15-μm-thick Zr filter and a reflected by Mo/Si multilayer mirror M4 to monochrome to the EUV wavelength. The centroid wavelength of the reflectivity spectrum is 13.5 nm and full width at half maximum (FWHM) is 0.7 nm. Finally, EUV light led to SGI system. Single grating exposure chamber maintains typically the vacuum pressure in the order of 10^{-6} Pa using a turbo molecular pump and scroll dry pump. Loadlock system for exchanging wafer sample was attached to the exposure chamber to change a 4-inches wafer. The spatial coherent length, L_c, is related to its angle distribution, σ, by the relation of $L_c = \lambda / \sigma$.[9] Since the light angle distribution on a single grating is 0.35 mrad, calculated coherent length is 38.6 μm. The distance L between the two-window grating has to be smaller than the spatial coherent length.

To replicate resist pattern caused by an interference fringes formulated from a single grating, distance between a single grating and a wafer and tilt position of a grating tilt have to be aligned. In order to control the gap between grating and wafer along light axis, we used Z-motion stage which can be moved by a pulse motor in vacuum pressure order of 10^{-6} Pa, and the stage moving resolution is 1.5 μm. Furthermore, we installed the α and β axis stages which can control the grating tilt position around by horizontal and vertical directions.

Figure 4 shows a photograph of a replicated ZEP520A resist pattern of 400-nm line and space (L/

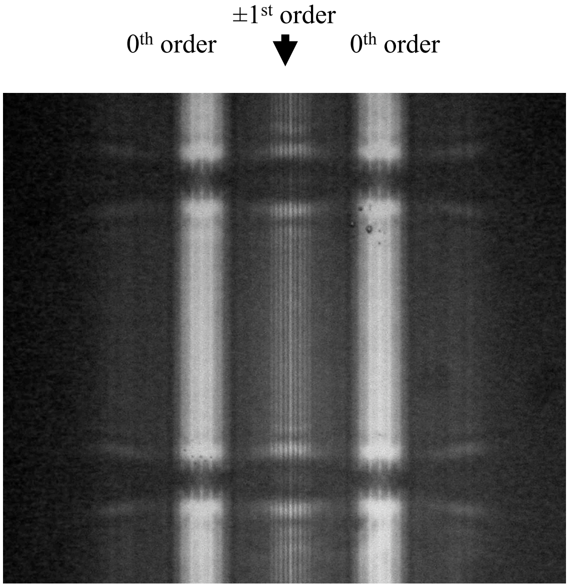

Fig.4 Replicated ZEP520A resist pattern of 400-nm line and space (L/S) pattern observed by optical microscope.

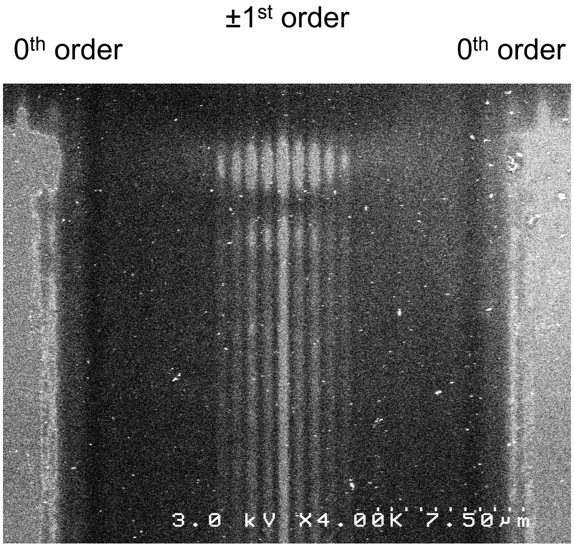

Fig.5 Replicated ZEP520A resist pattern of 400-nm line and space (L/S) pattern observed by optical microscope.

S) pattern using a 1600-nm-pitch single grating which was observed by a scanning electron microscope (SEM). Exposure time was around 10 s with a 0.2-um-thick Zr filter. As a result, using a bending magnet as a light source, we obtained interference replicated pattern. However, the pattern contrast is not perfect because of low temporal coherence of the bending magnet.

3. Dual Grating System

As a result of calculated interference fringes of the intensity distribution on a wafer in comparison with a coherent light and a partial coherent light, using 200-nm L&S grating, 100-nm L&S pattern on a wafer can be replicated easily from coherent light. However, it is difficult to replicate 100-nm L&S pattern using single grating system with partial coherent light. In this calculation, it is assumed that beam size of 20 mm in diameter and the divergence of ±0.75 mrad for a partial coherent light in the condition of a BL3 beamline after M1 and M2 mirrors.

To improve the resolution, it is introduced dual grating system which can allow pattern replication of 28-nm width. The setup of dual grating system is shown in Fig 5. 1st grating has one grating window, and 2nd grating has two grating windows to transmit the incident EUV light. By 1st grating, an incident light is diffracted into -1st and +1st order rays. Then by two grating windows of 2nd grating, -1st and +1st order rays produced from 1st grating are diffracted into -1st order ray and +1st order ray. Finally each -1st order ray and +1st diffracted from two grating windows of 2nd grating interfere each other to produce interference fringes on a suitable position of a wafer. In dual grating system, using 1st grating the incident light of 2nd grating is reproduced to satisfy special coherency.

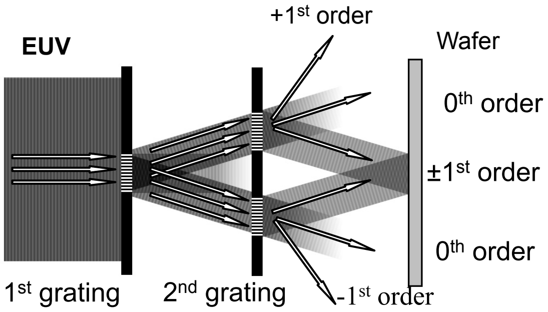

Fig.6 Setup of dual grating system.

If the incident light is a parallel ray, pattern size replicated on a wafer can be calculated by the following equation, where d_1 and d_2 are the pitches of 1st grating and 2nd grating, respectively.

$$P = \frac{1}{2\left(\left(\frac{1}{d_2}\right) - \left(\frac{1}{d_1}\right)\right)}$$

1) For example, if 400 nm pitch of 1st grating and 100 nm pitch of 2nd grating are used, it can be replicated 33-nm L&S pattern on a wafer. 2) For example, if 800 nm pitch of 1st grating and 100 nm pitch of 2nd grating are used, it can be replicated 28 nm L&S pattern on a wafer. 3) For example, if 1000 nm pitch of 1st grating and 80 nm pitch of 2nd grating are used, it can be replicated 22 nm L&S pattern on a wafer.

Figure 7 shows the calculated interference fringes and intensity distribution on a wafer. In this calculation, 800-nm pitch grating is used as a 1st grating, and 100-nm pitch grating was used as 2nd grating. The distance between 1st and 2nd grating is 109 mm, and distance between 2nd grating and a wafer is 43 mm. Furthermore, the partial coherence condition was used is same to that used in single grating. The results show that good performance in both of using coherent light source and partial coherent light source. Therefore, 28-nm L&S pattern can be replicated on a wafer using BL3 beamline.

SR light which is produced from the bending magnet of the electron beam storage ring is led to the glancing mirrors M1 and M2. Then the SR light is led through the 4 jaw slits and shutter. Finally the EUV light leads to the dual grating system. Dual grating exposure chamber maintain typically the vacuum pressure in the order of 10^{-6} Pa using a turbo molecular pump and scroll dry pump. Loadlock system was attached to the exposure chamber for exchanging a 4-inches wafer sample. In order to control the gap between dual grating and wafer along light axis, we used Z-motion stage which can be moved by a pulse motor in a high vacuum pressure, and the stage moving resolution is 1.5 μm.

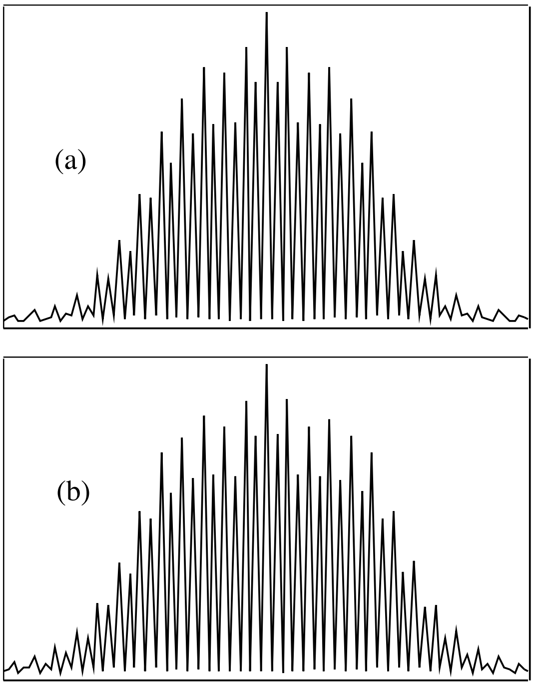

Fig.7 Calculated interference fringes and intensity distribution on a wafer in the DGI system, (a) coherent light and (b) partial coherent light.

Furthermore, we installed the α and β axis stages which can control the dual grating tilt position around by horizontal and vertical directions. The dual grating

Figure 7 shows 3-demensional-setup view of dual grating system. Two slits and one spacer are used to align the dual grating system. Short distance between 1st and 2nd grating is achieved to increase the tolerance of the alignment. The thickness of two slits and a spacer are 200 μm and 4 mm, respectively. The thickness of the silicon substrate of 1st and 2nd grating are 500 μm, respectively. Surface of 1st grating sits right direction and surface of 2nd grating sits left side on a paper sheet to maintain the distance of 4 mm between the surfaces of 1st and 2nd grating. Furthermore, distance between the surface of 2nd grating and a wafer is maintained to be 1.8 mm.

Figure 9 shows a ZEP520A resist pattern on 4-inches wafer. Center exposure area is an interference region of +1 order and -1 order from two grating window area from 2nd grating in dual grating system.

The effectiveness of using dual grating system combined with a bending magnet as a source is confirmed.

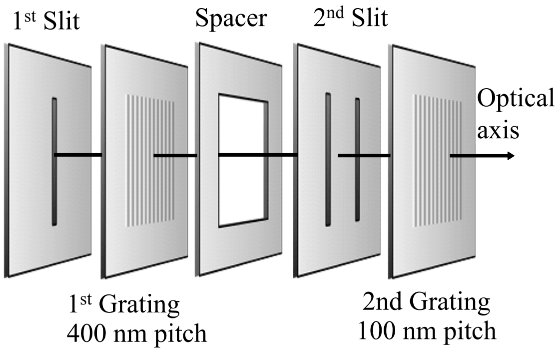

Fig.8 Three-demensional-setup view of dual grating.

4. Conclusion

Transparency grating was succeeded to fabricate. Using the transparency grating, SGI lithography system and DGI lithography system were constructed to the BL3 beamline at NewSUBARU. Using SGI lithography combined with a bending magnet as a light source, 400 nm L&S pattern is replicated. In the calculation, partial coherent light is not suitable for SGI lithography, and DGI system can be used for the partial coherent light source. As a result, 28-nm L&S pattern can be replicated using dual grating system combined with the partial coherent light source as a bending magnet by computer simulation.

Furthermore, the DGI exposure method can be combined with a stand alone EUV source, such as laser produced plasma and discharge produced plasma. Therefore, this exposure system will become a compact one for the evaluation of resolution and LER in a EUV resist.

References

1. H. Kinoshita, K. Kurihara, Y. Ishii and Y. Torii: J. Vac. Sci. Technol. B 7 (1989) 1648.

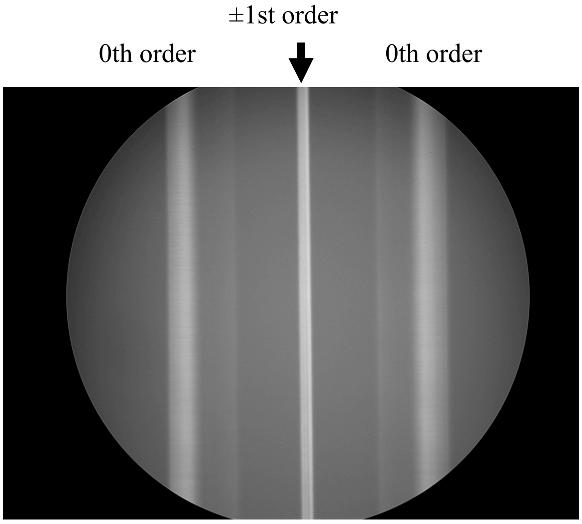

Fig. 9 Replicated ZEP520A resist pattern.

2. Three top issues in EUVL, EUVL international symposium 2007.

3. Roel Gronheid, Alan M. Myers, Frieda Van Roey, H.H.Solak, Yasin Ekinci, Tom Vandeweyer, Anne-Marie Goethals: presented at 2RE05, EUVL International Symposium 2006, Bercelona, Spain.

4. A. Yen, M.L. Schattenburg, H.I. Smith: Appl. Optics 31 (1992) 2972.

5. R. Tatchyn, E. Kallne, A. Toor, T. Cremer and P. Csonka: Rev. Sci. Instrum. 60 (1989) 1579.

6. H. H. Solak, D. He, W. Li, F. Cerrina, B. H. Sohn, X. M. Yang and P. F. Nealey: Appl. Phys. Lett. 75 (1999) 2328.

7. M. Wei , D. T. Attwood and T. K. Gustafson: J. Vac. Sci. Technol. B12 (1994) 3648.

8. H. H. Solak, C. David, J. Gobrecht , V. Golovkina, F. Cerrina , S. O. Kim and P. F. Nealey: Microelectron. Eng. 56 (2003) 67.

9 Pedrotti, Frank L.: Introduction to optics. (Prentice-Hall, New Jersey, 1987) p.317.1. T.Omote, “Polyimides”, M.Ghosh, and K.L.Miital, Eds., Dekker, New York, 1996, p.121.

Optimization of photo acid generator in the PAG-bonded resist

Yasuyuki Fukushima[1], Ryuji Ohnishi[1], Takeo Watanabe[1], Hideaki Shiotani[1],
Shouta Suzuki[1], Masamichi Hayakawa[2], Yusuke Endo[2], Tomotaka Yamanaka[2],
Shinichi Yusa[1], and Hiroo Kinoshita[1]

[1] LASTI/UH, [2] Toyo Gosei Kogyo Co., Ltd.
E-mail: takeo@lasti.u-hyogo.ac.jp

1. Introduction

Extreme ultraviolet lithography (EUVL) is the most promising technology for the fabrication of fine patterns of less than 32 nm node around 2010. Second issue of EUVL technology is resist development. The most significant issue is to simultaneously achieve high sensitivity and low line edge roughness (LER). For the method of reducing LER, it has to be taken account of uniform photo acid generator (PAG) density in a resist film. Since in the conventional chemically amplified (CA) resist, PAG and polymer mix in the solvent, PAG density in resist becomes non-uniform. Consequently, PAG was synthesized to the side chain of base resin to achieve uniform PAG density. As shown in Fig. 1, PAG density of a PAG-bonded resist seems to achieve higher uniformity rather than that of PAG blended resist. We developed and evaluated the PAG-bonded resist to satisfy the EUV specifications.

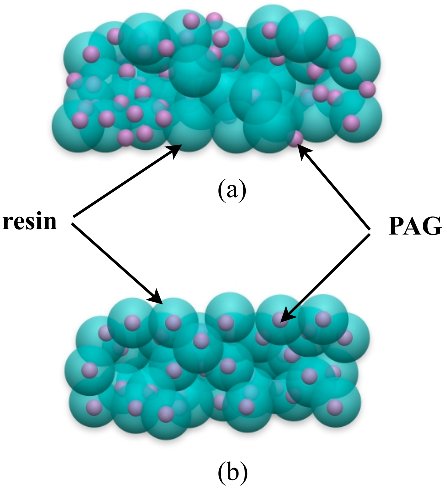

Fig. 1. (a) PAG blended resist and (b) PAG bonded resist.

2. Experiment

To confirm the superiority of a PAG-bonded resist, PAG blended resist which is consists of same base resin materials for the PAG-bonded base resin was used to compare LER under electron beam (EB) exposure. Chemical structure of the PAG-bonded resist and the PAG-blended resist are shown in Fig.2 (a) and Fig. 2 (b), respectively. We evaluated various PAG system for the improvement of the exposure characteristics of the PAG-bonded resist. The chemical structure of beneficial PAG is shown in Fig. 3.

The EUV sensitivity experiment was carried out using resist evaluation system installed at the BL3 beamline of NewSUBARU synchrotron radiation (SR) facility. E_0 sensitivity of the PAG-bonded resist and the PAG-blended resist were 5.0 mJ/cm^2 and 3.5 mJ/cm^2, respectively. Figure 4 and 5 show the photograph of SEM image of 75 nm lines and spaces (L/S) pattern of the PAG-bonded resist and the PAG-blended resist replicated by 30 kV EB writing tool. LER of the PAG-bonded resist and the PAG-blended resist were 3.5 (3σ) nm and 7.8 nm (3σ), respectively. Furthermore, 50 nm L/S pattern of the PAG-bonded resist could be observed. However, resist B could not resolve. Since using 30 kV EB writing tool, resolution of 50 nm is limited, 50 kV EB writing tool is used for the evaluation of the resolution. Figure 6 shows the photograph of SEM image of 55 nm lines and 25 nm spaces which is replicated by the 50 kV EB writing tool.

3. Summary

We developed and evaluated the PAG bonded resist that is a CA resist to reduce LER for EUVL. Under EUV exposure, E_0 sensitivity of the PAG-bonded resist was 5 mJ/cm^2. In order to clarify resolution and LER, EB exposure was performed, and LER of 3.5 nm (3σ) in 75 nm L/S was achieved by PAG bonded resist. A LER of PAG bonded resist is smaller than that of PAG blended resist. It can be considered that the PAG density of PAG bonded resist has higher uniformity than that of PAG blended resist. In addition, resolution of 25 nm was achieved by the 50 kV EB writing tool. It is confirmed that PAG bonded resist have characteristics of high resolution and low LER. We will discuss of the improvement of exposure characteristics using beneficial PAG group in the PAG-bonded resist.

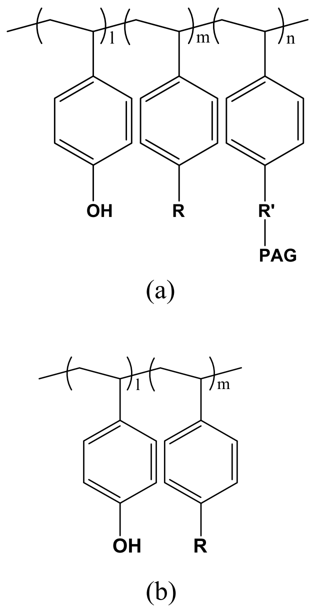

R, R': protection group

Fig. 2. Chemical structure of (a)PAG bonded resist.

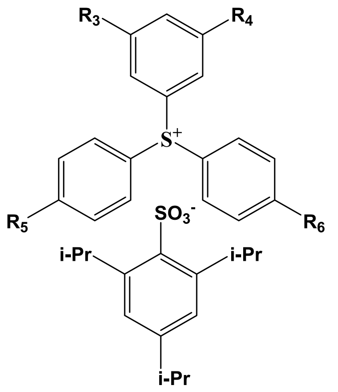

R_3, R_4: H, CH_3 R_5, R_6: H, CH_3, t-Bu

Fig. 3. Chemical structure of PAG and (b) PAB blended resist.

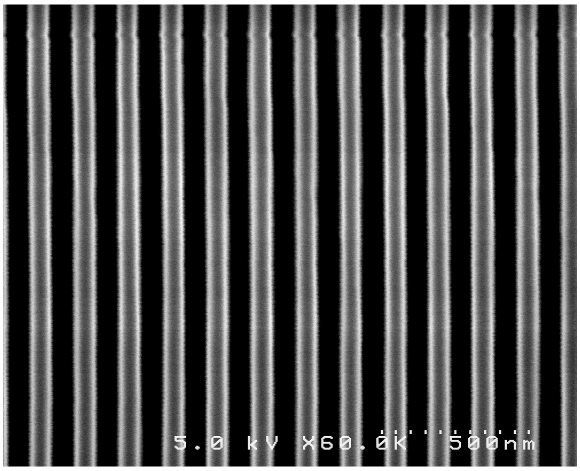

Fig. 4. The photograph of SEM image of 75 nm L/S pattern of PAG bonded resist.

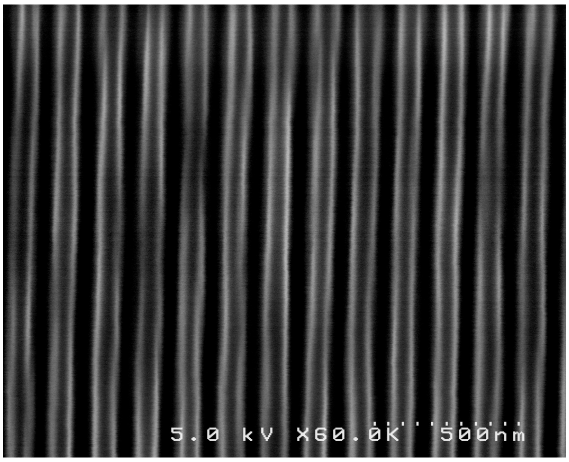

Fig. 5. The photograph of SEM image of 75 nm L/S pattern of PAG blended resist.

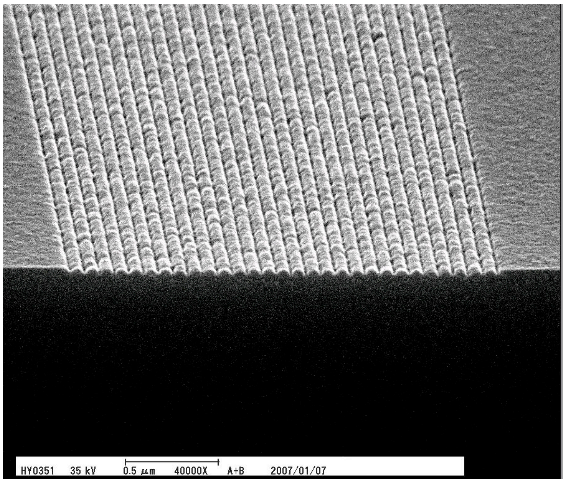

Fig.6. The photograph of SEM image of 55nm line and 25 nm space pattern of PAG bonded resist.

Mitigation of Low LER with PAG Bonded Resist for EUVL

Yasuyuki Fukushima, Takeo Watanabe, Ryuji Ohnishi, Hiroo Kinoshita, Hideaki
Shiotani, Shouta Suzuki, Masamichi Hayakawa*, Yusuke Endo*
Tomotaka Yamanaka* and Shinichi Yusa**

LASTI/UH, *Toyo Gosei Kogyo Co., Ltd.
**Graduate School of Engineering/ UH,

We developed and evaluated PAG bonded resist which is chemically amplified (CA) resist to reduce line edge roughness (LER) in extreme ultraviolet lithography (EUVL). Under electron beam (EB) exposure, it is compared that LER and resolution of photo acid generator (PAG) bonded resist and PAG blended resist which using same PAG and base polymer. It was found that LER and resolution of PAG bonded resist are better than that of PAG blended resist. LER of 3.5 nm in 75 nm L/S and resolution of 25 nm space were achieved. Under EUV exposure, sensitivity of 5.0 mJ/cm^2 is achieved.

Keywords: EUV resist, EB resist, line edge roughness, sensitivity

1. Introduction

Extreme ultraviolet lithography (EUVL)[1)] is the most promising technology for the fabrication of fine patterns of less than 32 nm node. EUVL is planned to transfer to the production line around 2010. Second issue of EUVL technology is resist development. EUV resist specification[2)] are 1) 18 nm resolution for a gate pattern, 2) 32 nm for dense pattern, sensitivity of less 2 mJ/cm^2, 3) line edge roughness less than 1.2 nm (3σ), 4) outgassing less than 1×10^{-6} Pa. Since LER and sensitivity are in trade off, it is very difficult to achieve LER and high sensitivity simultaneously. Required LER value is as same as molecule size of base resin. Thus molecule size control is required in the pattern width control.

To reduce LER in chemically amplified resist[3-5)], following five items have to take account such as, 1) controlling diffusion of acid, 2) low molecular weight 3) narrow dispersion molecular weight polymer and 4) uniform photo acid generator (PAG) density in resist film. Items 1) to 3) have been carried out. However it did not work well or had a problem for EUV resist.

Therefore, as a concrete method to achieve uniform acid density, PAG is synthesized to side chain of base resin. Since in the conventional chemically amplified (CA) resist, PAG and polymer mix in the solvent, the density of PAG in resist become heterogeneous[6)]. As shown in Fig. 1, PAG bonded resist seems to achieve higher uniformity rather than that of PAG blended resist.

In the previous paper[7)], it is demonstrated that PAG bonded resist has low LER and high sensitivity under electron beam. Futhermore, PAG bonded resist has high sensitivity under EUV exposure. However, the resolution was limited to 100 nm. Therefore, in this paper it is focused on to refine resolution of PAG bonded resist under EB exposure with keeping low LER and high sensitivity.

2. Experiment

2.1 Sample

For the method of increasing sensitivity, protection group which has a chemical structure with high absorption in EUV light was designed. In conventional protection group, de-protection reaction of protection group is occurred by acid which is generated during exposure from PAG. Furthermore, in novel protection group, since photo decomposition reaction is ocurred under EUV exposure. Therefore, novel resist system seems to have high sensitivity comparison to the conventional resist system such as ESCAP type resist.

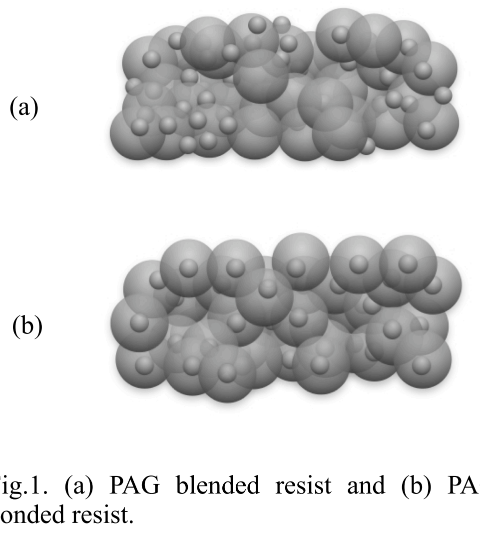

Fig.1. (a) PAG blended resist and (b) PAG bonded resist.

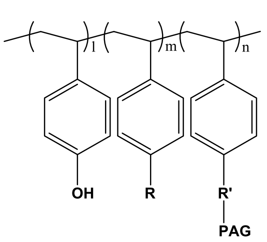

(a) (b)

R, R’: protection group

Fig. 2. Chemical structure of resists A and B.

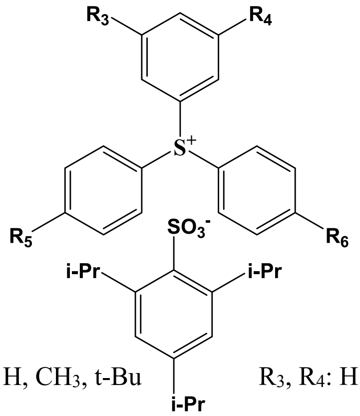

R_5, R_6: H, CH_3, t-Bu R_3, R_4: H, CH_3

Fig. 3. Chemical structure of PAG.

To confirm the superiority of PAG bonded resist, PAG blended resist which is consists of same base resin materials for PAG bonded base resin was used to compare LER under EB exposure. Chemical structure of PAG bonded resist and PAG blended resist are shown in Fig.2 (a) and Fig. 2 (b), respectively. Copolymer of hydroxy styrene was used as base resin, PAG which is shown in Fig. 3 was used as PAG, propylene glycol monomethylether acetate (PGMEA) was used as solvent. Molecular weight of synthesized resist was 16400 and molecular weight distribution was 1.09.

The details of composition of resist sample are shown in Table 1.

Table 1. The details of composition of resist sample.

Sample	Protection group	PAG	
		Amount	Type
Resist A	32.3 mol%	3.7 wt%	Bond
Resist B	32.1 mol%	3.7 wt%	Blend

2.2 Evaluation method

The sensitivity and outgassing experiment were carried out using resist evaluation system[8] installed at the BL3 beamline of NewSUBARU synchrotron radiation (SR) facility.

In the resist evaluation syste, it is simulating a six-mirror imaging optics for practical used for EUVL. SR light was mono-chromated to 13.5 nm wavelength by seven times reflection of concave mirror and two plane mirrors of Mo/Si mutilayer. Intensity of light was measured an electron current value of a photoelectron when EUV light irradiates to photoelectron plate. And it convert to the photon number of EUV light. Then, intensity of light was calculated from the photon number converted.

Furthermore, resist pattern was performed by EB writing system to evaluated resolution and LER. The acceleration voltages of EB writing system were 30 or 50 kV. The resist pattern image was obtained using scanning electron microscope (SEM) and LER was measured with a graphic processing computer software SuMMIT[9].

2.3 Process condition

The resist film was spin-coated on Si wafer and prebake was carried out on a hot plate at the temperature of 120 °C for 90 seconds to evaporate the solvent. The resist film thickness was controlled at 100 nm and measured by a multi-wavelength interference thickness measurement tool Nanospec model 6100A manufactured by NANOmetrics Co. Ltd. PEB was carried out on a hot plate at the temperature of 90 °C for 60 seconds after exposure. Aqueous 2.38 wt% of tetramethylammonium hydroxide (TMAH) was used as a developer at the temperature of 23 °C for 30 seconds and rinsed with de-ionized water.

3. Results and discussion

3.1. Sensitivity and outgassing measurement

Figure 4 shows sensitivity curve of resist samples under EUV exposure and Table 2 shows E_0 sensitivity of resist A and resist B.

E_0 sensitivity of resist A and B are 5.0 mJ/cm^2 and 3.5 mJ/cm^2, respectively. It shows that sensitivity of PAG blended resist is higher than that of PAG bonded resist. Since it is thought that polymer agglutinates to wrap up PAG, it is consider that acid is hard to diffuse during PEB process.

The outgassing is measured using high sensitive quadrupole mass spectrometer. Total outgassing displacement between after exposure and before exposure was measured. The measured mass range was 1 amu to 500 amu. Table 3 shows total outgassing pressure of resist A and resist B.

Table 2. E_0 sensitivity of resist A and B

Sample	E_0 sensitivity
Resist A	5.0 mJ/cm^2
Resist B	3.5 mJ/cm^2

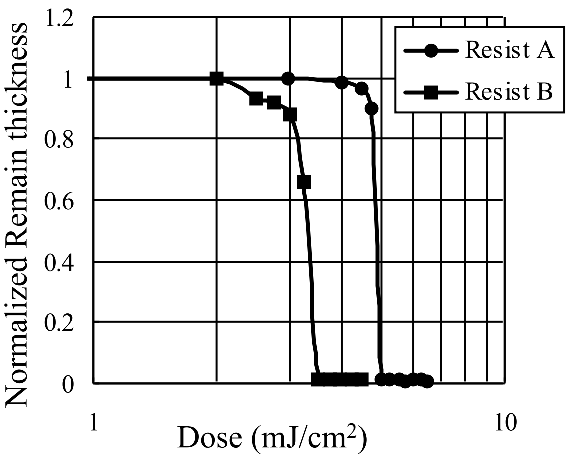

Fig. 4. Sensitivity curve of resist samples.

Table 3. Total outgas pressure of resist sample

Sample	Total outgas pressure
Resist A	3.46×10^{-6} Pa
Resist B	4.33×10^{-6} Pa

The total ougassing pressure of resist A and B are 3.46×10^{-6} Pa and 4.33×10^{-6} Pa, respectively. Furthermore, a lot of molecular weight own to a protection group was detected. As a result, it is thought that protection group is decomposed under EUV exposure. Total outgassing of resist A have not big difference between total outgassing of resist B because of similar base resin chemical structure.

3.2. Resolution and LER evaluation

Figure 5 shows the photograph of SEM image of resist A replicated by EB writing system ELIONIX 3700 The acceleration voltage of EB writing system was 30 kV. 75 nm line and space pattern was observed. Sensitivity and LER are 16.0 μC/cm² and 3.5 nm (3σ), respectively.

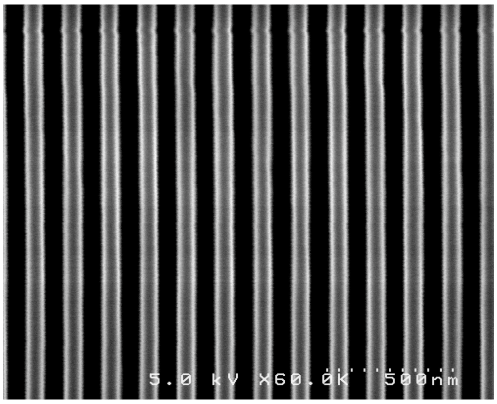

Fig.5. The photograph of SEM image of resist A

Figure 6 shows the photograph of SEM image of resist B. 75 nm line and space pattern was observed. A sensitivity and LER are 7.5 μC/cm² and 7.8 nm (3σ), respectively.

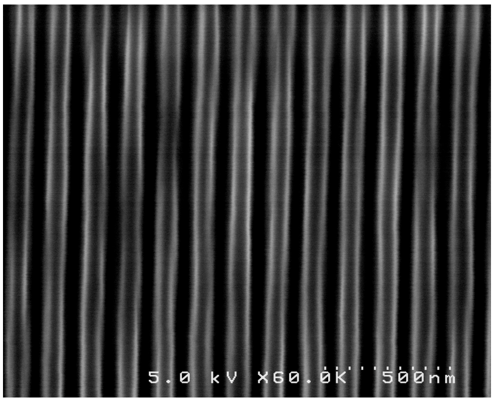

Fig. 6. The photograph of SEM image of resist B

It was confirmed that LER of PAG bonded resist was smaller than that of PAG blended resist. As a result, it is sure that uniformity of PAG in PAG bonded base resin has higher uniformity than that of PAG blended resist. Furthermore, 50 nm L/S pattern of resist A could be observed. However, resist B could not resovle.

Figure 7, 8, 9 show the photograph of SEM image of 90 nm line and 60 nm space, 62.5 nm line and 37.5 nm space, and 55 nm line and 25 nm space of resist A, respectively. The acceleration voltage of EB writing system was carried out at 50 kV using ELIONIX 7500. It is conformed that resist A has a capability to resolve 25 nm.

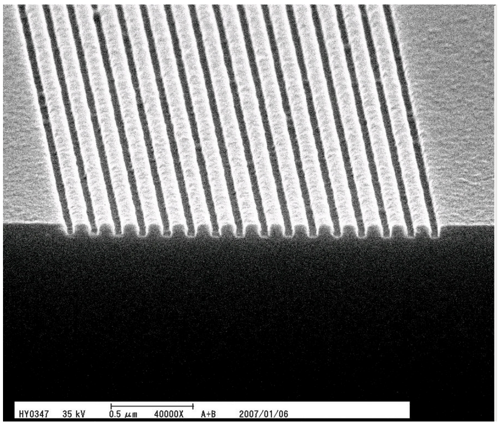

Fig. 7. The photograph of SEM image of 90 nm line and 60 nm space of resist A

4. Conclusion

We developed and evaluated PAG bonded resist which is chemically amplified (CA) resist to reduce line edge roughness (LER) for extreme ultraviolet lithography (EUVL).

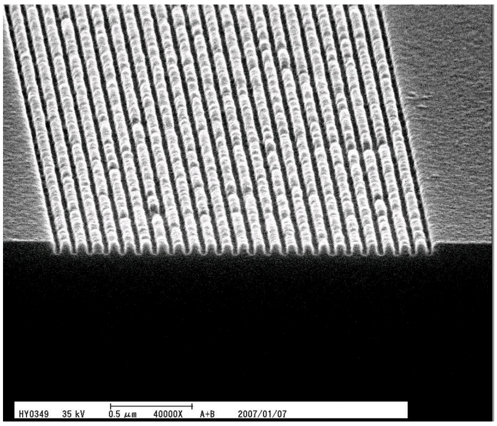

Fig. 8. The photograph of SEM image of 62.5 nm line and 37.5 nm space of resist A.

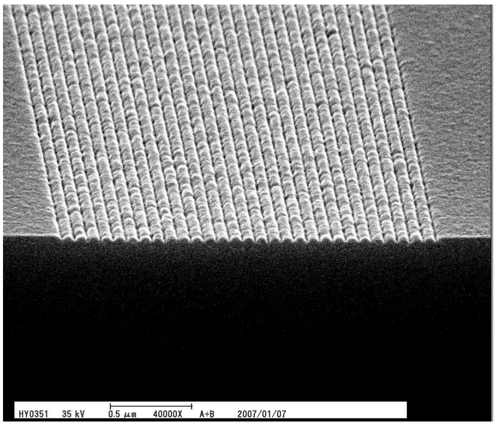

Fig. 9. The photograph of SEM image of 55 nm line and 25 nm space of resist A.

Under electron beam (EB) exposure, it is compared that LER and resolution of photo acid generator (PAG) bonded resist and PAG blended resist which using same PAG and base polymer. E_0 sensitivity of resist A was 5.0 mJ/cm^2 under EUV exposure.

Total outgas pressure of resist A was 3.46×10^{-6} Pa, and a lot of molecular weight of protection group was detected.

In order to clarify resolution and LER, EB exposure was performed, and LER of 3.5 nm (3σ) in 75 nm L/S was achieved by PAG bonded resist. A LER of PAG bonded resist is smaller than that of PAG blended resist. It can be considered that the PAG density of PAG bonded resist has higher uniformity than that of PAG blended resist.

In addition, resolution of 55 nm line and 25 nm space was achieved when the acceleration voltage of EB writing system was 50 kV. It is confirmed that PAG bonded resist have characteristics of high resolution and low LER.

In the next stage, LER and resolution of PAG bonded resist will be evaluated using EUV interference lithography.

References

1. H. Kinoshita, K. Kurihara, Y. Ishii and Y. Torii: J. Vac. Sci. Technol. B7(1989) 1648.
2. W. Yueh, H. Cao, M. Chandhok, S. Lee, M. Shumway and J. Bokor: Proc. SPIE. 5376 (2004).
3. H. Ito: Journal of Research, 1997-research.ibm.com
4. H. Ito:J. Polym. Sci., PartA, Polm. Chem. 41, 3863 (2003)
5. H. Ito: Proc. SPIE. 3678 (1999)
6. Proceeding of 15th lecture Meeting of photo-reactions and electric materials, the society of polymer and science, pp.15-18, 2006.
7. T. Watanabe, Y. Fukushima, H. Shiotani, M.Hayakawa, S. Ogi, Y. Endo, T. Yamamoto, S. Yusa and H. Kinoshita: J.Photopolym. Sci. Technol. 19 (2006) 521
8. T. Watanabe, H. Kinoshita, N. Sakaya, T. Shoki, S. Y. Lee:Jpn. J. Apply. Phys. 44 (2005) 5556
9. Developed by Patrick Naulleau, informed at URL: http://www.euvl.com/summit

SR irradiation effect of high-hydrogenated DLC thin films in the soft X-ray region

Kazuhiro Kanda[1], Masahito Niibe[1], Masahito Tagawa[2], Kumiko Yokota[2], Hiroki Akasaka[3], Hidetoshi Saitoh[3] and Shinji Matsui[1]
[1] Laboratory of Advanced Science and Technology for Industry, University of Hyogo
[2] Graduate School of Engineering, Kobe University
[3] Department of Materials Science and Technology, Nagaoka University of Technology

abstract

The effect of irradiation of synchrotron radiation to high-hydrogenated DLC thin films was investigated. Etching of films, department of hydrogen from films and change of local structure were founded.

Introduction

General DLC films are ablated by the exposure to the synchrotron radiation (SR) in the soft x-ray region under O_2 atmosphere, while they are not etched by the exposure to the SR in the soft x-ray region in the vacuum. On the other hand, the irradiation of soft x-ray in the vacuum against high-hydrogenated DLC (H-DLC) films bring about the departure of hydrogen. In the present study, the variation of local structure of high-hydrogenated DLC thin films by the irradiation of soft X-ray in the vacuum was investigated.

Experimental

High-hydrogenated DLC thin films were deposited by amplitude-modulated RF plasma-CVD. The film thickness was 200 nm. The irradiation of soft X-ray against DLC films was carried out at BL-6 of NewSUBARU. The SR at the BL-6 sample stage had a continuous spectrum from IR to soft X-ray, which was lower than 1 keV. The SR dose was represented by the product of the ring current with the exposure time. The irradiation of SR was performed at room temperature and the increase of substrate temperature was not found.

Results and discussion

Figure 1 depicts the SR dose dependences of the etching depth of high-hydrogenated DLC thin film by the SR irradiation. The depth of etching was measured with DEKTAK(ULVAC; 6M). The etching depth increased almost linearly with SR dose in the SR dose range of 0-150 mA·h.

The change of density of DLC film by the soft X ray irradiation was measured using the X-ray reflectometer. Measured angle dependences of the reflectivity of H-DLC films as deposition and after irradiation of 3600 mA·h were depicted in Fig. 2.
Critical angle and vibrational period were varied by the SR irradiation. The film density was found to increase from 1.45 g/cm^3 to 1.80 g/cm^3.

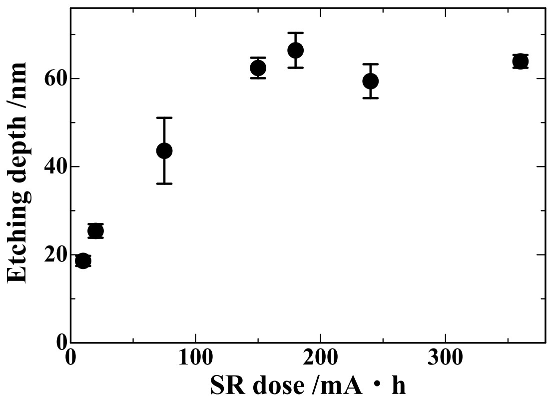

Fig. 1 The SR dose dependences of the etching depth of high-hydrogenated DLC thin film by the SR irradiation.

Rutherford backscattering spectrometry (RBS) and elastic recoil detection analysis (ERDA) are

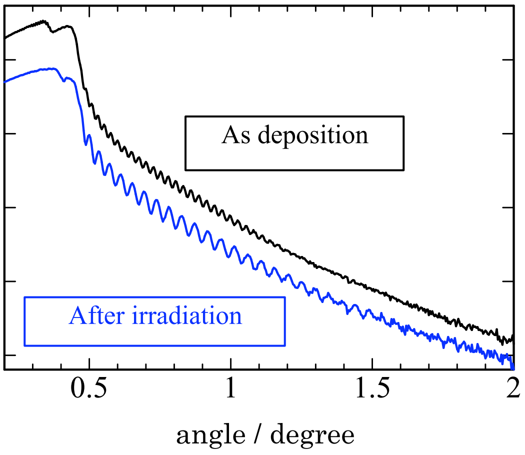

Fig. 2 XRR spectra of H-DLC films as deposition and after irradiation of 3600 mA·h.

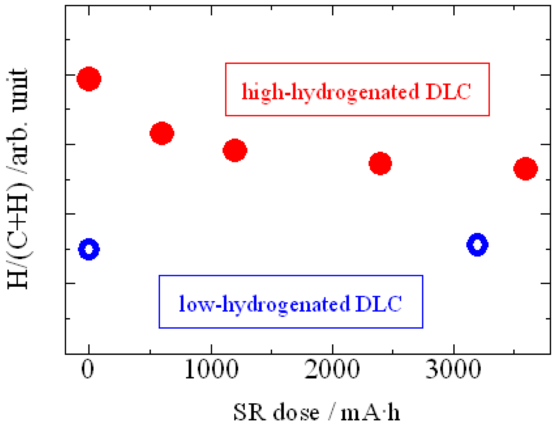

Fig. 3 The SR dose dependences of the hydrogen content of high-hydrogenated DLC thin film and low-hydrogenated DLC thin film.

available for evaluating quantitative determination for all elemental composition, specially hydrogen, of thin films with high accuracy, being unnecessary for standard samples. In this study, the hydrogen content of DLC film has been determined by RBS and ERDA techniques using a tandem Pelletron accelerator, 5SDH-2 in the Kobe University.

As shown in Fig. 3, the hydrogen content in the low-hydrogenated DLC film kept constant independent on a soft X-ray exposure dose. On the other hand, that in the high-hydrogenated DLC film decreases exponentially with a soft X-ray exposure dose. Thus, the departure of the hydrogen was observed from high-hydrogenated DLC films, while was not observed from the low-hydrogenated DLC film by soft X-ray irradiation.

To examine a change of the local structure of high-hydrogenated DLC film by the departure of hydrogen, Near Edge X-ray Absorption Fine Structure (NEXAFS) spectra were measured at NewSUBARU BL-9. Photocurrent coming from a sample was detected in the total electron yield. The NEXAFS spectrum of carbon K edge absorption was measured in the range of 275-320 eV with the resolving power of 0.5 eV FWHM. In the NEXAFS spectrum of the high-hydrogenated DLC film before the soft X-ray irradiation, structural peaks were observed in the 286-310 eV. This is interpreted by the construction of specific structures in the DLC film, corresponding to a large amount of hydrogen atom. These structural peaks disappear after the soft X-ray irradiation and spectral profiles get close to those of general DLC films well. The intensity of 285.4 eV, corresponding to sp2 structure increased with the exposure doses of the soft X ray. Therefore, the sp2 structure in the DLC film increases by the departure of the hydrogen.

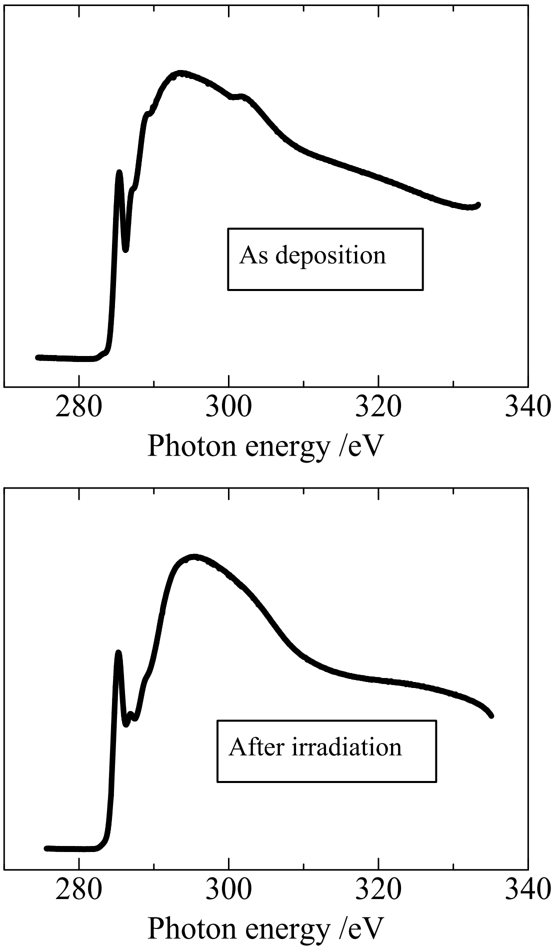

Fig. 4 C K-edge NEXAFS spectra of H-DLC film as deposition (upper) and that after SR irradiation of 3600 mA·h (lower)

Structural Changes in the DLC Films Fabricated using Ga Focused Ion Beam Assisted Deposition by Heat Treatment

Kazuhiro Kanda[1], Makoto Okada[1], Yuji Kang[1], Tsuneo Suzuki[2], and Shinji Matsui[1]

[1] LASTI, Graduate School of Science, University of Hyogo
[2] Extreme Energy-Density Research Institute, Nagaoka University of Technology

abstract

The annealing effect on a diamond-like carbon (DLC) thin film fabricated by focused-ion-beam chemical-vapor deposition (FIB-CVD) was investigated. Elementary analysis, using Rutherford backscattering spectrometry and elastic recoil detection analysis were performed on the FIB-CVD DLC thin film by annealing in the various annealing condition. It was found that the Ga in the middle layer in the FIB-CVD DLC film promptly departed and that department of hydrogen was slower than that of Ga.

Introduction

Ga Focused-ion-beam chemical-vapor deposition (FIB-CVD) method is developed as an effective technique for producing of three-dimensional nanostructures. In this method, scanning of focused Ga ion beam under the phenanthrene gas atmosphere leads to deposition of carbon material at arbitrary nanoscale area. It was known that the fundamental structure of carbon material formed by FIB–CVD consists of the DLC core, which contains Ga as an ion source, and surface layer, which was composed of pure diamond-like carbon (DLC). In addition, this residual Ga in the FIB-CVD DLC film moved to the neighboring surface and departed from the film surface by the annealing, from the angle-dependent measurement of C K-edge NEXAFS spectrum [1]. In our previous work, Ga content in the FIB-CVD DLC thin film decreased from 3.6 % to trace mount by the annealing for 1 hour at 1023 K, from Rutherford backscattering spectrometry (RBS) [2]. In the present study, we measured the RBS spectrum and elastic recoil detection analysis (ERDA) spectrum by the variation of annealing condition of FIB-CVD DLC film. As a result, the novel information on departure process of Ga from FIB-CVD DLC film was acquired.

Experimental

Ga FIB-CVD DLC films were formed on a Si substrate surface using a commercially available FIB-CVD system (SII Nano Technology, SMI2050MS) with a Ga^+ ion beam operating at 30 keV. The area and thickness of the produced FIB-CVD DLC films were 10×10 mm^2 and $\approx$200 nm, respectively. The samples were kept in the vacuum annealing apparatus during 32 hour. The annealing temperature was varied from 673 K to 973 K.

The atomic fraction of Ga in the sample was determined by the measurement of RBS and ERDA. RBS and ERDA with MeV-He^+ irradiation were performed using an electrostatic accelerator (Nisshin-High Voltage, NT-1700HS) located at the Extreme Energy Density Research Institute, Nagaoka University of Technology.

Results and discussion

Figure 1 shows Ga profiles in the RBS spectra. In the FIB-CVD DLC film as deposition, the profile of Ga shows rectangular, which means that Ga populated equally in the core of the FIB-CVD film, which contains Ga. After annealing, the content of Ga decreased and the profile of Ga was split to two peaks. This profile indicates that the Ga in the middle layer in the FIB-CVD DLC film was almost lost, and the Ga in the vicinity of surface and interface remained. It was known that the residual Ga moves easily in the FIB-CVD DLC film and forms spheres surrounded by graphite shell on the film surface by annealing treatment [3]. The moving velocities of Ga in the vicinity of interface and surface were considered to be smaller than that in the middle DLC layer, because the diffusion coefficients in the Si substrate and in the graphite shell were smaller than that in the amorphous carbon.

Fig. 2 shows the annealing time dependence of Ga and H contents of FIB-CVD DLC film. The Ga

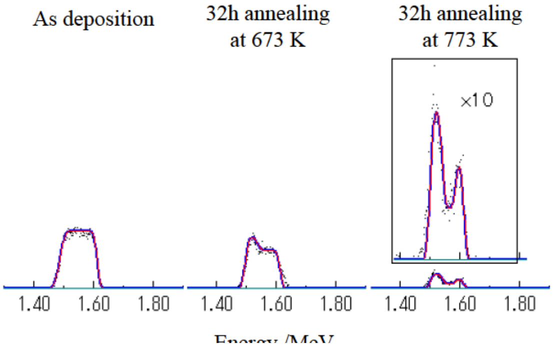

Fig. 1 Ga profiles in the RBS spectra.

content in the as-deposited FIB-CVD DLC film, ≈5 at %, decreased with an increase in annealing time in exponential law, while H content almost not varied.

Fig. 3 was depicted the annealing time dependence of Ga and H contents. The Ga content slightly decreased with an increase in annealing temperature from room temperature to 673 K and considerably decreased with an increase from 673 to 773 K. On the other hand, the H content decreased with an increase in annealing temperature from 673 to 973 K, but a certain mount of H (≈7 at %) was observed in the FIB-CVD DLC film after 32 h annealing at 973 K. As a result, the residue Ga in the FIB-CVD DLC film almost departed from the film at 673 K, which was a lower temperature than the desorption of H in the DLC film.

References

[1] A. Saikubo, K. Kanda, Y. Kato, J. Igaki, R. Kometani, et. al., Jpn. J. Appl. Phys. 46 (2007) 7512.

[2] K. Kanda, J. Igaki, A. Saikubo, R. Kometani, T. Suzuki, et. al., Jpn. J. Appl. Phys. 47 (2008) 7464.

[3] R. Kometani, S. Ishihara, K. Kanda, Y. Haruyama, et. al., Jpn. J. Appl. Phys. 47 (2008) 5032-5035.

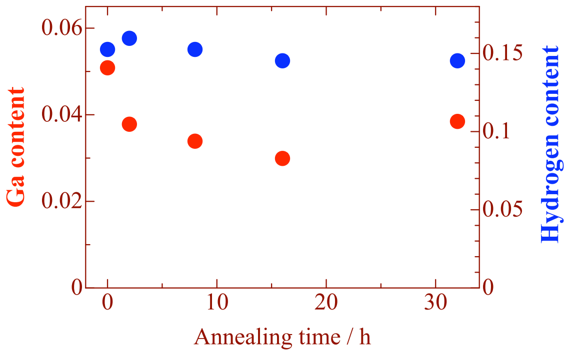

Fig. 2 Annealing time dependence of elementary composition of FIB-CVD DLC film at the annealing temperature of 673 K.

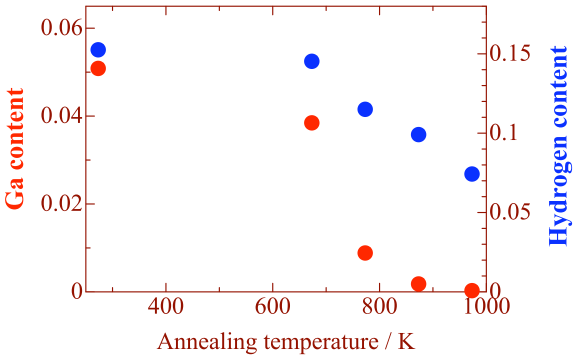

Fig. 3 Annealing temperature dependence of elementary composition of FIB-CVD DLC film after 32 h annealing.

Atomic Movement in a-Si Film by Soft X-ray irradiation

Akira Heya, Yasuyuki Takanashi, Kazuhiro Kanda and Naoto Matsuo
University of Hyogo

Abstract

Atomic movement in a-Si film by soft X-ray irradiation was investigated for low-temperature crystallization. a-Si films were irradiated at storage electron energy of 1GeV, photon energy of 115eV and irradiation quantity of 50mA*hours and storage-ring current were varied from 50 to 175mA. a-Si film was crystallized above storage-ring current of 175mA. It is considered that crystallization temperature at this condition was low compared with conventional thermal crystallization. It is considered that the soft X-ray irradiation enhanced atomic movement in a-Si film.

Introduction

Flexible organic light emitting diode (OLED) display is one of the most expected displays for next generation because of its light weight and flexibility. Polycrystalline silicon (poly-Si) films prepared below 200 °C is necessary as material of thin film transistor (TFT) in flexible displays. The poly-Si films prepared by crystallization of amorphous silicon (a-Si) using excimer laser annealing (ELA) have been investigated widely. However, it is difficult to realize low-temperature process for ELA method.

We have tried to crystallize a-Si film using soft X-ray irradiation [1-3]. It is confirmed that a-Si film crystallized at storage-ring current of 220mA, storage electron energy of 1GeV, photon energy of 115eV and irradiation quantity of 1000mA*hours. However, in this irradiation condition, it is afraid that sample temperature was high.

In this study, the sample temperature was measured by an infrared thermometer and a thermocouple attached on sample. In addition, a-Si film was irradiated at various storage-ring currents (50 to 175mA).

Experiments and Results

1) Sample temperature during soft X-ray irradiation

a-Si films with 50nm thickness were deposited by plasma enhanced chemical vapor deposition method on SiO_2/glass substrates. The temperature of a-Si/SiO_2/glass substrate was measured by a thermocouple (K type) attached on sample (10×10 mm^2 in size). The temperature distribution was obtained by moving of sample position. The measurement conditions were at storage electron energy of 1GeV, storage ring current of 220mA and photon energy of 115eV.

The temperature distribution is shown in Fig. 1. The maximum and minimum temperature was 680℃ and 340℃, respectively. It is shown that difference in temperature was large in spite of small sample because soft X-ray beam size is small and thermal conductivity of glass substrate is low. The maximum temperature was comparable with crystallization temperature for conventional furnace annealing. Therefore it is necessary to decrease sample temperature for low-temperature crystallization.

2) a-Si films irradiated at various storage-ring current

a-Si/SiO_2/glass substrate was irradiated at storage electron energy of 1GeV, photon energy of 115eV and irradiation quantity of 50mA*hours. Storage-ring current were varied from 50 to 175mA for decrease in sample temperature. The irradiation time for the storage-ring current of 50, 75, 100, 125, 150 and 175mA were 60, 40, 30, 24, 20 and 16min, respectively.

The Raman spectra of Si film irradiated at various storage-ring current are shown in Fig. 2. The peak due to amorphous phase (480cm^{-1}) was observed at a-Si films irradiated below 150mA. On the other hand, a-Si film was crystallized at

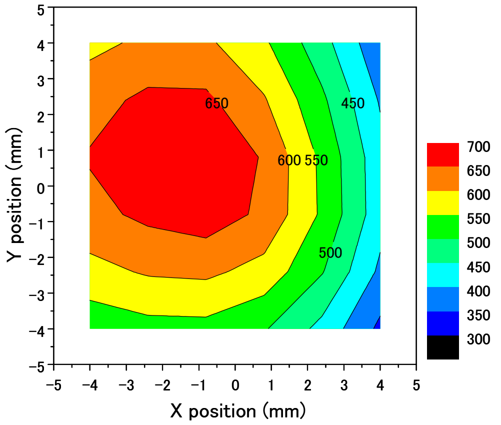

Fig. 1. Sample temperature distribution during soft X-ray irradiation at storage electron energy of 1GeV, storage ring current of 220mA and photon energy of 115eV.

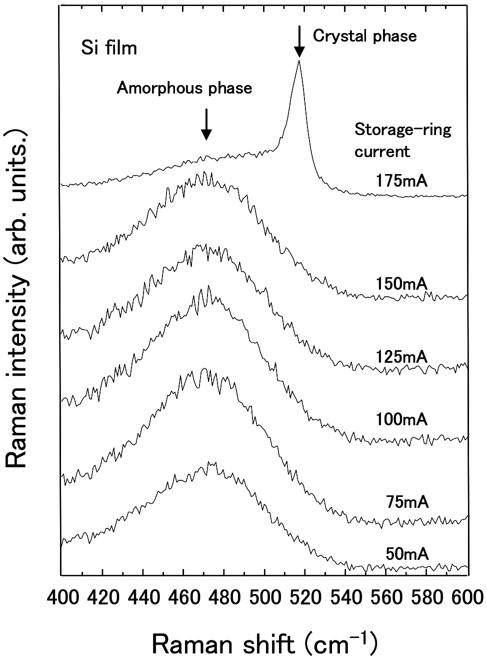

Fig. 2. Raman spectra of Si film irradiated at various storage-ring current. a-Si films were irradiated at storage electron energy of 1GeV, photon energy of 115eV and irradiation quantity of 50mA*hours.

ring current of 175mA. The sample temperature estimated by thermo tape at 100mA were 300℃. The collect sample temperature at storage-ring current of 175mA is not clear. However, this temperature can be estimated to 500℃ by assuming that as the sample temperature increased linearly with increasing the storage-ring current. It is found that a-Si was crystallized at low temperature compared with a conventional furnace annealing.

The crystallization mechanism for the conventional thermal annealing and the thermal annealing with soft X-ray irradiation are shown in Fig. 3. Si atoms can be moved by photon excitation during soft X-ray irradiation and Si atoms are ordered locally. We call this region the quasi-nucleus. It is considered that the radius of the quasi-nucleus was small compared with the critical radius for crystallization. The quasi-nucleus grew to crystal grain with critical radius for crystallization despite low-temperature annealing. In this case, crystal grains can be grown without nucleation energy in the crystallization process because the quasi-nucleus was already formed. Therefore, the critical temperature for crystallization was decreased by soft X-ray irradiation because of the generation of a quasi-nucleus. It is found that soft X-ray irradiation can be expected for low-temperature crystallization of a-Si film.

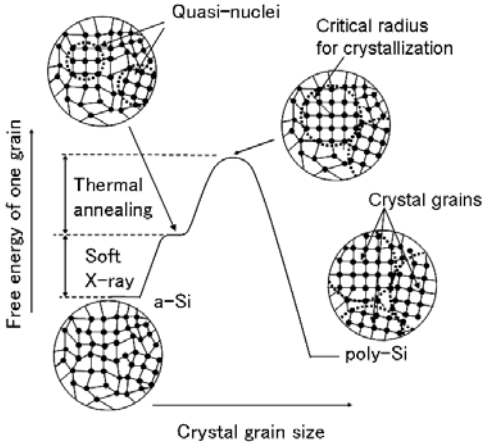

Fig.3. Crystallization mechanism during soft X-ray irradiation. Quasi-nuclei were formed by soft X-ray irradiation. The critical temperature for crystallization was decreased by soft X-ray irradiation.

References

[1] N. Matsuo, T. Mochizuki, S. Miyamoto, K. Kanda, N. Tanaka, and N. Kawamoto: Dig. AM-LCD, 2005, p.293.
[2] N. Matsuo, K. Uejyukkoku, A. Heya, S. Amano, Y. Takanashi, S. Miyamoto, and T. Mochizuki: Jpn. J. Appl. Phys. **46** (2007) 1061.
[3] A. Heya, Y. Takanashi, S. Amano, N. Matsuo, S. Miyamoto, and T. Mochizuki: Jpn. J. Appl. Phys. **48** (2009) 050208.

Opening of Material Analysis Beamline at BL-5 for Industrial Enterprises

T. Hasegawa[1], M. Uemura[1], M. Motoyama[2], and K. Kanda[2]
1 Synchrotron Analysis L.L.C., Hyogo-ku, Kobe, Hyogo 652-0863 Japan
2 University of Hyogo, Kamigori, Ako, Hyogo 678-1205 Japan

Abstract

An analysis beamline with high energy-resolution begins to supply at BL-5 for the industrial enterprises' use. BL-5 consists of two branch lines for the use in the high-energy region and low-energy region, respectively. These two branch lines can be employed simultaneously. The whole useful energy range of the BL-5 is the region from 50 to 4000 eV and X-ray absorption spectrum of every atom from Li to Sn can be measured using this line. BL-5 will be managed and maintained by the Synchrotron Analysis L.L.C. (SALLC), which is composed by the industrial companies.

Introduction

Attendant upon the quick development of nano-technology industry, demand for material analysis in the soft X-ray region has increased rapidly. For instance, the analysis of the soft X-ray region is an important major technology in the research and development and the manufacturing enterprise of a high-technology material and the device. X-ray absorption fine structure (XAFS) technique in the soft X-ray region has attracted much attention from analysis industry as a powerful tool to investigate the electronic states and geometric structures of industrial materials. In addition, photoemission spectroscopy (PES) technique is also an effective analysis method to research the electronic structure of material surfaces in the ultra-soft x-ray region. Hyogo prefecture constructed a new beamline at BL-5 of NewSUBARU in reply to the demand of industrial societies. In the construction of this beamline, cooperation of University of Hyogo with private enterprises is expected to prosper the co-research with University of Hyogo and advance of the analysis technique of analysis industry in Hyogo prefecture.

Layout of BL-5

The light source of BL-5 is the bending magnet, which can provide the photon in the region up to 4000 eV. BL-5 consists of two branch lines for the use in the wide range from 50 eV to 4000 eV. BL-5A, which is mounted with a double crystal monochromator, can be used in the energy range of 1300-4000 eV. On the other hand, BL-5B is mounted with a varied line spacing grating (VLSPG) monochromator, which is designed to cover the energy range 50-1300 eV with three gratings. The incident beam from the bending magnet is provided for two branch lines through the different windows of mask. These two branch lines can be employed simultaneously.

Specifications of BL-5A

An optical arrangement of the BL-5A is shown in Fig. 1. InSb crystals and Si crystals are prepared for a double crystal monochromator. Toroidal mirrors are used as a pre-mirror and a focusing mirror of BL-5A, for the purpose to introduce a high-photon flux to the end station. The XAFS in the total electron yield (TEY) mode and fluorescence XAFS measurement using SSD (SII Vortex) can be performed. The fluorescence XAFS spectra can be measured samples at the under an atmospheric pressure by the replacement of an end station to He using Be window.

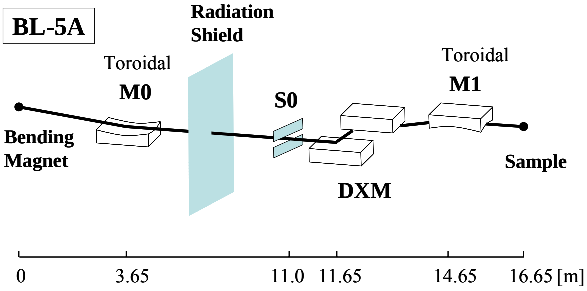

Fig.1 Optical layout of BL-5A

Specifications of BL-5B

The constant-deviation monochromator consisting of a demagnifying spherical mirror and VLSPG, which can provide to high resolution, simple wavelength scanning with fixed slits, was mounted on BL-5B. An optical arrangement of the BL-5B is shown in Fig. 2.

The optical system consists of a first mirror (M0), a second mirror (M1), an entrance slit (S1), a pre-mirror (M2), and three kinds of plane grating (G), an exit slit (S2) and a focusing mirror (Mf). The including angle of the monochromator is 175°. Two measurement chambers are prepared at the end station of BL-5B. The XAFS spectra in the total electron yield mode and fluorescence XAFS spectra using SDD (EDAX) can be measurement in the high vacuum chamber. In addition, the photoelectron

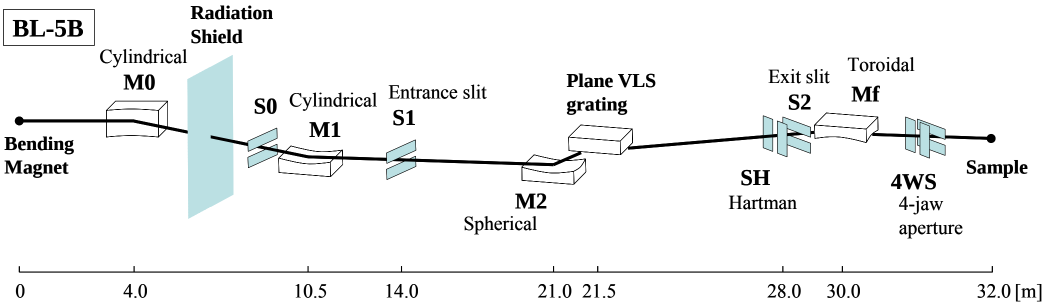

Fig.2 Optical layout of BL-5B

spectra using spherical electron analyzer (VG Scienta, R3000) can be measured in the ultra high vacuum chamber. These chambers can be replaced each other within 1 hour. Each chamber can maintain 16 samples of 25 mm corner because of industrial use.

Measurement

In BL-5B, absorption spectra by means of the TEY method were obtained for standard samples in the soft X-ray region. The carbon K-edge near-edge X-ray absorption fine structure (NEXAFS) spectrum of graphite is shown in Fig.3. The spectrum have been normalized to I_0 and had a linear pre-edge background removed. The peak at 285.4 eV [1] appears clearly, which is due to C1s→π^* transition. Additionally, the absorption spectra by means of the TEY method were obtained for *h*-BN powder. The boron and nitrogen K-edge NEXAFS spectrum of *h*-BN are shown in Fig.4 and Fig.5, respectively.

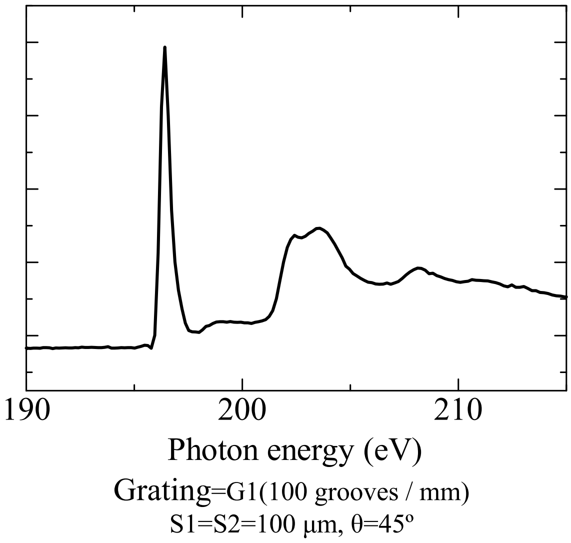

Fig.4 *h*-BN B K-edge NEXAFS spectrum

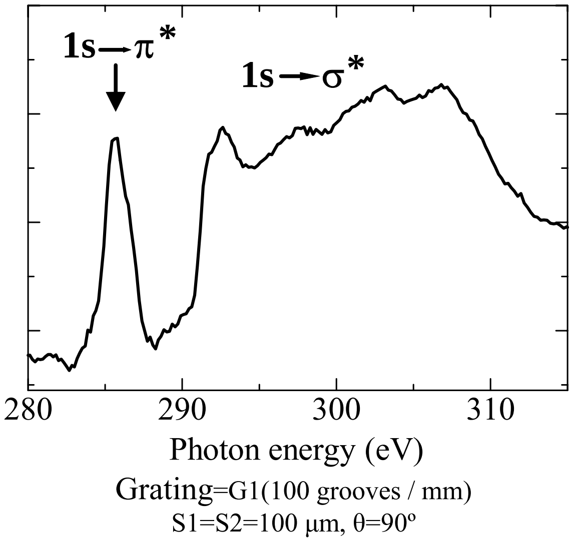

Fig.3 Graphite C K-edge NEXAFS spectrum

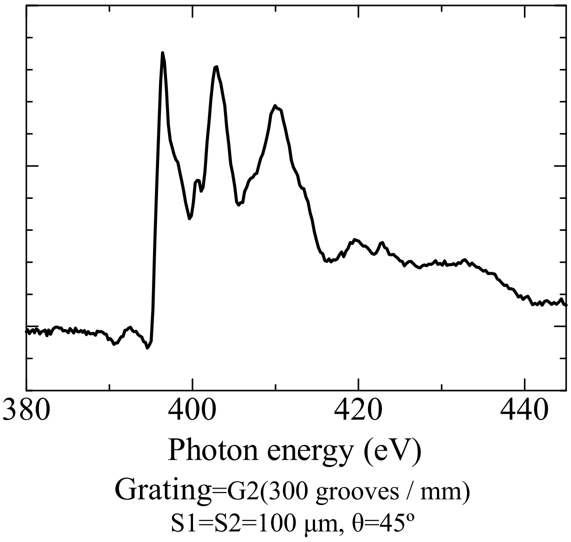

Fig.5 *h*-BN N K-edge NEXAFS spectrum

References

[1] P. E. Batson: Phys. Rev. B **48** (1993) 2608.

Photoemission study of the Au-SrTiO$_3$(100) surface

Yuichi Haruyama, Yoshihiro Aiura[1], Hiroshi Bando[1], Shinji Matsui
Graduate School of Science and LASTI, University of Hyogo
[1]National Institute of Advanced Industrial Science and Technology, AIST Tsukuba

Abstract

We have investigated the Au-SrTiO$_3$(100) interface as a function of the Au evaporation using the photoemission spectroscopy. In the valence band of SrTiO$_3$, the broad state originating from O 2p electrons and a state from Ti 3d electrons were observed between 3-9 eV and at 1 eV below the Fermi level (E_F), respectively. With increasing the Au evaporation, the decrease in intensity of the state at 1 eV was observed. In the Ti 3p core-level, the decrease of the Ti^{3+} states was observed after Au evaporation. These results indicate that the electrons transfer from the Ti^{3+} states of the SrTiO$_3$(100) surface to the evaporated Au.

Introduction

Since Haruta *et al.* discovered the catalytic property of Au atoms on the transition metal oxide surface [1], many studies on the electronic and geometric structures of Au-transition metal oxide interface have been performed so far [2]. Particularly, the strong catalytic property was found in Au clusters on the transition metal oxide with the size of less than 10 nm, and the oxidation of CO and the epoxidation of C_3H_6 were observed even at low temperature [2]. In this study, we studied the electronic structures of the Au-SrTiO$_3$(100) surface as a function of the Au evaporation using the photoemission spectroscopy.

Results and Discussion

In Fig. 1, a photoemission spectrum of the Ti 3p, O 2s, and Sr 4p core-levels before Au evaporation is compared to that after Au evaporation of 5 Å. In each Ti 3p, O 2s, and Sr 4p core-level, the shift of the peak to lower binding energy side by 0.2 eV was observed after Au evaporation. In addition, the intensity of the peak at ~35.5 eV decreased after Au evaporation. In the previous photoemission study of the Ti 3p core-level, the peaks at ~37.8 and ~35.5 eV were assigned to the Ti^{4+} and Ti^{3+} states, respectively. The Ti^{3+} states were produced by the transfer of a electron to the Ti sites next to the surface oxygen vacancies when the surface oxygen vacancies were formed. Therefore, the decrease of the Ti^{3+} states after Au evaporation means that the electrons transfer from Ti^{3+} states tothe states to the evaporated Au atoms. Before Au evaporation, the Sr $3d_{5/2}$ peak was located at 133.9 eV. With increasing the Au evaporation at 5 Å, the peak at ~133.9 eV shifted to lower binding energy side by 0.2 eV. The shift of the peak in the Sr 4p core-level is identical to that in the Ti 3p, O 2s, and Sr 3d core-levels. In the previous photoemission study of the annealed SrTiO$_3$ surface, the band bending effect caused by the surface Ti^{3+} states was observed. Therefore, the shifts of the Ti 3p, O 2s, Sr 3d, and Sr 4p core-levels after Au evaporation are basically ascribed to the band bending effect caused by the decrease of the surface Ti^{3+} states.

Figure 2 shows the photoemission spectra of the Au 4f core-level as a function of the Au evaporation. All spectra display Au $4f_{7/2}$ and $4f_{5/2}$ spin-orbit doublet peaks located at ~84.4 and ~88.0 eV, respectively. At 0.5 Å, the Au $4f_{7/2}$ peak was located at 84.4 eV. With increasing the Au evaporation at 1 Å, the width of the peak at ~84.4 eV decreased drastically. In addition, the peak at ~84.4 eV shifted to lower binding energy side by 0.4 eV. The further shift of the peak position to lower binding energy side by 0.2 eV was observed at 5 Å. In the top, the spectrum of the pure Au was positioned for comparison and showed the peak at 83.8 eV, which is derived from bulk Au 4f component. As for the peak at 83.8 eV observed on the Au evaporated SrTiO$_3$ surface, the binding energy position is identical to that of the bulk Au 4f component. Therefore, the peak at 83.8 eV is

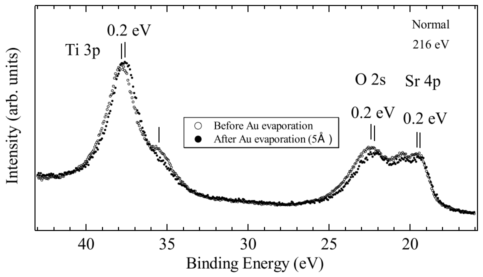

Fig. 1. Photoemission spectra of the Ti 3p, O 2s, and Sr 4p core-levels before Au evaporation and after Au evaporation of 5 Å.

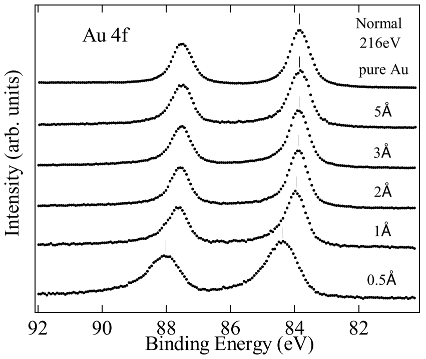

Fig. 2. Photoemission spectra of the Au 4f core-level as a function of the Au evaporation.

assigned to the bulk Au 4f component. This indicates that the deposited Au atoms at more than 1 Å are close to the pure Au. In Fig. 3, the shift of the peak in the Au 4f core-level is plotted as a function of the Au evaporation. Since the shift of peak in the Au 4f core-level is different from that in the Sr 3d core-level, the shift of the Au 4f core-level is not ascribed to only the band bending effect (~0.2 eV). Especially, at lower Au evaporation (0.5 Å), the electronic structure seems to be different from that at higher Au evaporation. The shift of the Au 4f core-level is not a charge-up effect of the substrate because no such effect was observed under the photoemission measurements of the clean $SrTiO_3(100)$ surface. In the case of the Au compounds, some Au 4f components on the higher binding energy side were observed as compared to that of the pure Au. However, the dependence of the energy shift on the Au evaporation is not explained. In the previous study of the Au-Si(100) surface, Landree et al. pointed out a final state effect arising from the formation of the Au cluster. According to Landree et al., the screening of the core-hole produced by the photoemission process is weaker when the cluster size becomes small. The position of the Au 4f core-level shifted to higher binding energy side. Therefore, there is a possibility that the shift to higher binding energy side is assigned to the final state effect caused by the formation of the Au cluster on the Au-$SrTiO_3(100)$ surface The dependence on the Au evaporation is explainable in the case of the final state effect.

Figure 4 shows the photoemission spectra of the valence band as a function of the Au evaporation. In the bottom, the spectrum of the clean $SrTiO_3(100)$ surface is positioned. In the valence band region of $SrTiO_3$, the broad feature was observed between 3-9 eV. The broad feature between 3-9 eV is predominantly derived from O 2p electrons [3]. At 0.5 Å, a peak at 6.4 eV appeared and the width of the broad feature increased. With increasing the Au evaporation at 1 Å, several peaks between 3 and 6 eV appeared. With further increasing the Au evaporation, the intensity of the peaks between 3 and 6 eV was dominant. For comparison, the spectrum of the pure Au was also positioned in the top and showed two peaks at 3.0 eV and 6.0 eV and a flat feature between E_F and 2 eV. Two peaks at 3.0 eV and 6.0 eV were predominantly derived from Au 5d electrons while the flat feature between E_F and 2 eV was predominantly derived from Au 6s electrons. Therefore, several peaks between 3 and 6 eV are predominantly derived from Au 5d electrons. In the inset of Fig. 4, the photoemission spectra near E_F were extended. In the spectrum of the clean $SrTiO_3$ surface, a state at ~1 eV below E_F was observed. The state at ~1 eV below E_F was derived from Ti 3d electrons [3], and was related to the Ti^{3+}-oxygen vacancy complexes. With increasing the Au evaporation, the intensity of the peak at ~1 eV decreased rapidly and the shift of the peak at lower binding energy side was observed. With further increasing the Au evaporation at 5 Å, the peak disappeared with high background. The decrease in intensity of the state at ~1 eV below E_F suggests that the electrons transfer from Ti^{3+} states to the deposited Au atoms. This is consistent with the results of the Ti 3p core-level. In Fig. 3, the position of the state at ~1 eV below E_F is also plotted with the Au evaporation. The shift of the state at ~1 eV below E_F is different from that in the Au 4f and Sr 3d core-levels, indicating that the shift of the state at ~1 eV below E_F is not ascribed to only the band bending effect. The state at ~1 eV below E_F arising from the Ti 3d electrons is positioned in the same energy to the Au 6s electrons of the deposited Au. In addition, the electrons transfer from Ti^{3+} states to the deposited Au was observed in this study. These results suggest that the Au 6s electrons of the deposited Au are hybridized to the Ti 3d electrons of the substrate.

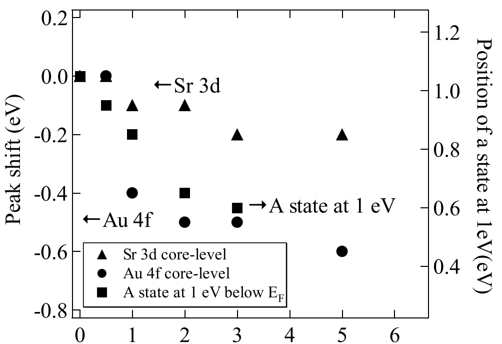

Fig. 3. In the left axis, the shifts of the peak in the Au 4f and Sr 3d core-levels were plotted as a function of the Au evaporation. The position of the state at 1 eV below E_F is also plotted in the right axis.

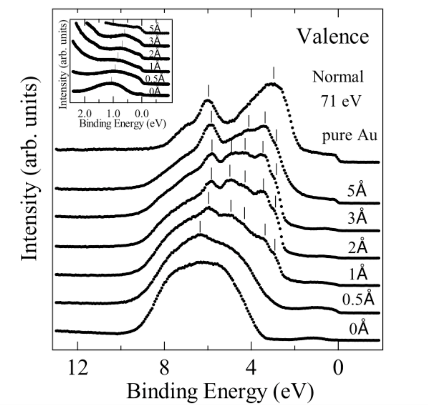

Fig. 4. Photoemission spectra of the valence band as a function of the Au evaporation.

References

[1] M. Haruta, N. Yamada, T. Kobayashi, S. Iijima, J. Catal. **115** (1989) 301.
[2] M. Haruta, Cattech **6** (2002) 102.
[3] Y. Aiura, Y. Nishihara, Y. Haruyama, T. Komeda, S. Kodaira, Y. Sakisaka, T. Maruyama, and H. Kato, in Advances in Superconductivity VI, edited by T. Fujita, and Y. Shiohara ,Springer, Tokyo, (1994) 983.

Effect of Al content on structure of native oxide films on Zn-Al Alloys formed in atmosphere

Katsuhiro Nishihara[1], Tatsuo Nagata[1], Yasuhiro Masaki[1], Masamitsu Matsumoto[1],
Takeo Kudo[1, 2], Hitoshi Uchida[2],
Yuichi Haruyama[3], Kazuhiro Kanda[3], Shinji Matsui[3], Masahito Niibe[3], Toru Mitamura[3],
1 Corporate Res. and Development Lab., Sumitomo Metal Industries LTD.
1-8, Fuso-cho, Amagasaki 660-0891, Japan
2 Graduate School of Engineering, University of Hyogo
2167 Shosha, Himeji 671-2280, Japan
3 Lab. of Advance Sci. and Tech. for Industry, University of Hyogo
3-1-2 Koto, Kamigori, Ako, Hyogo 678-1205

Abstract

Structures of thin native oxide films on Zn-Al alloys, pure Zn and Al, which formed in atmosphere, were investigated by means of photoemission spectroscopy using synchrotron radiation (SR-PES) and Al-Kα radiation (XPS).

As a result, it is found that the surface compound of thin native oxide film on Zn-Al alloys changes from zinc oxide to aluminum oxide with increasing Al content, and that the depth profile of the structure depends on Al content. Additionally, the ratio of Al content in native oxide film is more than that in Zn-Al alloy.

Introduction

Zn coating is one of useful methods for protecting steel sheets against corrosion. Recently, several Zn-Al alloy coatings, which have better corrosion resistance than zinc coating, have been invented, and the hot-dip Zn-Al alloy coated steel sheets, where Al is added to the Zn coating in the weight ratio of 5%, 55% and so on, are produced commercially [1].

In the previous study, the effect of Al content on the corrosion resistance of Zn-Al alloy coated steel sheets has been reported by many researchers [2-5]. The thin and amorphous corrosion product films, which are formed on coating in the early stages, can be confirmed directly by means of SR-PES [6]. In this study, the native oxide films on Zn-Al Alloys were investigated by means of SR-PES (168eV and 252eV) and Al-Kα radiation (1487eV).

Experiments and Results

The materials employed in this study were Zn-Al alloys and pure zinc and aluminum for comparison. In Zn-Al alloys, Al was added to Zn in the weight percent of 0.1~70%.

The specimens were prepared by cutting 10 × 10 mm plate from Zn-Al alloy ingots, and then they were mechanically polished with diamond slurry. Finally, all specimens were exposed to atmosphere for a week. As a result, native oxide films were formed on polished surface of Zn-Al alloys.

SR-PES was performed at BL-7B. XPS was carried out with XPS spectrometer (VG, ESCALAB220i-XL) using monochromatized Al-Kα radiation. Photoelectrons were detected at the angle of 90° to the surface in SR-PES and at the angle of 40° and 90° in XPS.

Fig. 1 shows XPS (1487 eV) and SR-PES (168 eV, 252eV) spectra recorded on the native oxide film. In native oxide films shown in Fig. 1 (b) ~ (d), Zn_{3p} peak around 90eV and Al_{2p} peak around 75 eV were observed in XPS spectra. In the SR-PES spectra

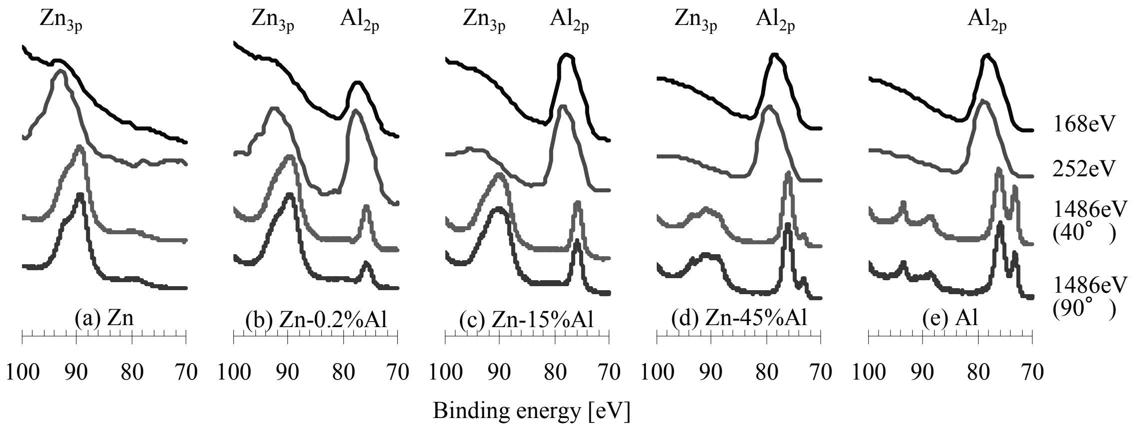

Fig.1 SR-PES (168eV, 252eV) and XPS (1486eV) spectra of thin oxide film on Zn-Al alloys
(a) Zn, (b) Zn-0.2%Al, (c) Zn-15%Al, (d) Zn-45%Al, (e) Al

(168eV) of Zn-0.2%, Zn-15%Al and Zn-45%Al, Al_{2p} peak around 76eV was clearly detected, but Zn_{3p} peak was not clearly observed. In XPS spectra of Zn-45%Al and Al, Al_{2p} peaks were assigned to Al metal.

Fig. 2 shows the peak analysis to clarify the structure of native oxide films on Zn-Al alloys. Each peak in photoemission spectra was divided into Gaussian peaks with curve fitting method. The Al content ratio was estimated from the peak intensity ratio of Al_{2p} to the sum of Al_{2p} and Zn_{3p}. Each peak intensity of Al_{2p} and Zn_{3p} were corrected by the photo-ionized cross section, which was shown in **Fig. 3** [7].

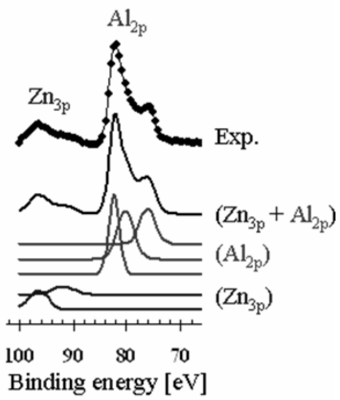

Fig. 2 Peak analysis of Al_{2p} and Zn_{3p} peaks

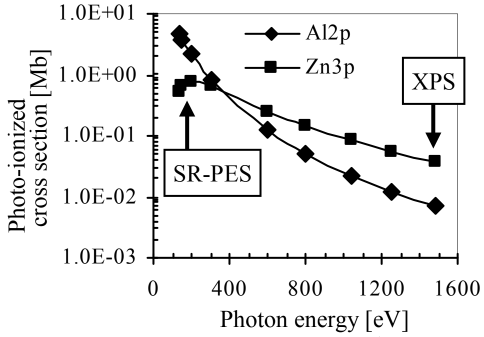

Fig. 3 Photo-ionized cross section of Al_{2p} and Zn_{3p}[7]

Fig. 4 shows the content ratio of Al to the sum of Zn and Al. XPS analysis measured a component of native oxide films on Zn-Al alloys. On the other hand, chemical analysis determined a component of Zn-Al alloys. Cleary, the ratio of Al content in native oxide film was more than that in Zn-Al alloy. Therefore, it is found that the native oxide films on Zn-Al alloys are composed of much Al content, that is, Al oxide.

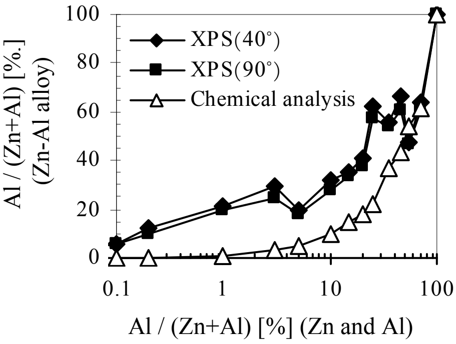

Fig.4 Al/(Zn+Al) for Zn-Al alloy and native oxide film on Zn-Al alloy

Fig. 5 shows the peak position of Zn_{3p} and Al_{2p} in XPS and SR-PES spectra. The detection depth in SR-PES and XPS were estimated 1 nm or less and 4 nm or less from the escape depth of photoelectron, respectively [8]. Accordingly, it is concluded that the depth profile of the structure in native oxide film is depended on Al content in Zn-Al alloy, and that the ratio of Al oxide in native oxide film increased with increasing Al content in Zn-Al alloy.

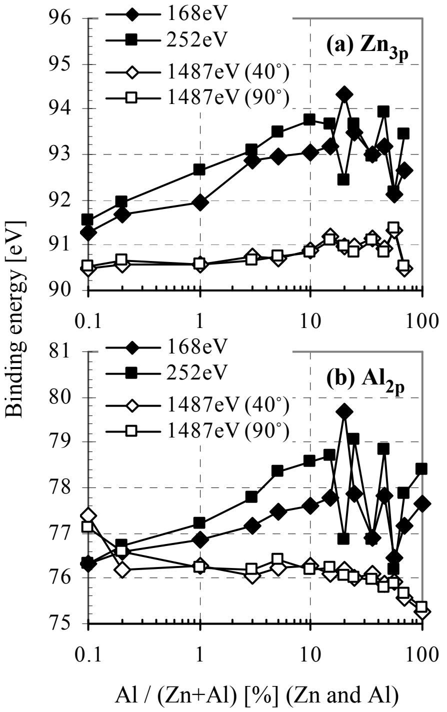

Fig. 5 Peak positions of Zn_{3p} and Al_{2p} peaks in XPS and SR-PES spectra

References

[1] M. Sagiyama, in Research Report for Fundamentals of Corrosion Protection and Evaluation Methods on Zinc and Zinc alloy Coated Steels, p.1, ISIJ, Tokyo (2005).
[2] Y. Hoboh, J. Surf. Finish. Soc. Jpn., 42, 160 (1991).
[3] D. J. Blickwede, Tetsu-to-Hagané, 66, 821 (1980).
[4] Y. Uchiyama, M. Hasaka and K. Koga, Trans. Jpn. Inst. Met., 27, 968 (1986).
[5] J. Oka, H. Asano, M. Takasugi and K. Yamamoto, Tetsu-to-Hagané, 68, A57 (1980).
[6] K. Nishihara, M. Kimoto, T. Kudo, H. Uchida, Y. Haruyama, K. Kanda and S. Matsui, in Proc. ISIJ Asia Steel/2006, p. 840, ISIJ, (2006).
[7] J. J. YEH and I. Lindau, Atomic Data and Nucl. Data Table, 32, 7-8 (1985).
[8] C. R. Brundle, J. Vac. Sci. Technol., 11, 212 (1974).

Surface Reduction in Silica Waveguide Films Irradiated by Synchrotron Radiation

K. Moriwaki, Graduate School of Eng./ Kobe Univ., K.Kanda, LASTI/Univ. Hyogo.
S.Matsui, LASTI/Univ. Hyogo, and K.Watanabe, Photonics Labs/NTT

Abstract

Synchrotron radiation without a spectrometer by the NewSUBARU is used to change the refractive index in silica-based films for optical waveguide devices. Irradiated samples are shown to have a thin reduction layer on the surface as well as a deep refractive-index-change layer. This two-layer model after the SR irradiation is confirmed by both optical absorption and reflection measurements. The thickness of the surface reduction layer is determined to be less than 45 nm by etching the sample surface. Although the refractive index change is decreased drastically after removing the surface reduction layer by etching, it still remains high (on the order of 10^{-2}) enough to apply the samples to various optical devices.

Introduction

We use synchrotron radiation (SR) for photo-induced refractive-index modifications in silica-based glasses for optical waveguide devices. Our objectives are to induce large refractive-index changes more effectively using SR without a spectrometer, and to investigate their origins depending on wavelengths in the SR spectra. Our previous results[1)] showed that a high refractive index change by SR irradiation was obtained but also a thin reduction layer was found on the sample surface measured by XPS (X-ray photoelectron spectroscopy). In our present experiments, the two layer model including the surface reduction layer after SR irradiation is characterized by optical absorption and reflection measurements or others to determine their parameters such as a thickness and a refractive-index distribution.

Experiments and Results

Experimental conditions are almost the same as in the previous experiments[1)]. SR (from the NewSUBARU BL6) was irradiated on samples directly without a spectrometer. SR with an undulator (from the NewSUBARU BL-7A) was also used to investigate wavelength effects. The electron energy of the SR was 1GeV (a wavelength range of more than about 1nm without a spectrometer). GeO_2 doped SiO_2 or pure SiO_2 glass films on Si substrates were used in our experiments. Pure silica substrate without a film was also used for an optical absorption measurement. After the SR irradiation, refractive indices for the samples were determined by an optical reflection measurement for a film on a Si substrate. XPS measurements were also used to characterize surface reduction states and their depth distributions using a dry etching method.

We have measured optical absorption spectra for samples of GeO_2 doped SiO_2 films on silica substrates and silica substrates without films as shown in Fig.1. Dotted lines in Fig.1 indicate defects of both Si E' center (215 nm)[2)] and oxygen deficiency (245 nm). For silica glass in Fig.1, oxygen deficiency defects at 245 nm are shown to be bleached and Si E' centers peak at 215 nm is generated after SR irradiation. After etching the sample surface to a depth of 15nm, the absorbance decreases drastically, this indicates removal of the surface reduction layer. As the etched depth becomes deeper than the 15 nm,

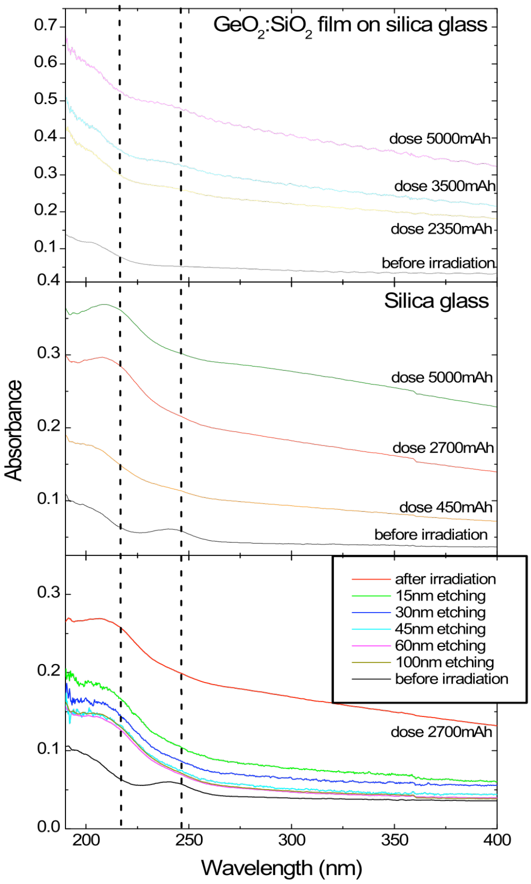

Fig.1 Optical absorbance for SR irradiated samples of GeO_2 doped SiO_2 film on silica substrate and silica substrates without films. Optical absorbance is also shown at the bottom for a sample of SR irradiated silica glass after some etching processes.

the absorbance is still decreased but is almost saturated at etched depths of deeper than 45 nm. The saturated absorbance after the etching is higher than an initial one before the SR irradiation, especially around a wavelength of 215 nm. It is important that almost only the Si E' center peak at 215 nm remains after etching the surface to a depth of 100nm. Figure 1 shows that the Si E' center defects may be the cause of the high refractive-index change without the surface reduction layer in the SiO_2 glass after the SR irradiation.

In addition, we measured optical reflection spectra from the SR-irradiated films on Si substrates. Measured spectra were analyzed to determine the refractive indices and thicknesses by a simulation including interference between the film surface and the interface to the substrate. The obtained values are shown in Fig.2 for samples before irradiation, after irradiation and after etching the irradiated one, respectively. The two-layer model was successfully used to determine the refractive indices and thicknesses in a simulation for the optical reflection spectra. The simulated thickness of the reduction layer was almost the same as was obtained in the previous XPS measurement[1)]. Simulated refractive-indices are shown in Fig.3 for samples of before, after SR irradiation and after etching the irradiated one. The refractive indices in Fig.3 were obtained by fitting the measured optical reflection spectra to simulated ones. Figure 3 shows that the refractive index becomes high by the SR irradiation because of the surface reduction layer, but it still remains high for a sample after removing the reduction layer by etching. This refractive index on the order of 10^{-2} without the surface reduction layer is high enough to apply it to optical devices. SR irradiation with an undulator and the following analysis by XPS etc. is now underway to investigate wavelength effects by the SR irradiation.

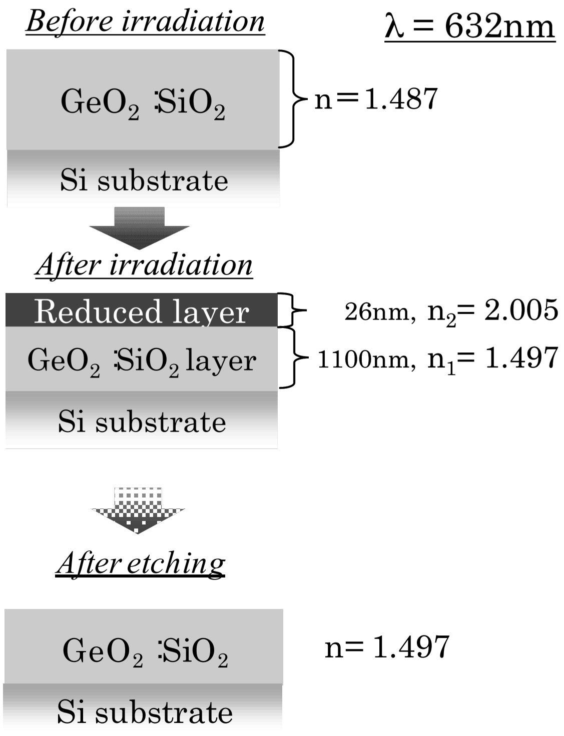

Fig.2 Parameters characterized by optical reflection measurements and their simulations for samples before, after the SR irradiation and after etching the irradiated sample, respectively.

Conclusions

For a sample irradiated by SR (BL-6) without a spectrometer, the refractive-index changes were analyzed successfully by a two-layer model including a very high refractive-index layer by a reduction on the surface and a high refractive-index layer without the reduction. A thickness of the reduction layer was determined to be less than 45nm by optical absorption measurements. Large refractive index changes (10^{-2}) were remained in a SiO_2 film by the SR irradiation after removing the reduction layer. Si E' center defects appeared in the film after the SR irradiation, and their distribution was uniform in the depth direction. Si E' centers may be the cause of the high refractive-index change for a sample without the reduction layer.

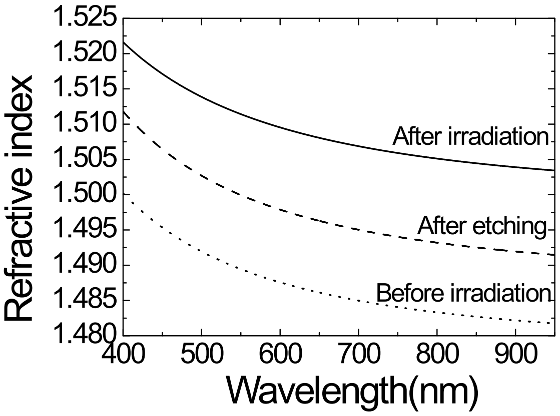

Fig.3 Refractive-index change for samples before, after irradiation and after etching determined by a simulation using the measured optical reflection data.

References

[1] K.Moriwaki *et al.*, LASTI Annual Rep ort vol. 9 (2007).
[2] H.Hosono and Y. Abe, Phys. Rev. B46, 11445 (1992).

Inhibition of Carbon Deposition on the Multilayer Mirror Surface by Introducing Water Vapor

Masahito Niibe and Keigo Koida
LASTI, University of Hyogo

Abstract

In the EUV lithography tool, carbon thin film deposition on the surface of projection optics by EUV irradiation degrades the reflectivity of the mirrors. An experiment was carried out to investigate carbon deposition and its mitigation on the surface of Mo/Si multilayer mirrors by EUV irradiation with the introduction of water vapor. In the experiment of carbon deposition by EUV irradiation in the coexistence of n-decane and water vapor, it was observed that carbon film deposition was mitigated by controlling the water vapor pressure. However, the mitigation effect on carbon deposition was not uniform for the EUV intensity, and a large non-linear dependency on the irradiation flux was observed.

Introduction

Contamination on the optical surface of an extreme ultraviolet lithography (EUVL) tool is one of the critical issues to be solved to commercialize the system. To develop a contamination-protection technology for the surface of projection optics for an EUVL system, various examinations were carried out on Mo/Si multilayer mirrors. There are two kinds of contamination by EUV irradiation on projection optics. They are carbon deposition and oxidation of the Si layer atop of a Mo/Si multilayer. Both types of contamination decrease the reflectivity of multilayers and cause a resultant decrease in the throughput of the exposure tools. In our previous work [1], we have found that carbon film deposition and surface oxidation, which have been thought to occur independently of surface degradation, are reactions that occur competitively and antagonistically. Therefore, it is important to balance the amount of hydrocarbons that are the source of carbon film deposition and that of oxidation gases, such as water vapor. To extend this idea further and understand the mechanism of the contamination, an experiment of carbon deposition mitigation by EUV irradiation in the coexistence of n-decane and water vapor was carried out.

Experiments

The details of the EUV contamination evaluation system that we used have been reported elsewhere [2]. The sample was put in a holder fixed on x-z axial automatic stages. The reflectivity of the sample was measured by two photo-diode detectors (IRD, SXUV-100), one of which measured the direct beam intensity when the sample was removed from the irradiation beam and another which measured the reflection beam intensity. EUV irradiation and the measurement of the relative reflectivity change were carried out *in situ*. By regulating the beam size using a 100 μm diameter pinhole in the reflectivity measurement, the reflectivities of 11 different intensity points were measured in one series of irradiation and measurement. The reflectivity map was also obtained by using the pinhole. The sample holder was electrically insulated from the chamber, and the electron emission current by EUV irradiation was measured as the sample current. Using the sample current with a monochromated photon energy scan, *in situ* analysis and elemental mapping of the irradiated surface were carried out as soft X-ray absorption spectrometry (XAS) with the total electron yield mode [3].

The sample used for the EUV irradiation was a Mo/Si multilayer mirror with a period of about 7 nm and number of layer pairs of 50 and top of the surface was coated by about 2 nm-thick Ru metal. The ultimate pressure of the measurement chamber was less than 2×10^{-7} Pa, and the main component of residual gas was water (M=18). Two lines of a gas introduction system were equipped at the measurement chamber, and the pressure of gas was controlled by a needle valve. In this experiment, one line was used for introducing n-decane gas, and another line was used for the introduction of water vapor. The experimental condition of gas introduction for the experiments is shown in Table 1.

Table I Experimental conditions.

n-decane pressure	(Pa)	3.0×10^{-5}
Water Vapor pressure	(Pa)	0, 1.3×10^{-6} 1.3×10^{-5}, 5.0×10^{-5}, 3.0×10^{-4}

Results

Figure 1 shows the sequential reflectivity change at the irradiation center of multilayer mirrors under an atmosphere of a fixed n-decane pressure of 3.0×10^{-6} Pa as well as under a variable water vapor pressure from 0 to 1.3×10^{-4} Pa . At a water vapor pressure below 1.3×10^{-5} Pa, the relative reflectivity increased by about 1% in the early stage of EUV irradiation. The reflectivity then decreased gradually, and the value became 97% at the EUV dose of 1200 J/mm^2. On the other hand, at a water pressure greater than 5.0×10^{-5} Pa, the rate of the reduction of reflectivity was small, and the relative reflectivity was 98.5% at the EUV dose of 1200 J/mm^2.

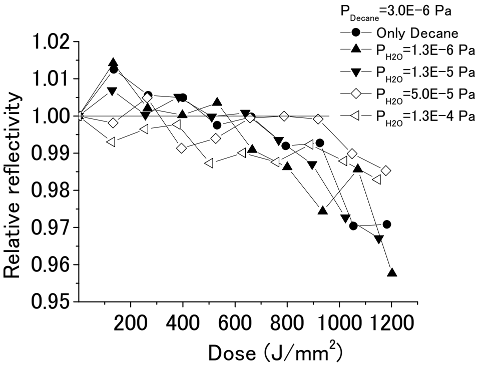

Fig. 1 Dose dependence of the relative reflectivity change of Ru-capped Mo/Si multilayer mirrors by EUV irradiation in the presence of n-decane gas and water vapor atmosphere.

A reflectivity map of the irradiated area for the sample of irradiation condition at an n-decane pressure of 3.0×10^{-6} Pa and a water vapor pressure of 5.0×10^{-5} Pa is shown in Fig. 2. As shown in Fig. 2, the shape of the reflectivity drop was similar to that of a doughnut, which means that the reflectivity drop at the irradiation center was not remarkable and the value was almost equal to that at the non-irradiated area. However, a large reflectivity drop occurred at the periphery of irradiation center, where the EUV intensity was rather small. The doughnut shapes of the reflectivity distribution were observed for all samples at water vapor pressures from 1.3×10^{-5} Pa to 1.3×10^{-4} Pa.

Figure 3 shows the distributions of the XAS intensity of (a): C-K and (b): O-K absorption edges of the sample, which are nearly proportional to the surface atomic density of carbon and oxygen elements, as reported earlier [3]. The distribution of the carbon density was trapezoidal for the sample at a water vapor pressure of 0 to 1.3×10^{-6} Pa. This trapezoidal distribution was similar to the carbon thickness distribution for the samples of only lower decane gas pressures. On the other hand, for the sample of a water vapor pressure higher than 1.3×10^{-5} Pa, the carbon concentration at the irradiation center decreased with increasing the water vapor pressure. The shape of the distribution was similar to that of the letter "M" (or two-dimensionally, doughnut-shaped). The atomic concentration of oxygen at the irradiated area decreased from the non-irradiated area for the samples at water vapor pressures below 5.0×10^{-5} Pa. However, the concentration of oxygen became high at the irradiation center for the samples at a water vapor pressure of 1.3×10^{-4} Pa. The problem of the non-linear behavior to the EUV intensity in the atmosphere into which water vapor was introduced still needs to be resolved.

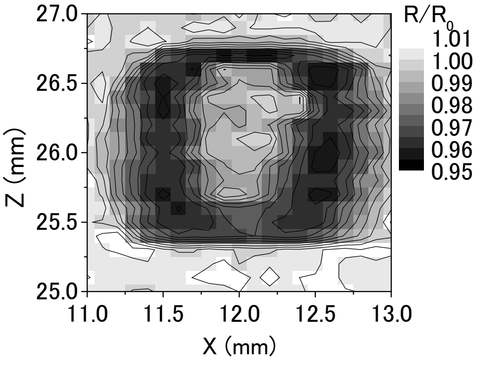

Fig. 2 Reflectivity map of the EUV-irradiated area after irradiation in the presence of decane gas at P_{decane}= 3.6 E-6 Pa and P_{H2O}=5.0 E-5 Pa at the dose of 1200 J/mm2.

A part of this work was performed by using the resources of NEDO.

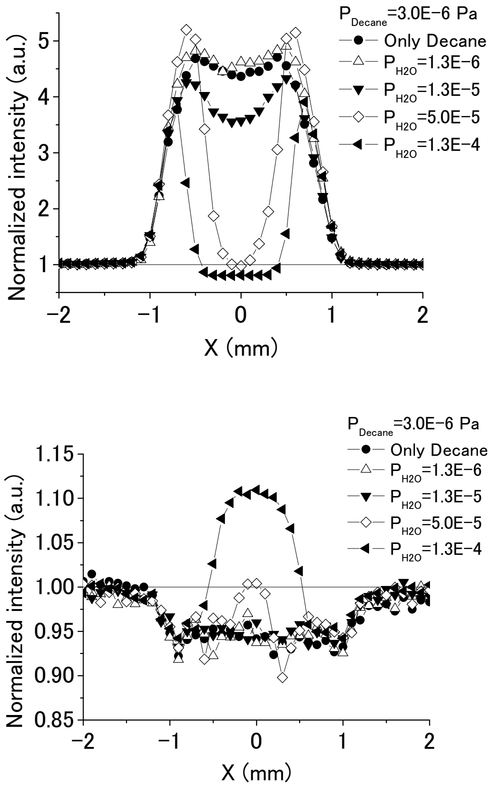

Fig. 3 Normalized photo-absorption intensity distribution of (a): C-K and (b): O-K edges at the EUV-irradiated area after the carbon-deposition mitigation experiment by water vapor.

References

[1] M. Niibe *et al.*, J. Vac. Sci. Technol. **B26**, 2230 (2008).

[2] M. Niibe *et al.*, Jpn. J. Appl. Phys. **45**, 5373-5377 (2007).

[3] M. Niibe *et al.*, J. Vac. Sci. Technol., **B25**, 2118 (2007).

Analysis of carbon deposition on multilayer mirrors by using two different beamlines

Takahiro Nakayama[a], Hiroyoshi Kubo[a], Akira Miyake[a], Hiromitsu Takase[a], Shigeru Terashima[a], Yasuaki Fukuda[a], Katsuhiko Murakami[b], Shintaro Kawata[b], Takashi Aoki[b], Shuichi Matsunari[b], Yukinobu Kakutani[b], Keigo Koida[b], Masahito Niibe[c]
[a]Canon, 23-10, Kiyohara-Kogyodanchi, Utsunomiya-shi, Tochigi-ken, 321-3298, Japan
[b]Nikon, 1-10-1, Asamizodai, Sagamihara-shi, Kanagawa-ken, 228-0828, Japan
[c]Laboratory of Advanced Science and Technology for Industry (LASTI), Univ. of Hyogo,
3-1-2, Kouto, Kamigori-cho, Ako, Hyogo 678-1205, Japan

Abstract

It is very important to mitigate oxidation of multilayer mirrors (MLMs) and carbon deposition onto MLMs to extend the lifetime of EUV exposure tool. In order to estimate the lifetime, we have to figure out scaling law. Previous results at EUVA have shown that carbon deposition rate on MLMs is not proportional to every hydrocarbon partial pressure and every EUV intensity[3-4]. In this study we focused on carbon deposition on Si-capped multilayer mirror. We made experiments of EUV irradiation to the MLMs using two different apparatuses. One is connected to a beamline (SBL-2) of synchrotron radiation facility Super-ALIS in the NTT Atsugi research and development center, and the other is connected to a beamline (BL9) of synchrotron radiation facility New SUBARU in the University of Hyogo. As the result of experiments, we found that different carbon deposition rate occurred on the different beamlines, although they have the same average EUV intensity. We present differences of carbon deposition rate on MLMs between two different beamlines and estimation of carbon deposition rate on EUV tool analyzing dependences of carbon deposition rate on characteristics of EUV source.

Introduction

HVM (High Volume Machine) of EUV Scanner is needed to operate for several years without high maintenance cost. In order to estimate a lifetime for HVM, we have to figure out scaling law. We focus on the scaling law of contaminations on multilayer mirrors (MLMs). Carbon deposition on MLMs causes a damage of optical performances. We have to elucidate a photochemical reaction of EUV irradiation to the MLMs and estimate carbon deposition rate for HVM. We found that carbon deposition rate is not proportional to average EUV intensity and hydrocarbon partial pressure[3-4]. But we do not know dependences of carbon deposition rate on characteristics of EUV source. So we need to make a comparison between different EUV sources to understand the reaction quantitatively.

Experiments and Results

We made experiments using two different beamlines. One is a beamline (SBL-2) of synchrotron radiation facility Super-ALIS in the NTT Atsugi research and development center. The other is a beamline (BL9) that is a long undulator in NewSUBARU synchrotron radiation facility in the University of Hyogo. Table 1 shows characteristics of both the EUV beamlines. Experimental data of carbon deposition rate at SBL-2 and reflectivity change at BL9 have been reported in detail in previous papers[1-4]. We set an irradiation time at 2 to 9 hours to acquire samples with suitable thickness of deposited carbon to analyze. Therefore the irradiation time is different every sample. We injected decane ($C_{10}H_{22}$) that was selected because its vapor pressure is high enough to control its partial pressure easily in the irradiation chamber. Table 2 shows experimental conditions of injected gases. We consider that the reason why water partial pressure is larger than background pressure shown in Table 1 is to inject water with decane gas. We used X-ray photoelectron spectroscopy (XPS) and obtained carbon deposition quantity from photoelectron intensity of C(1s). We can detect Ru(3d3/2) and C(1s) with XPS, but both binding energy are near values. So we cannot discriminate between Ru(3d3/2) and C(1s) peaks. Therefore in this experiment, we used multilayer mirrors of $[\mathrm{Si}(4.2\ \mathrm{nm})/\mathrm{Mo}(2.8\ \mathrm{nm})]^{50}$ on Si-wafer, i.e. Si-capped MLMs. We converted photoelectron intensity of C(1s) into a carbon film thickness. Furthermore, we calculated carbon deposition rate by dividing the carbon film thickness by the total irradiation time. Average EUV intensity was calculated by dividing total EUV dose by total irradiation time. We show dependence of carbon deposition rate on average EUV intensity in Fig. 1. Injected decane pressures of Fig. 1(a) and Fig. 1(b) are $\sim 1\times10^{-6}$ Pa and $\sim 2\times10^{-7}$ Pa, respectively. Both results show that the carbon deposition rate in BL9 is higher than that in SBL-2. Both carbon deposition rates are saturating following average EUV intensity increasing. Comparing with both saturated carbon deposition rate, carbon deposition rate in BL9 is 3 to 5 times higher than that in SBL-2. The minimum average EUV intensity to saturate carbon deposition rate in BL9 is over 4 times higher than that in SBL-2. The results show that a carbon deposition rate depends not only on average EUV intensity, but also on other characteristics of EUV source that can be source frequency and pulse width of EUV light.

Several models of the photochemical reaction under EUV irradiation have been reported[5-9]. In this study we used NIST (National Institute of Standards and Technology) simple thick-C-growth model[10] shown in Fig. 2 and we have fitted our experimental data of carbon deposition rate using the model. Surface reaction in EUV light unirradiated is as follows:

$$\frac{dS_M(t)}{dt} = Z_P\left(1 - \frac{S_M(t)}{S_{Max}}\right) - \frac{S_M(t)}{\tau_S}$$

Photochemical reaction in EUV light irradiated is described as follows:

$$\frac{dS_M(t)}{dt} = Z_P\left(1 - \frac{S_M(t)}{S_{Max}}\right) - \frac{S_M(t)}{\tau_S} - I_{EUV}\sigma_{tot}S_M(t)$$

$S_M(t)$ is coverage of adsorbed intact molecules [molecules $*\mathrm{cm}^{-2}$]. S_{max} is site-limited max coverage (= ~1ML). Z_P is impingement rate [molecules$*\mathrm{cm}^{-2}*\mathrm{s}^{-1}$]. τ_S is surface-residence time [s]. I_{EUV} is incident EUV intensity [photons$*\mathrm{cm}^{-2}*\mathrm{s}^{-1}$]. σ_{tot} is total cross section [cm^2]. Carbon-growth rate, k [C atoms$*\mathrm{cm}^{-2}*\mathrm{s}^{-1}$], is described as follows:

$$k = \nu N_C \int_0^{t_P} I_{peak}\sigma_{tot}S_M(t)dt$$

ν is source frequency. t_p is pulse width. I_{peak} is peak intensity when square wave pulse is assumed. N_C is a number of carbon atoms in a hydrocarbon molecule. Solving and using these equations, our experimental data in SBL-2 were fitted with fitting parameters of surface-residence time and total cross section. We used three experimental conditions at SBL-2. These partial pressures of decane are $1.2\mathrm{x}10^{-6}$, $7.3\mathrm{x}10^{-7}$ and $2.3\mathrm{x}10^{-7}$ Pa. The total cross section σ_{tot} was $6\mathrm{x}10^{-9}$ cm^2. The obtained total cross section is large comparing with photo-absorption cross section ($3\mathrm{x}10^{-19}$ cm^2/atom) at EUV of "Si". ASET has reported surface-residence time of H2O on Si is two microseconds[11]. NIST has also reported surface-residence time of benzene on C/TiO2, benzene on TiO2 and methyl methacrylate on TiO2, are $1\mathrm{x}10^{-6}$~$1\mathrm{x}10^{-5}$ sec., $1\mathrm{x}10^{-4}$~$1\mathrm{x}10^{-2}$ sec. and 10~1000 sec. [12], respectively. Our residence time ($5\mathrm{x}10^{-10}$ sec.) is shorter than theirs. The parameters need to be verified and modified. And calculation result does not correspond with our experimental result in higher partial pressure $6\mathrm{x}10^{-5}$ Pa. In EUVL symposium 2008, NIST has presented that a carbon growth has logarithmic dependence over multiple decades of hydrocarbon pressure, which suggests adsorption model similar to Temkin isotherm[12]. So we can use the equation and parameters in the limited conditions between $1.2\mathrm{x}10^{-6}$ and $2.3\mathrm{x}10^{-7}$ Pa. Using above parameters and equations we calculated dependences of carbon deposition rate on average EUV intensity. The results are shown in Fig. 1 that has the same experimental conditions as the experiments. We can see that calculation results have the same behavior of the experimental result. So this indicates the possibility that source frequency and pulse width affect the carbon deposition. We estimate dependences of carbon deposition rate on several source parameters. We calculate with three different pulse width, $2.6\mathrm{x}10^{-11}$, $1\mathrm{x}10^{-8}$ and $1\mathrm{x}10^{-4}$ seconds, and also calculate with three different source frequency, $5\mathrm{x}10^{8}$, $5\mathrm{x}10^{4}$ and 150 Hz. We assume decane as an induced hydrocarbon molecule and partial pressure $1\mathrm{x}10^{-7}$ Pa. Average EUV intensity is 0.1 $\mathrm{mW/mm}^2$. The dependences of carbon deposition rate on source frequency and pulse width are shown in Fig. 3(a) and Fig. 3(b), respectively. The dotted circle indicates experimental conditions. Figure 3(a) shows that carbon deposition rate is proportional to source frequency in low source frequency. The other hand, carbon deposition rate is saturated in high source frequency. We have considered that carbon deposition rate is limited by hydrocarbon pressure in low source frequency and by number of photons in high source frequency. Figure 3(b) shows that carbon deposition rate is proportional to pulse width in short pulse width and is saturated in long pulse width. These phenomena are caused by the same reason as the dependence on source frequency.

In conclusion, we made experiments using two different beamlines and figured out the scaling law for two beamlines. The carbon deposition rate depends not only on average EUV intensity. We used NIST simple thick-C-growth model and fitted our experimental data of carbon deposition rate. Using the model and assuming parameters, we calculated dependences of carbon deposition rate on average EUV intensity. The calculation results have the same behavior of the experimental data from $2.3\mathrm{x}10^{-7}$ to $1.2\mathrm{x}10^{-6}$ Pa of decane partial pressure. As the calculation parameters are different from what we expected, the dependence of carbon deposition rate on characteristics of EUV source is not completely understood. Therefore the reaction model needs to be verified and modified. There are also a lot of other works to be figured out in the future, which is dependence of carbon deposition rate on hydrocarbon partial pressure, on gas species and on capping layer. Standing wave effect and quantitative data, total cross section and residence time in an each gas species and capping layer material, also need to be figured out. Finally, It is important to make an experiments using EUV source which has source frequency and pulse width like those for high volume machine to figure out the scaling law.

A part of this work was performed as a research and development program of Ministry of Economy Trade and Industry (METI) and New Energy and Industrial Technology Development Organization (NEDO) under the management of Extreme Ultraviolet Lithography System Development Association (EUVA).

Table 1. Characteristics of the EUV beamlines.

Beamline	Maximum EUV intensity (mW/mm^2)	Diameter of EUV irradiated area (mm)	Source frequency (MHz)	Pulse width (psec.)	Background pressure (Pa)
SBL-2	12~24	2	125	78	$<5x10^{-7}$
BL9	~200	2	500	26	$<5x10^{-7}$

Table 2. Experimental conditions.

Beamline	Decane partial pressure (Pa)	Water partial pressure (Pa)	Total pressure (Pa)	Irradiation time (hrs)
SBL-2	6.0×10^{-5}	2.1×10^{-6}	6.5×10^{-5}	4
	1.2×10^{-6}	4.6×10^{-7}	1.9×10^{-6}	5
	7.3×10^{-7}	3.6×10^{-7}	1.1×10^{-6}	5
	2.3×10^{-7}	3.0×10^{-7}	5.8×10^{-7}	8
BL9	1.2×10^{-6}	3.3×10^{-6}	5.0×10^{-6}	1.3
	2.5×10^{-7}	3.5×10^{-7}	7.0×10^{-7}	2.7

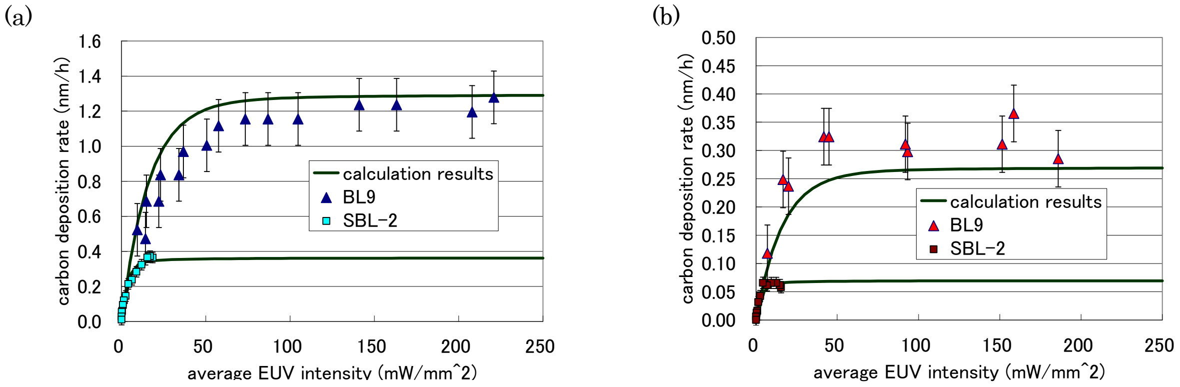

Figure 1. Dependence of carbon deposition rate on average EUV intensity
Experimental data and calculation results at both beamlines are shown in Fig. 1(a) and Fig. 1(b). Decane pressures are 1.2×10^{-6} Pa in BL9 and 1.2×10^{-6} Pa in SBL-2 in Fig. 1(a). Decane pressures are 2.5×10^{-7} Pa in BL9 and 2.3×10^{-7} Pa in SBL-2 in Fig. 1(b).

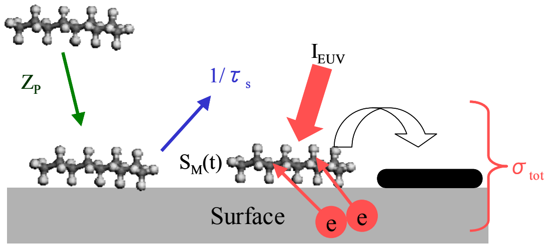

Figure 2. NIST simple thick-C-growth model.

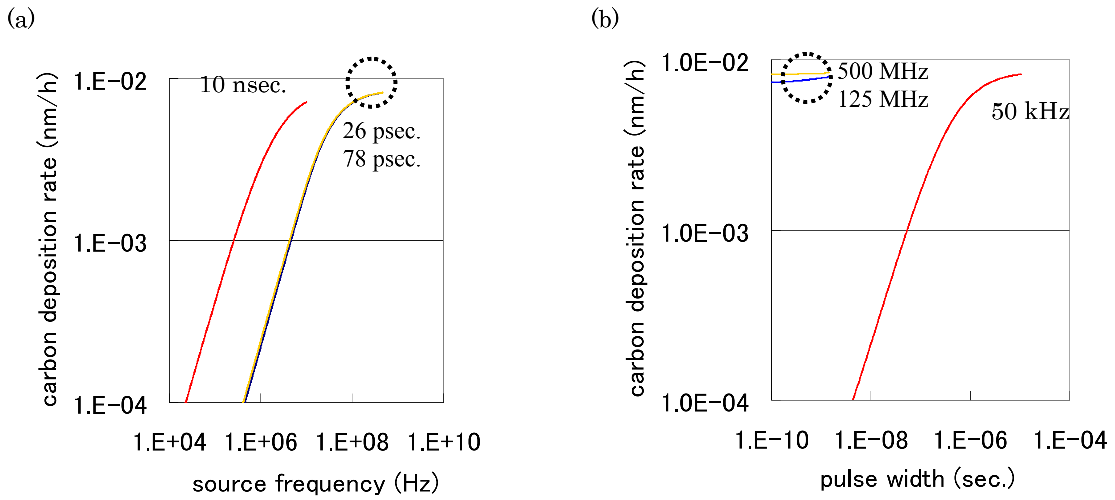

Figure 3. Dependence of carbon deposition rate on source frequency and on pulse width.
Dependence of carbon deposition rate on source frequency and on pulse width are shown in Fig. 3(a) and Fig. 3(b), respectively. Dotted circle indicates experimental conditions.

REFERENCES

[1] M. Niibe, “New contamination experimental equipment in the NewSUBARU and evaluation of Si-capped multilayer mirrors using”, Proc. of SPIE Vol. 6151, 34, 2006

[2] Y. Kakutani, “Long-term durability of a Ru capping layer for EUVL projection optics by introducing ethanol”, Proc. of SPIE Vol. 6517, 31, 2007

[3] H. Takase, “Study of Ruthenium-capped Multilayer Mirror for EUV Irradiation Durability”, Proc. of SPIE Vol. 6151, 35, 2006

[4] T. Nakayama, “Phenomenological analysis of carbon deposition rate on the multilayer mirror”, Proc. of SPIE Vol. 6921, 3B, 2008

[5] Ralph Kurt et al.,"Radiation－induced carbon contamination of optics", Proc. of SPIE 4688, 702－709, 2002

[6] Jeromy T. Hollenshead and Leonard E. Klebanoff, "Modeling carbon contamination of extreme ultraviolet (EUV) optics", Proc. of SPIE 5374, 675－685, 2005

[7] J. Hollenshead et. al., "Modeling radiation－induced carbon contamination of extreme ultraviolet optics", J. Vac.Sci. Technol. B 24(1), 64－82, 2006

[8] S. Matsunari et. al., "Carbon deposition on multi－layer mirrors by extreme ultra violet ray Irradiation", Proc. of SPIE 6517, 2X, 2007

[9] S. B. Hill et. al., "Accelerated lifetime metrology of EUV multilayer mirrors in hydrocarbon environments", Proc. of SPIE 6921,42 , 2008

[10] S. B. Hill et. al., “Limits to accelerated MLM lifetime testing: TiO2 in hydrocarbons and Ru in H2O”, IEUVI-TWG, EUVL symposium, 2007

[11] I. Nishiyama, “Model of Ru surface oxidation for the lifetime scaling of EUVL projection optics mirror”, Proc. of SPIE Vol. 6151,0G-1, 2006

[12] S. B. Hill et. al., “EUV-induced contamination of TiO_2 surfaces by anticipated tool-environment hydrocarbons”, EUVL symposium, 2008

Improvement of EUV-mirror reflectance measurement stability on Beamline 9 of NewSUBARU

Yukinobu Kakutani[a] **and Masahito Niibe**[b]
[a]Nikon, 1-10-1, Asamizodai, Sagamihara-shi, Kanagawa-ken, 228-0828, Japan
[b]Laboratory of Advanced Science and Technology for Industry (LASTI), Univ. of Hyogo, 3-1-2,
Kouto, Kamigori-cho, Ako, Hyogo 678-1205, Japan

EUV-mirror reflectance changes during EUV irradiation (13.5nm) have been measured as lifetime tests of multilayer mirrors (MLMs) on the beamline 9. To evaluate the mirror reflectance changes due to EUV irradiation, the reflectance measurement error is required to be less than +/- 0.5%.

In Beamline 9 of NewSUBARU , we can measure two beam positions near a focus point of the beam line and just in front of sample position, which were used for the beam position adjustment. We can also measure the EUV beam intensity through a pinhole in a 100um diameter, which has been used in a reflectance measurement.

Changes in beam intensity through a pinhole set just in front of sample position and beam positions along horizontal and vertical axes at near a focus is shown in Fig. 1.

Comparing the beam position near the focus and the beam intensity, it was found that a part of experimental errors were originated from both horizontal and vertical drift of beam positions during the reflectance measurements of 5 or 6 min. It was also found that jumps of beam position, which may be connected to COD correction. In addition to the beam drifts, the noise of the EUV detector output in the reflectance measurement system (the ammeter read error) affects to experimental error. Each experimental error was estimated to be +/-0.2% for the horizontal drift, +/- 0.25% for the vertical drift, +/- 0.35% for the beam jump, and +/- 0.2% for the read error of the ammeter. The total experimental error, which was convoluted from each error, was about +/-0.5%. The experimental error width was not small for mirror reflectance measurements. The system was improved as follows:

1. The feedback system of the beam position was improved by changing amplifiers of the position measurement to be faster, which makes the beam drift small.
2. The read error of the ammeter was improved to +/-0.1% by changing the integration time which octuple from 166 ms to 1.33 s.
3. The measurement data at the beam jump are omitted using a revised measurement program

code easily. Using the revised code a reflectance measurement is able to be done within 1 min from 5-6 min.

Each experimental error improves to +/-0.15% for the vertical drift, +/- 0.1% for the read error of the ammeter, and the errors for the horizontal drift and for the beam jump can be negligible. The total experimental error +/-0.2% was achieved.

This error can be small enough to measure the reflectance change in recent evaluated samples.

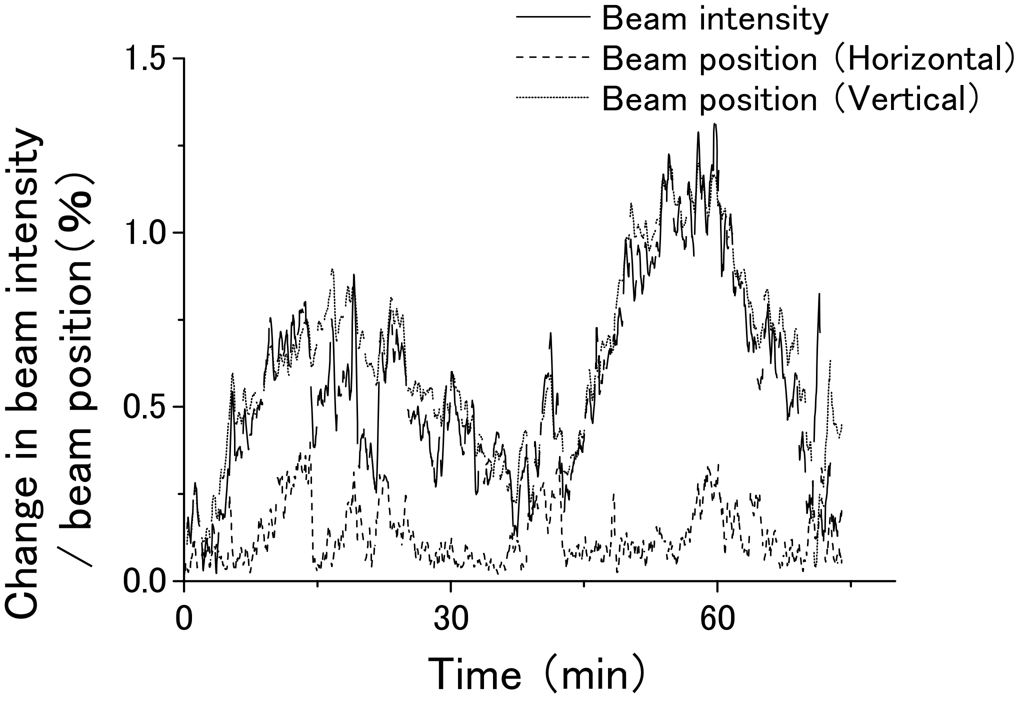

Fig. 1. Changes in beam intensity through a pinhole set just in front of sample position and beam positions along horizontal and vertical axes at near a focus in Beamline 9.

Electronic State Analysis of Minor Elements in Ultra-fine Grained Metallic Materials

M. Terasawa, T. Mitamura, M. Niibe, LASTI, University of Hyogo
T. Yamasaki, Dept. of Materials and Chemistry, Graduate School of Engineering, University of Hyogo
H. Kurishita, Institute for Materials Research (IMR), Tohoku University
M. Kawai, Institute of Material Structure Science, High Energy Accelerator Research Organization (KEK)

Abstract

Ultra fine grained (UFG) materials of SUS316L and W were fabricated by mechanical alloying (MA) and hot isostatic pressing (HIP) treatments. It was found that addition of about 1 % TiC powder was effective to reduce the grain size down to 100nm, and the materials exhibited superior irradiation resistance and mechanical properties. The electronic states of the TiC in the UFG materials were analyzed by XANES spectroscopy at NewSUBARU BL9.

Introduction

Life extension of nuclear power plants is one of the major recent targets to be developed for economical electric-power generation. The extension means prolonged use of nuclear fuels and core reactor materials in nuclear reactors. On the other hand, in the J-PARC program, which is a large accelerator development project in Japan to promote use of secondary particles, such as neutron, pi- and myu-particles, neutrino and so on, produced by high energy proton beam bombardment. For the neutron source in the J-PARC facility, liquid mercury target enveloped with metallic container is planned to be adopted.

The metallic materials are likely to deteriorate in the nuclear water reactors due to radiation hardening, embrittlement, and/or stress corrosion cracking. The environment for the materials of the neutron source in J-PARC is much severe. It is strongly expected that the materials are developed so as to show tough resistance for such phenomena.

We are developing ultra-fine grained materials of austenitic stainless steel (316L) and W with addition of small amount of TiC powder. In this work, electronic state analysis of TiC in the W-TiC materials was investigated by XANES spectroscopy in order to elucidate the effect of TiC addition.

Experiments and Results

Fabrication of ultra-fine grained materials

Ultra-fine grained materials of austenitic stainless steel (SUS316L) and W were fabricated by mechanical-alloying (MA) and hot isostatic pressing (HIP) treatments. Powder of SUS316L (an average particle size: 44 – 105 μm) or pure W (4.0 μm), combined with TiC (0.57 and 40 μm, respectively), were used as the starting materials.

The SUS316L-1.0wt.% TiC materials with the average grain sizes of 100 nm were obtained by 80 % cold roll and annealing at the temperature of 800℃, after MA and HIP (800℃) treatment. The fabricated materials have exhibited good resistance to neutron irradiation examined in JMTR up to 1.14 x 10^{24} n/m^2 (E_n>0.1 MeV). The hardness increase of the materials after the irradiation is only 6.0 %, though much higher increase (73 %) is shown in the simultaneous irradiation of the standard SUS316L specimens. The lower void swelling of the ultra-fine grained materials than standard 316L is also found in 1 MeV electron irradiation, as shown in Fig. 1.[1,2]

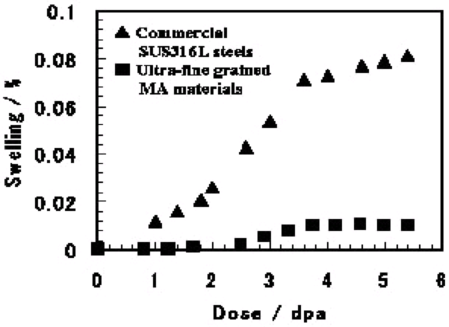

Fig.1 Void swelling of the UFG SUS316L-TiC irradiated by 1 MeV electrons at 400℃

The ultra-fine grained (UFG) W-1.1wt.% TiC materials are obtained with the grain size of 50 – 100 nm, and have exhibited superior resistance to the irradiation with neutrons and helium-ions.[3,4]

Electronic state analysis of TiC in UFG materials

In the fabrication of the UFG materials, small amount (about 1 wt.%) of TiC addition is found extremely effective to control the grain size in both materials of SUS316L and pure W, as described above. Although it is suggested that TiC nano particles act so as to pin the grain boundary during the fabrication process, what kind of interaction of TiC with matrix materials is concerned, and by what mechanism the pinning is governed are not clear.

We tried to measure the electronic states of Ti in the W-1.1wt.% TiC consolidates, as a preliminary step to elucidate the behavior of Ti or TiC in the fabrication process. XANES spectroscopy was performed at the end-station of the long undulator beamline BL9 in the NewSUBARU SR facility using a high resolution monochromator [5]. The data were collected by a total electron yield (TEY) mode in which the sample current was measured when the photoelectron emitted by soft x-ray absorption. The values were normalized with a simultaneously recorded photoemission signal from a gold mesh, which indicate the soft x-ray intensity incident into the sample. The measurement system is shown in Fig. 2 schematically. At the present time, XANES spectra of Ti-L and C-K absorption edge of TiC in the W-1.1wt.% TiC consolidates were measured.

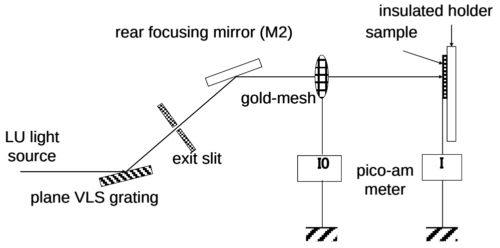

Fig.2. Schematic diagram of XANES measurement in total electron yield mode

Fig. 3 shows Ti-$L_{2,3}$ absorption spectra for pure Ti (99.99 %) metal and TiC powders measured for reference before the XANES study for the fabricated W-TiC materials. A peak of Ti-L_2 ($2p_{1/2}$) and L_3 ($2p_{3/2}$) was observed at 465.9 eV and 461.4 eV, respectively, in the Ti specimen. On the other hand, each of L_2 and L_3 spectral line exhibits twin peak structure with an additional line with a separation of about 1.5 eV for the TiC powder specimen. The spectral variation is reflected by electronic structure due to different chemical state.

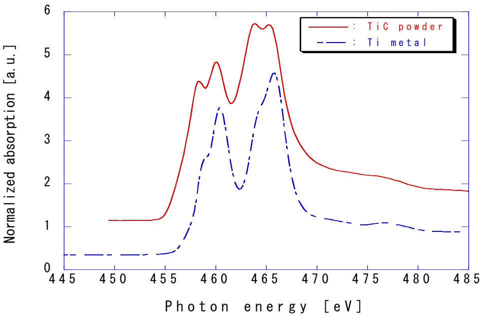

Fig.3. Ti-$L_{2,3}$ edge XANES spectra of Ti and TiC

Fig.4 shows XANES spectra of Ti-$L_{2,3}$ for the UFG W-1.1wt.% TiC specimens. Three kinds of materials, which fabricated by different environment mechanical alloying in order to investigate the plastic behavior, are examined. That is, #A; treated at 1650℃ in H_2 environment, #B; treated at 1650/ 1850℃ in H_2 environment, #G; treated at 1650℃ in argon environment. The materials treated in H_2 are found to exhibit a large strain rate sensitivity of flow stress, m, of 0.5 – 0.6, which is a feature of superplastic materials, while the ones treated in argon exhibit a smaller m value of approximately 0.2.[6]

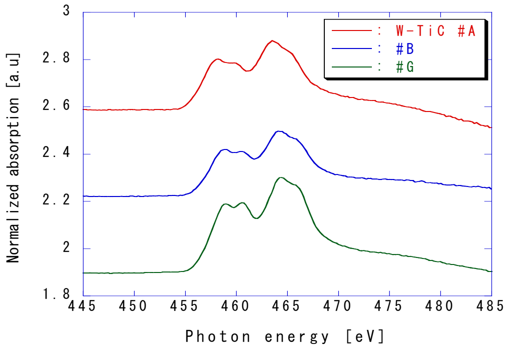

Fig.4. Ti-$L_{2,3}$ edge XANES spectra of UFG W-TiC materials

The XANES spectra observed show characteristic twin peak structures for both L_2 and L_3, which are in general agreement with the spectra shown in TiC powders. Somewhat deformed profiles of the twin peaks in the W-TiC materials may be due to the existence of partly decomposed Ti and/or other chemicals such as oxides or nitrides. Although we tried to measure Ti-$L_{2,3}$ electrons for the W-TiC specimens by the XPS previously, the electrons was hardly observable, the present XANES studies were successful as described above.

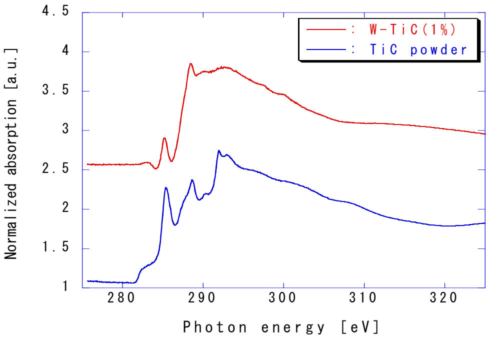

Fig.5. C-K edge XANES spectra of TiC and UFG W-TiC materials

The XANES spectra of C-K edges for W-1.1wt.% TiC and powder TiC are compared in Fig. 5. The reduction of π^* peak at 285 eV and enhancement of the peak at 288 eV is prominent for the W-1.1wt.% TiC specimens. This change may give an important electronic state transition information during the MA and HIP process in the UFG material fabrication.

References

[1] Y. Z. Cheng et al, Material Science Forum, **426-432**, pp.1065-1070 (2003).

[2] H. Matsuoka et al, Proc. ICAPP'05, Seoul, Korea (2005) paper 5687.

[3] H. Kurishita et al, Phys. Scr. T128 (2007) pp.76-80.

[4] H. Kurishita et al, IWSMT-8 (2006).

[5] M. Niibe et al., AIP Conf. Proc. 705, 576 (2003).

[6] H. Kurishita et al, Mater. Sci. Eng. A (in press).

Soft X-ray Absorption Spectra of TiO_2 Thin Films Prepared by Magnetron Sputtering Technique

Masahito Niibe[1], Masanori Kayahara[2] and Shozo Inoue[2]
LASTI[1] and Graduate School of Eng. [2], University of Hyogo

Abstract

Soft X-ray Absorption Spectra (XAS) of Ti-$L_{2,3}$ and O-K edges were measured for the samples of TiO_2 thin films prepared by magnetron sputtering technique. The samples were deposited by reactive RF-magnetron sputtering system at incident angles of sputtered particles to substrate normal of 0° (normal) and 80° (GLAD). The samples were also annealed at 300°C. The Ti-$L_{2,3}$ edge spectra indicates that the prepared samples contain almost the same amount of rutile and anatase crystalline structures. It was also found from the O-K edge spectra that the absorption intensity of the broad peak, 10 eV higher energy than the O-K edge, increased remarkably compared to t_{2g} and e_g peaks by the annealing.

Introduction

Titania (TiO_2) is known as a material which shows a strong oxidative power by UV irradiation and is actively studied in the wide fields of photolysis of water, sterilization and superhydrophilic treatment of solid surfaces etc. It is desirable for titania thin films used as photocatalyst that the specific surface area of thin film is made as large as possible. We have shown that oblique columnar structures evolved in sputter deposited films when they were grown under a highly oblique angle (e.g. 80°) between the flux of sputtered particles and the substrate normal [1]. This technique is called as glancing angle deposition (GLAD) and has a potential to provide materials with a large specific surface area. We adopted this technique to prepare the TiO_2 thin film and compared the normally (0°) deposited one.

Titania is known to take crystalline structures of rutile and anatase, mainly. It is also said that the photocatalytic activity of anatase structure is much higher than that of rutile structure. However, in the preparation of TiO_2 thin film, it is sometimes very difficult to identify the structure of the thin film because the intensity of X-ray diffraction is generally very weak. In this study, we tried to identify the structure of prepared TiO_2 thin film with the use of soft X-ray absorption spectra (XAS). We also investigated to compare the difference in photocatalytic activities between as-deposited and annealed samples as a difference of electronic structures obtained by the XAS.

Experimentals

The TiO_2 thin film samples were prepared by RF-magnetron sputtering technique. A reactive sputtering deposition was carried out with a use of Ti metal target and mixture gas of Ar and O_2. The substrate was a Si wafer and the sample holder was able to tilt from the sputtered particle beam. The incident angles of sputtered particles to substrate normal were chosen 0° (normal deposition) and 80° (GLAD). A part of prepared samples were annealed at 300°C for 60 min in an air environment.

The evaluation of photocatalytic activity was conducted by measuring the absorbance change of methylene blue solution, in which prepared TiO_2 film was dipped and UV light was irradiated for 1 ~ 24 hrs with the use of a black light [2].

XAS of the samples were measured by the spectrometer at the beamline 9 (BL9) in the NewSUBARU SR facility. Total electron yield (TEY) method with sample current mode was employed for the XAS measurement. The measurement was carried out at the absorption edges of Ti-$L_{2,3}$ (~455 eV) and O-K (~530 eV). The measurement was also carried out for TiO_2 powder samples with rutile and anatase structures as references.

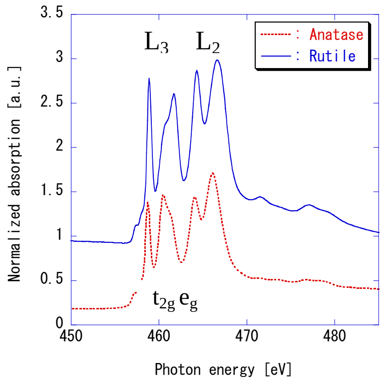

(a) Ti-$L_{2,3}$ edge

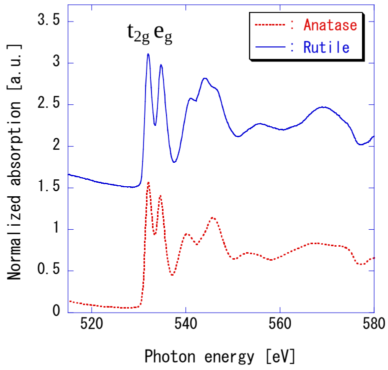

(b) O-K edge

Fig. 1 XAS of rutile and anatase powder samples.

Results

Figure 1 shows the XAS near the (a): Ti-$L_{2,3}$ edge and (b): O-K edge of rutile and anatase powder samples. Both spectra are very similar to those reported previously [3]. Ti-L_3 and L_2 resonance absorption peaks in both powder samples are split into two peaks, which is resulted from the energy split of Ti3d and O2p hybridized orbits by oxygen tetrahedral ligand field. The peaks in lower and higher energy is called “t_{2g}” and “e_g”, respectively. The spectra of Ti-$L_{2,3}$ edges for rutile and anatase powder samples are very similar in each other. The most remarkable difference in both spectra is that the peak of e_g in L_3 edge is leaned to higher energy for rutile sample and to lower energy for anatase sample.

The lower energy peaks of O-K edge for both samples are also split into two peaks, which are also resulted from the same ligand mechanism. The peaks are also called “t_{2g}” and “e_g”. In the O-K absorption spectrum, there is a broad peak at about 10 eV higher than the absorption edge at 530 eV, which is understood to be resulted from the O2p hybridized orbits with Ti4s and Ti4p.

Figure 2 shows Ti-$L_{2,3}$ XAS of TiO_2 thin films prepared by (a): normal deposition and (b): GLAD. These spectra are very similar to those of reference powder samples. As shown in Fig. 2, the e_g peak of L_3 edge split further into two peaks. These peaks are corresponded to e_g peaks of rutile and anatase structures as mentioned in Fig. 1. The intensity of both split peaks are almost the same. Therefore, we can estimate that the prepared sample contained almost the same amount of rutile and anatase crystalline structures in both samples of normal and GLAD.

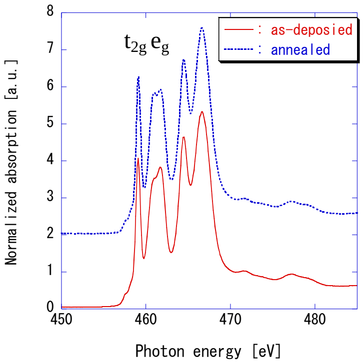

(a) Normal deposition

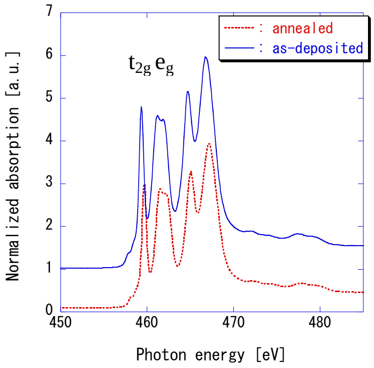

(b) GLAD

Fig. 2 Ti-$L_{2,3}$ XAS of TiO_2 thin films prepared by normal deposition and GLAD.

As shown in Fig. 2(b), anatase/rutile ratio of TiO_2 thin film deposited by GLAD was not changed by annealing with 300°C. On the other hand, as shown in Fig. 2(a) for normal deposited sample, the amount of rutile structure is a little greater than that of anatase structure in the as-deposited sample. However, anatase/rutile ratio increases slightly by annealing with 300°C.

Figure 3 shows the O-K edge spectra of normal deposited TiO_2 thin films. In the O-K edge spectral profile, the shape of t_{2g} and e_g peaks is similar to those of reference powder samples. However, the profile of broad peak at higher energy is like an intermediate shape of rutile and anatase structure. The intensity of the broad peak at the higher energy increased remarkably compared with those of t_{2g} and e_g peaks by annealing. This intensity increase by annealing was also observed in the sample of GLAD.

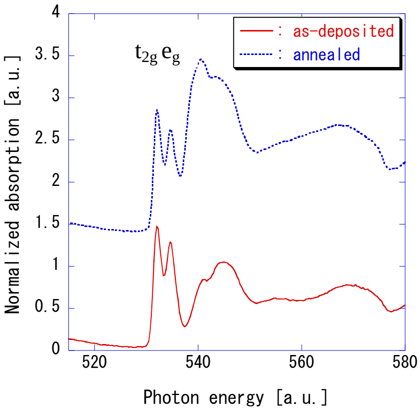

Fig. 3 O-K edge spectra of normal deposited TiO_2 thin films.

According to the experiment of photocatalytic activity evaluation, the photocatalytic activity of the film annealed at 300°C was observed to increase. Therefore, there is a good correlation between the increase in photocatalytic activity and that in absorption intensity of broad peak at higher energy of O-K edge by the annealing. There might be some relation between the local structural change by annealing and change in O2p hybridized orbit with Ti4s and Ti4p.

References

[1] S. Inoue et al., J. Jpn. Soc. Precision Eng., **72**, 919 (2006) in Japanese.

[2] “Wet dissociation test method for photocatalyst products” The Japanese Association of Photocatalyst Products 2004. 05.28, in Japanese.

[3] S. O. Kucheyev et. al., Phys. Rev. B **69**, 245102 (2004).

Development of a Soft X-ray Emission Spectrometer

Tohru Mitamura, Masahito Niibe, Yasuji Muramatsu*, Kazuo Taniguchi**
LASTI, University of Hyogo,
*Department of Engineering, University of Hyogo,
** Institute of X-Ray Technologies Co., Ltd.

Abstract

Soft X-ray emission spectrometer is currently under development to the beam line, BL9a. Outlines of the emission spectrometer are given and the progress of the development is reported.

Introduction

Soft X-ray emission spectroscopy (soft XES) provides a means of probing the partial occupied density of electronic states of a material. When energetic beams such as synchrotron radiation or ion beams are irradiated to target materials, inner shell electrons of the constitution elements of the target are excited to unoccupied levels above the Fermi level. Spectra obtained from the X-ray absorption spectroscopy (XAS) reflect the electron density distribution of unoccupied energy levels.

To the radiation-induced inner shell holes, electrons of the occupied higher energy states transit to the holes and X-rays with excess energy are emitted subsequently. Spectra obtained from the XES reflect the electron density distribution of the occupied energy levels under the Fermi level. XES is element- and site-specific, hence it is a powerful tool for determining detailed electronic properties or chemical structure of materials.

As the X-ray emission is a relaxation process following primary X-ray absorption one, the intensity of emitted X-ray is generally very weak. Accordingly, the soft X-ray emission spectroscopy requires intensive excitation source, in anyway we can use ion beam or light source, so as to accomplish a high precision experiment within a limited amount of time. Hence light source with high luminosity from a synchrotron radiation is advantageous.

The beam line, BL-9a, with the long undulator emission provides energy-variable intensive light source. To this beam line, a soft XAS system has been applied and effectively utilized for investigation of surface structure of solids. In addition to the soft XAS system, it is desirable to equip a soft XES system so as to improve detecting systems for the phenomena related to soft X-rays. In the present report, basic outline and progress situation of the soft XES under development are reported.

Outline of the soft XES under development

The soft XES under development is a type of the wavelength dispersive X-ray spectrometer (WDS). It has been originally designed by the group of one of the authors, K. Taniguchi, for observation of photo-emission phenomena from target materials irradiated by energetic-ions. In the present development, the design of the spectrometer is modified and improved to install to BL-9a of the New SUBARU.

Fig.1, shows the partially build-up inner parts of the spectrometer. In the figure, S, G and D are the emitted X-ray entrance slit, the diffraction grating and the CCD detector, respectively. The S and G are attached to a support frame which is fixed to the flange F1. The F1 is connected to a port of the target chamber. The detector D is mounted on a support frame which is fixed to the flange F2. The F2 is independently shifted the position in the horizontal (X-axis) and the vertical (Y-axis) directions in order to lie the detector on a circle called the Rowland circle.. The angle of D (θ-axis) can be adjusted so that the surface is tangent to the Rowland circle. Each movement of three axes is driven by a stepping motor. The F1 and F2 are connected by a welding bellows.

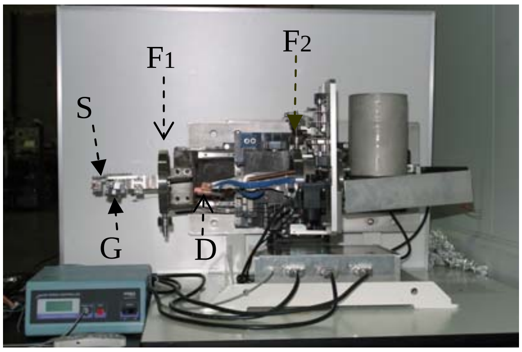

Fig.1 Inner view of the X-ray emission spectrometer (XES). S: entrance slit, G: concave diffraction grating, D: CCD detector. F1and F2 are conflate flanges. They are connected by a welding bellow.

The stepping motors are Oriental motor products. The ones for X and Y axes are equipped with magnet brakes. All of the motors are driven and controlled by a driver and controller unit, Mark204-MS, which is a Sigma-koki product. This unit is equipped by a GPIB terminal through which the system is controlled by a personal computer, using the software, LabVIEW.

The grating is a type of concave diffraction grating with 3600 lines/mm. The CCD detector is two dimensional type with the area of 10x28 mm^2. The center of the detector is set so as to be tangent to the Rowland circle, hence peripheral aberration is processed by an image-processing method in order to maintain the good resolution. The CCD detector is cooled through a cold finger attached to the cylindrical Dewar vessel which can be seen in the Fig.1.

We have also another detector, silicon drifted detector (SDD). This is a type of energy dispersive X-ray spectrometer (EDS). The WDS detector has an advantage of good resolution and a disadvantage of long measurement time. In contrast, EDS detector has an advantage of short measurement time and a disadvantage of low resolution. According to experimental purposes, EDS is more suitable than WDS. We have a plan to attach the SDD to a port of the target chamber.

Fabrication of Narrow Pitch and High Aspect Ratio Microcoils for Electromagnetic Microactuators

Daiji Noda, Yoshifumi Matsumoto, Masaru Setomoto, and Tadashi Hattori
Laboratory of Advanced Science and Technology for Industry, University of Hyogo

Abstract

The demand of micro-fabrication such as microactuators, microcoils, smart sensors is increasing. Actuators, which held big volume and weight with a part of a product, have been required to reduce their size. However, the miniaturization of electromagnetic actuators has made little progress since it requires three-dimensional micro-fabrication processing and new technologies. Therefore, we have fabricated a spiral microcoil with narrow pitch and high aspect ratio coil line structures using a deep X-ray lithography and metallization techniques. We have fabricated spiral microcoils at a pitch of 20 μm. Thus, an aspect ratio of coil lines was achieved about 5 as coil lines of 10 μm. In the case of 30 μm line and space pattern, we obtained an aspect ratio of about 3. By using these techniques, microcoils with narrow pitch and high aspect ratio can be achieved, which are expected to yield high performance.

Introduction

Recently, the demand of micro-fabrications such as microactuators, microcoils, sensors, etc is very increasing. Actuators, which hold big volume and weight with a part of a product, have been required to reduce their size. However, the miniaturization of actuators has made little progress since it requires three-dimensional (3D) micro-fabrication processing and new technologies. On the other hand, LIGA (German acronym for Lithographite Galvanoformung and Abformung) process [1] can be fabricated nano and micro parts for devices. This technique is possible to make high aspect ratio structure fixed the narrow pitch of coil line and space. In addition, the X-ray exposure stage was carried out with the workpiece held in a specially manufactured nine parts operation [2]. Thus, this stage makes it feasible to do 3D deep X-ray lithography for microcoils. Therefore, we have fabricated a spiral microcoil with high aspect structure for electromagnetic type microactuators using a 3D deep X-ray lithography and metallization techniques.

Design of electromagnetic actuator

As the structure of the magnetic circuit, we used the type called *open frame solenoid*, which is open on the sides [3]. The material of electromagnetic core (fixed core and plunger) and shield parts (yoke) were used Permalloy that is a nickel iron alloy, because it has the largest permeability among soft magnetic metals. When the electrical supply to the coil is turned on, a magnetic flux forms in the gap, deforming the magnetic field and producing suction force on the plunger. If the aspect ratio is increased, the cross section area of coil lines is also increased allowing a greater current path. Then, the magneto motive force is proportional to the squares of current path in the microcoil in this model. This microactuator having the high aspect ratio of coil line is also expected a high performance in spite of miniature size.

Fabrication process of microcoil

X-ray lithography was carried out for deep X-ray lithography in New SUBARU synchrotron radiation facility of our university at the operation energy of 1.5 GeV. The surface of acrylic pipe for a screw thread structure, this is the coil part, has made using LIGA process.

Figure 1 shows the fabrication process of microcoil. First, a cylindrical structure was formed on the surface of acrylic pipe by X-ray lithography. Next, copper was thinly deposited on pipe surface by sputtering in order to use as a seed layer in the electroforming. And, copper was formed into narrow pitch spiral structure by electroforming. Then, pipe surface was completely covered with copper film. Finally, forming Cu layer over the pipe surface was etched until the isotropic portions of wiring were

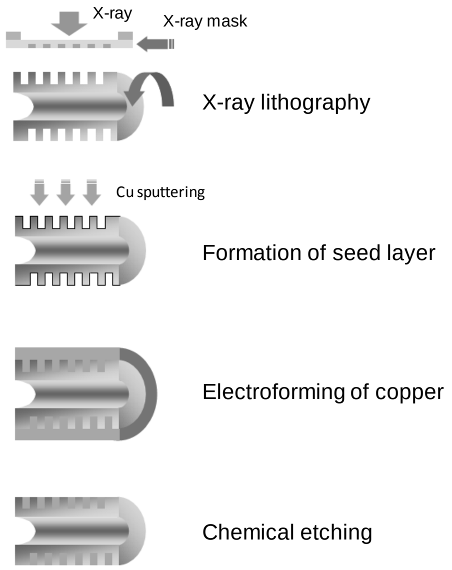

Fig. 1: *Process flows of microcoil*

exposed. We have fabricated a spiral microcoil at a pitch of 20 μm, as shown in Fig. 2. Thus, an aspect ratio of coil lines was achieved about 5 as coil lines of 10 μm. In the case of 30 μm line and space pattern, we obtained the aspect ratio of 3. Following the seed layer deposition, we formed uniform copper electroplating for the current path of microcoils. In this result, it was able to be confirmed that plating developed to reach the bottom surface of the grooves, as shown in Fig. 3. Finally, Isotropic copper etching was performed until the insulated portions of the wiring were exposed, as shown in Fig. 4.

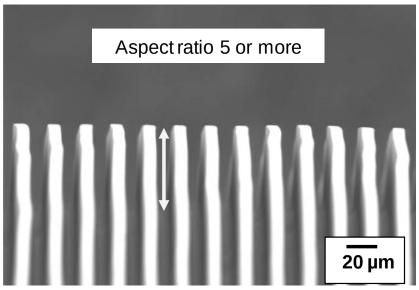

Fig. 2: *SEM image of coil lines with aspect ratio of 5*

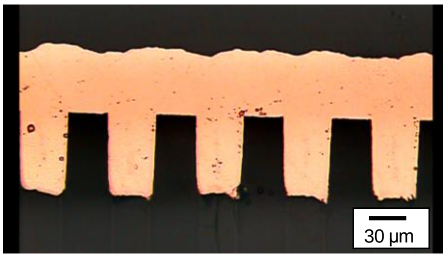

Fig. 3: *SEM image of coil lines after copper electroforming*

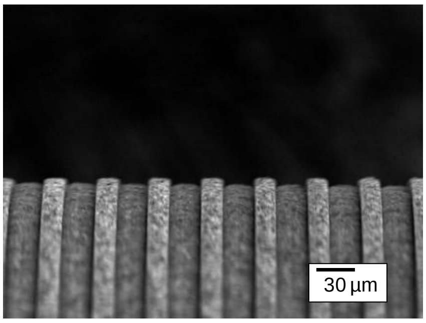

Fig. 4: *SEM image of coil lines by isotropic copper etching*

Measurement of suction force

We have also fabricated a measurement system to measure the suction force of designed electro-magnetic type actuators. This system is very simple structure and easy to exchange the coil part. The gap between plunger and fixed core was adjusted X-, Y-stage. The theoretical values by simulation and actual measurement results of suction force generated by the microcoil were compared, as shown in Fig. 5. These results are relatively in good agreement with theoretical values.

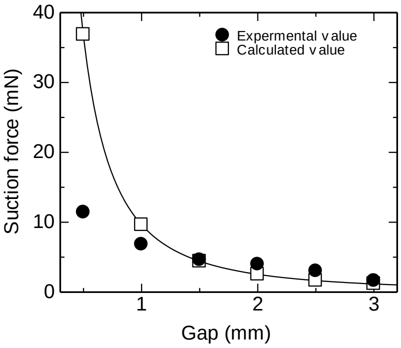

Fig. 5: *Suction force comparison between measurement values and simulation results*

Conclusions

We have fabricated microcoils with high aspect ratio using a 3D deep X-ray lithography and metallization technique in order to produce electromagnetic microactuators. We succeeded in producing a threaded structure with10 μm in coil lines width and about 5 in the maximum aspect ratio. On the other hand, we produced a measurement system to measure a suction force. In this measurement, theoretical values by simulation results and actual measurement of suction force were compared. By using these techniques, microcoils with high aspect ratio can be achieved, which are expected to yield high performance. It is anticipated that high performance microcoils could also be manufactured, in spite of their miniature size.

Acknowledgment

This research is partially supported by the Grant-in-Aid for Scientific Research on Priority Area, No. 438, "Next-Generation Actuators Leading Breakthroughs", from the Ministry of Education, Culture, Sports, Science and Technology, Japan.

References

[1] E. W. Becker, W. Ehrfeld, P. Hagmann, A. Maner, and D. Munchmeyer, Microelectron. Eng., **4**, pp. 35-56 (1986).
[2] H. Mekaru, S. Kusumi, N. Sato, M. Yamashita, O. Shimada, and T. Hattori, Jpn. J. Appl. Phys., **43**, 6B, pp. 4036-4040 (2004).
[3] Y. Matsumoto, M. Setomoto, D. Noda, and T. Hattori, Microsyst. Technol., **14**, 9-11, pp. 1373-1379 (2008).

Fabrication of X-ray Grating Using X-ray Lithography Technique for X-ray Phase Imaging

Daiji Noda, Hiroshi Tsujii, and Tadashi Hattori
Laboratory of Advanced Science and Technology for Industry, University of Hyogo

Abstract

X-ray radiographic imaging technique is very important in medical, biological, inspection, material science, and so on. However, it is not enough to obtain clear X-ray images of samples with low absorbance materials, such as biological soft tissues. Then, we have used an X-ray phase imaging method of an X-ray Talbot interferometer. In this method, X-ray gratings were required to have narrow pitch and high aspect ratio structure. Therefore, we have developed and fabricated high aspect ratio X-ray gratings with a pitch of 5.3 μm, a height of 30 μm, and a large effective area of 100 mm × 100 mm using X-ray lithography and narrow electroforming technique. In this paper, we discuss the fabrication process of X-ray gratings and results of X-ray phase tomography using an X-ray Talbot interferometer with these X-ray gratings.

Introduction

X-ray radiographic imaging technique is very important in medical, biological, inspection, material science, and so on. However, it is not enough to obtain clear X-ray images of samples with low absorbance materials, such as biological soft tissues. On the other hand, several methods for generating radiographic contrast from the information of X-ray phase shift have been investigated. It is improvement in the high sensitivity by about 1000 times higher than by conventional absorption contrast.

Numerous researchers have studied a variety of methods of phase imaging [1,2]. X-ray Talbot interferometer (XTI) is one of the methods of X-ray phase imaging [1]. It offers many advantages: a) it is a very simple setup using two gratings; b) it does not need a high mechanical stability; c) a widely area imaging is possible; d) a detector for imaging does not need a high resolution, and e) it functions with a broader energy band width much than in the case of using crystal optics. Therefore, these advantages have made the XTI attractive for application in medical diagnostics. In order to use 10-40 keV X-ray irradiation, the Au thickness of absorptive material must be over 20 μm. But, it is not straightforward to make this structure with high aspect ratio by conventional techniques. Then, we have tried in fabricating such X-ray gratings particularly with a large area (100 × 100 mm^2) using X-ray lithography technique.

Fabrication of X-ray mask

First, we fabricated an X-ray mask for grating patterns. For large effective area of X-ray grating, we developed a large area X-ray mask structure. Figure 1 shows fabrication process of X-ray mask for X-ray grating pattern with pitch of 5.3 μm [3]. A titanium film was formed on Si substrate by sputtering to serve as electroforming of Au absorptive material. Next, negative type photoresist of SU-8 was spin coating and patterning by ultraviolet (UV) lithography technique. In this research, a pitch of 5.3 μm and a height of 4 μm resist pattern were fabricated. Au was formed into resist structure of narrow lines by electroforming. And, we have used SU-8 as membrane because of large effective area X-ray mask. In this study, SU-8 was spin coated at 40 μm thickness. We attached a SUS frame on membrane in order to support X-ray mask. Finally, Si substrate and Ti seed film were removed by wet etching with potassium hydroxide (KOH) and buffered hydrogen fluoride (BHF) solution, respectively. We succeeded in making X-ray mask with pitch pattern of 5.3 μm and large effective area of 100 × 100 mm^2.

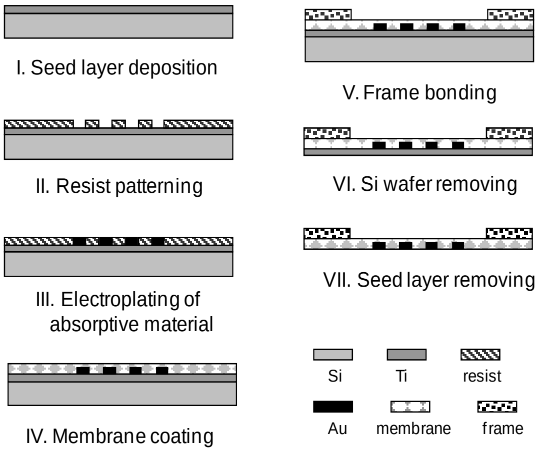

Fig. 1: *Fabrication process of X-ray mask*

Fabrication of X-ray grating

The X-ray lithography using synchrotron radiation has been utilized for 2.5-dimensional applications on flat substrate. Therefore, we took advantage of this technology to fabricate a high aspect ratio structure required for X-ray gratings with a pitch of several micrometers. For X-ray lithography, we used NewSUBARU beamlines 2, which is the synchrotron radiation facility owned by our university [4]. The beamline 2 has a potential of large area patterning across an A4-size area with a highly uniform pattern thickness.

A target specification of the X-ray grating was 5.3 μm pitch pattern and large effective area of 100 × 100 mm^2. For the deep X-ray lithography, we used a negative photo-resist SU-8. This SU-8 was originally designed for UV lithography. However it could also be used in deep X-ray lithography of high accuracy and high aspect ratio pattern. The pattern quickly collapses when the rinse solution is dried in the development and washing process, as shown in Fig. 2. In order to solve this problem, we used supercritical washing and drying machine (product by RyuSyo Industrial Co., Ltd.) using carbon dioxide (CO_2) as the supercritical fluid because it is safe and has a low critical point lower than those of other fluids. Figure 3 shows an image of high aspect ratio structure without sticking. From this figure, processing depth was obtained about 35 μm with narrow pitch of 5.3μm. Thus, an aspect ratio was achieved of about 13.

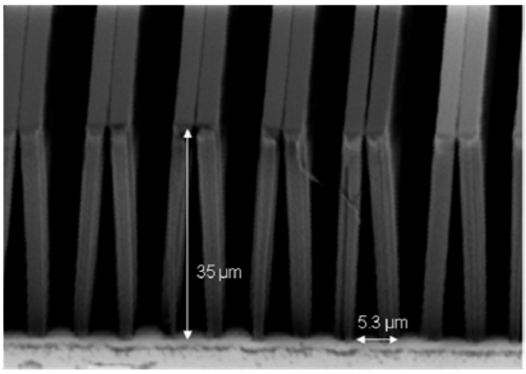

Fig. 2: *SEM image of narrow pitch structure with sticking*

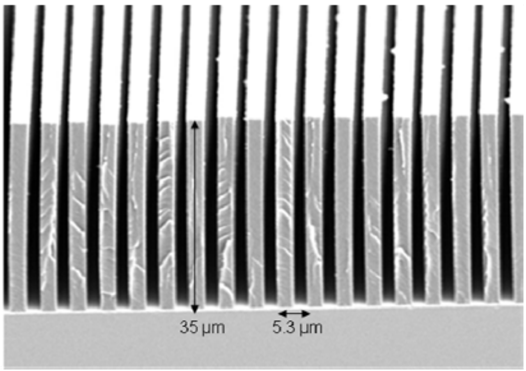

Fig. 3: *SEM image of narrow pitch structure without sticking*

Au absorbing part for the X-ray grating was formed by electroforming. In electroforming, chromium was used as seed film. A non-cyanic based solution was used for Au electroforming. From these results, the designed pitch of 5.3 μm and height of about 30 μm of X-ray grating are realized [5], as shown in Fig. 4. Next target of X-ray grating is improvement of precision, smaller pitch and higher aspect ratio structure.

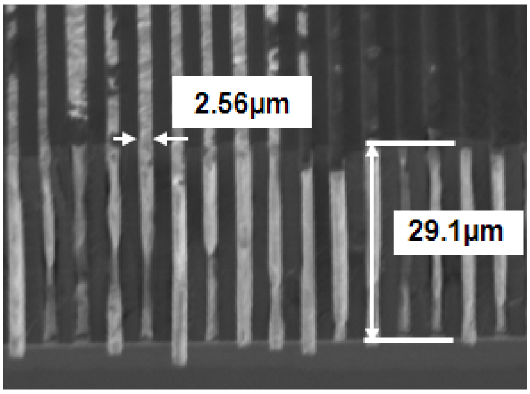

Fig. 4: *SEM image of X-ray grating in cross section*

Conclusions

We have fabricated X-ray gratings having a pitch of 5.3 μm and a large effective area of 100 × 100 mm^2 for X-ray Talbot interferometer of use in X-ray phase imaging. To make a higher aspect ratio X-ray grating, we developed the fabrication process composed of X-ray lithography and micro electroforming method. In X-ray lithography, sticking was observed because of surface tension. Therefore, we introduced a supercritical washing and drying machine using CO_2 as the supercritical fluid. In this result, the resist structure with high aspect ratio and narrow pitch was obtained without surface tension in large area, such as effective area of 100 × 100 mm^2. After Au electroforming, large area and narrow pitch X-ray grating could be fabricated.

This result suggests that XTI is a novel and simple method for phase sensitive X-ray radiography, and promising method for many imaging applications.

Acknowledgment

This research was supported by the research project “Development of Systems and Technology for Advanced Measurement and Analysis” from the Japan Science and Technology Agency (JST).

References

[1] A. Momose, Jpn. J. Appl. Phys., **44**, 9A, pp. 6355-6367 (2005).
[2] C. David, B. Nöhammer, H. H. Solak and E. Ziegler, Appl. Phys. Lett., **81**, pp. 3287-3289 (2002).
[3] D. Noda, M. Tanaka, K. Shimada, and T. Hattori, Jpn. J. Appl. Phys., **46**, 2, pp. 849- 851 (2007).
[4] Y. Utsumi, T. Kishimoto, T. Hattori, and H. Hara, Microsyst. Technol., **13**, 5-6, pp. 417-423 (2007).
[5] D. Noda, H. Tsujii, N. Takahashi, and T. Hattori, J. Electrochem. Soc., **156**, 5, pp. H299-H302 (2009).

Fabrication of Micro Capacitive Inclination Sensor by Resin Molding

Hiroaki Miyake[1], Kazufumi Nishimoto[1], Satoshi Nishida[2], Daiji Noda[1], and Tadashi Hattori[1]
[1]Laboratory of Advanced Science and Technology for Industry, University of Hyogo
[2]Nanocreate Co., Ltd.

Abstract

In various leading-edge technology industries, there is a growing need to reduce the weight and increase the energy saving performance of various electronics products. Less costly production technology is now under development to enable the production of less expensive MEMS devices. In this situation, there is a pressing need to develop micromachining technology and a production process suitable for mass produced MEMS. The LIGA process is a technology, which is considered to be suited for mass production, enabling the creation of a microstructure by transferring a pattern from this master mold to a resin. In this study, we fabricated a micro capacitive inclination sensor by using combination of a resin forming method and a mold. If a small inclination sensor, having a size of several millimeters, could be made using a resin forming method, production costs could be substantially reduced compared to sensors made with the conventional MEMS process.

Introduction

In various leading-edge technology industries, there is a growing need to reduce the weight and increase the energy saving performance of various electronics products. Although MEMS (Micro Electro Mechanical Systems) technology [1] is not suited for mass-produced sensors since silicon is brittle and expensive and its processing is complicated, involving many processes. The LIGA process is a technology, which is considered to be suited for mass production, enabling the creation of a microstructure by transferring a pattern from this master mold to a resin.

In this research, we fabricated a micro capacitive inclination sensor [2] by using combination of a resin forming method and a mold. If a small inclination sensor, having a size of several millimeters, can be made using a resin forming method, production costs can be substantially reduced compared to sensors made with the conventional MEMS process. Since the dimensions of its sensing region are $5 \times 5 \times 3$ mm^3, which are much smaller than the dimensions of conventional sensors, this inclination sensor is expected to be widely used in the field where efficient and reliable attitude control is a primary factor to be considered.

Micro capacitive inclination sensor

Figure 1 shows the working principle of a micro capacitive inclination sensor fabricated in this study. Two semicircular opposing electrodes are set above one circular common electrode, as shown in Figs. 1a and 1b, so that two capacitors are formed. The region between the opposing electrodes and common electrode is half filled with oil. The oil inside maintains its level due to gravity when the sensor inclines, so that the amount of oil changes in each capacitor, as shown in Fig. 1c. As a result, the capacitances change, and the angle of inclination of the sensor can be detected, based on this change in the capacitance values. Capacitance change of the capacitor on the one side of the electrodes ΔC is expressed the proportional inclination angle θ [2].

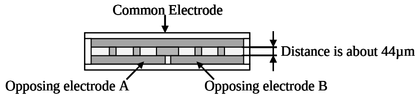

(a) Section structure

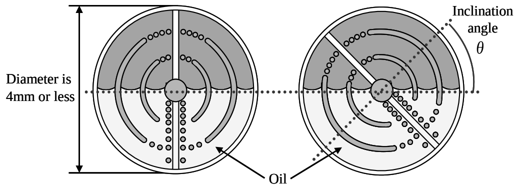

(b) Horizontal (c) Inclination

***Fig. 1:** Principle of micro capacitive inclination sensor*

Fabrication process of sensor

Figure 2 shows the fabrication process for the micro capacitive inclination sensor. In the first step, the spacer part of this mold was transferred to a resin by hot embossing molding [3]. The common electrode was formed on the molding prepared. Specifically, an electrode film was formed, only at the recesses on the slit-structured surface having projections and recesses. A patterning method using a mask would be a viable method for forming an electrode at a specified position. Using this method, however, it is very difficult to bring a mask into proper alignment with a non-flat surface; this method also has a drawback in respect of cost. In the case of the process that is the subject of this paper, a significant cost reduction is possible, since an electrode film can be formed without using a mask.

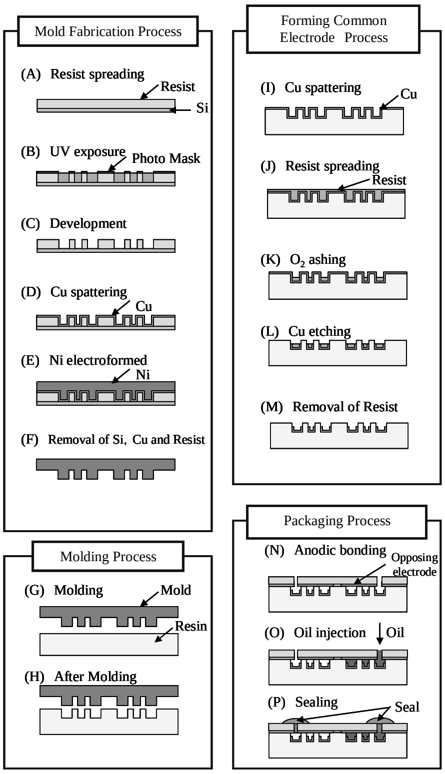

Fig. 2: *Fabrication process for sensor using molding*

Formation of electrode on resin molding

The inclination sensor comprises two electrodes, i.e., a common electrode and opposing electrode, to form a capacitor. Figure 3 shows images of the cross section of a molding on which resist had been coated, using a spin/spray coating system. As shown in this image, resist smoothly followed the projections and recesses in the pattern. After resist coating, the thickness of the resist film on the electrode region was the same at that of the film on the junction region. Therefore, if O_2 ashing were performed on a molding having a uniform thickness of resist, resist could not remain only in the recess in the electrode region. Therefore, we placed a resist-coated sample in a container filled with solvent vapor so that resist, exposed to solvent vapor, would melt and be planarized. As is evident from Fig. 3b, the resist coating on the junction part was very thin, compared with a sample, shown in Fig. 3a, which had not yet been planar. Cu electrode was thus formed successfully, only in the recess in the structure, using the proposed new process.

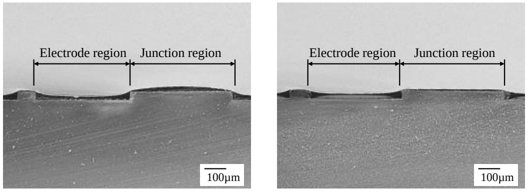

(a) after resist coating *(b) resist had been planer*

Fig. 3: *SEM image of pattern in cross section*

We successfully fabricated a micro inclination sensor as a molded product. In future, we will carry out wiring to complete this inclination sensor, and then conduct performance evaluations, as shown in Fig. 4.

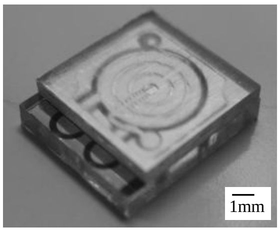

Fig. 4: *Picture of completed sensor*

Conclusions

Based on low cost molding techniques suited for mass production, we have fabricated a micro capacitive inclination sensor by using a resin molded component. We prepared a mold by UV lithography and Ni electroforming. In addition, using the hot embossing molding technique, we fabricated a structure in which our pre-designed projections and recesses were realized. We proposed a new process for forming electrodes, only in the recesses in a fabricated resin molded component, without using a mask, and successfully fabricated the common electrode of an inclination sensor. The process proposed and established in this study requires no alignment and makes possible a substantial cost reduction. Although we faced a difficult task of planarizing resist in this process, we used solvent vapor for planarization with satisfactory results. We successfully fabricated a micro inclination sensor as a molded product. In future, we will carry out wiring to complete this inclination sensor, and then conduct performance evaluations. The techniques using resin-molded parts have the potential to be applied to the production of, not only inclination sensors, such as the one fabricated in this study, but also MEMS devices. If the techniques using resin-molded parts are introduced to the mass-production of MEMS devices, including sensors, at low cost, the range of their applications will further expand to new areas of technology and industry.

References

[1] F. Kohsaka, J. Liang, T. Matsuo, and T. Ueda, IEEJ Trans. SM, **127**, 10, pp. 431-436 (2007).

[2] H. Ueda, H. Ueno, K. Itoigawa, and T. Hattori, IEEJ Trans. SM. **126**, 12, pp. 637-642 (2006).

[3] N. Ishizawa, K. Idei, T. Kimura, D. Noda, and T. Hattori, Microsyst. Technol., **14**, 9-11, pp. 1381-1388, (2008).

Fabrication of Ultraviolet Range Light Guide Plate

Yuta Okayama[1], Kenji Yamashita[1], Yoshitaka Sawa[2], Daiji Noda[1], and Tadashi Hattori[1]
[1]Laboratory of Advanced Science and Technology for Industry, University of Hyogo
[2]Sawa Plating Co., Ltd.

Abstract

The light guide plate, as part of the backlight unit in a cellular phone or liquid crystal display, has evolved to meet market demands for low power consumption, high-luminance and high-quality displays. Along with the advance of the light guide plate, LEDs have undergone development as light source for light guide plates. Surpassing the limitations of LED emission in the visible light range, LEDs that emit ultraviolet light have been developed. In recent years, the ultraviolet light are used as a source of light of the air cleaner, and it is used as a source of light to activate the titanium oxide which is photocatalyst. Common ultraviolet light sources are either line or point light sources. There are no surface light sources capable of providing uniform lighting. We studies surface illuminators that incorporate diffusers in the visible light range. Applying our existing technology, we constructed an unprecedented ultraviolet surface illuminator and measured it using a photocatalyst.

Introduction

In recent years, liquid crystal displays (LCDs) have come to be widely used in cellular phones and TV sets. This popularity has led to growing demand for a higher performance light guide plate as an LCD component. In the light guide plate, light is guided from a light emitting diode (LED) or other point light source to desired locations via total internal reflection rendered by index of refraction differential between air and diffuser material. The light in light guide plate tears a total reflection condition by reflecting in an internal projection (dot) and irradiates the surface. The light guide plate, converts point light source to surface illumination. Figure 1 shows a schematic diagram of a light guide plate. One advantage of the light guide plate is its efficient use of light through the conversion of point light source to surface illumination. Our laboratory conducts studies on the design of a light guide plate that achieves a high uniformity ratio [1]. To apply our technology to surface illuminators using ultraviolet (UV) light, which have begun to be used recently in home air cleaners, we have embarked on fabricating a light guide plate specifically designed for UV LEDs. For light guide plate fabrication, we used UV-LIGA process, which enables fine pattern processing technologies [2]. And, we proposed to termed UV diffraction exposure in order to form a fine, three-dimensional bump shape [1].

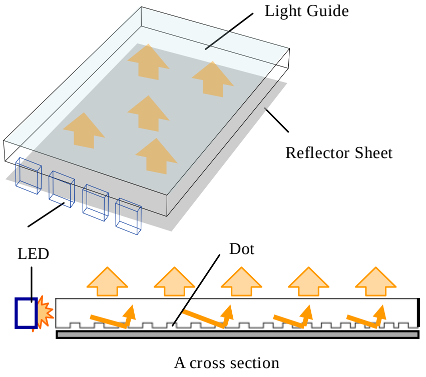

***Fig. 1:** Schematic diagram of light guide plate*

In this study, optimal bump shape and allocation were derived for UV surface illuminators. Indeed, a light guide plate was fabricated using the molding technology.

Design of light guide plate

In achieving uniform surface illumination with a light guide plate alone, it is very important to form the shape and allocation of reflective bumps. Optimization of bump shape and allocation enables the creation of a light guide plate for uniform illumination. A ray-tracing simulator was used to derive the optimal bump shape and allocation. First, the optimal bump shape was obtained. The bump shape was transformed from a cylindrical column to a truncated cone, using fixed dimensions of 30 μm height and 52 μm base diameter. Simulation results revealed that strong light was emitted near 60 to 70 degrees taper angle, as in the visible light range. In the next step, emission angle distribution was obtained for 60 and 70 degrees taper angle truncated cones. As suggested by the results, high output and maximum perpendicular emissions from the surface are achieved from a truncated cone with a 70 degrees taper angle.

In the next step, optimal bump allocation was derived for the 70 degrees taper angle. In this study, the light guide plate we fabricated had bumps in a 48 by 88 mm area on a 52 by 96 mm board 2.6 mm thickness. The optimal bump allocation was determined by thinning filled bumps, on the basis of simulation results. The bumps were selected randomly. Therefore, the process was repeated to derive the optimal bump allocation for uniform illumination. Figure 2 shows simulated analysis results. The fully uniform placement of bumps was obtained. Before bump allocation optimization, output characteristics were such that the maximum value was 6.39W/m^2 and the minimum value was 1.15 W/m^2. After optimization, the maximum value was reduced to 3.23 W/m^2, while the minimum value was increased to 1.82 W/m^2. The uniformity ratio, which is an indicator of the degree of illumination uniformity, improved from 35% to 91%.

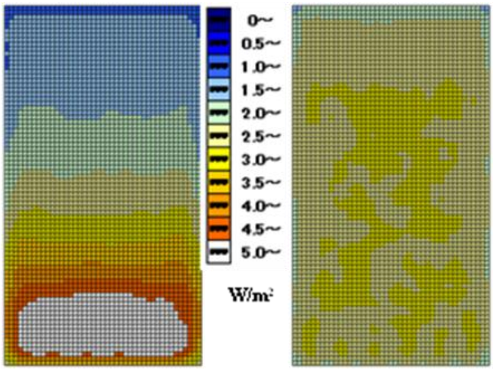

(a) Uniform arrangement (b) Optimum arrangement

Fig. 2: *Energy distribution of light guide plate*

Fabrication of light guide plate

Since the shape was micro sized, the UV-LIGA process was used to fabricate an ultraviolet light guide plate, designed as above. As regards the master pattern, a structure was created by lithography, painting with resist that is photosensitive resin wafer. Next, copper was sputtered onto the surfaces of the created master pattern. A mold was then fabricated through Ni electroforming. Since the light guide plate was to be fabricated by injection molding, it was necessary to set the size to accommodate a cavity for injection molding. Consequently, the Ni thickness was set at approximately 4 mm for electroforming. Lastly, the light guide plate was produced through injection molding using the mold as a cavity. Figure 3 shows the exterior and an SEM image of the injection molded light guide plate. The achieved bump shape was obtained at 10 μm in top diameter, 52 μm in base diameter, 70 degrees in taper angle and 30 μm in height.

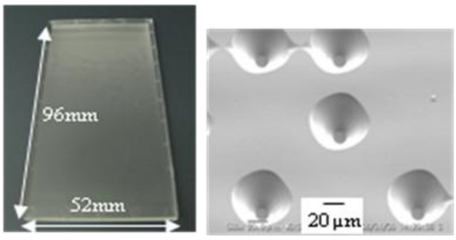

Fig. 3: *Top view and SEM image of fabricated light guide plate*

Evaluation of light guide plate

Using a photodiode, the emission characteristics of the fabricated light guide plate were measured to verify that the light guide plate would provide uniform illumination. Energy values were calculated from the spectral response characteristics of the photodiode and the wavelength of the light emitted by the LED. The energy distribution was obtained as closely simulation result, as shown in Fig. 4. In the simulation, the maximum and minimum values were 3.23 W/m^2 and 1.82 W/m^2, respectively, while the molded light guide plate provided maximum and minimum values of 4.25 W/m^2 and 3.10 W/m^2, respectively. The maximum value increase from the simulation results was probably due to some entry angle deviation that occurred at LED mounting. However, the higher minimum value suggests that the fabricated light guide plate was better than the simulated one used for analysis.

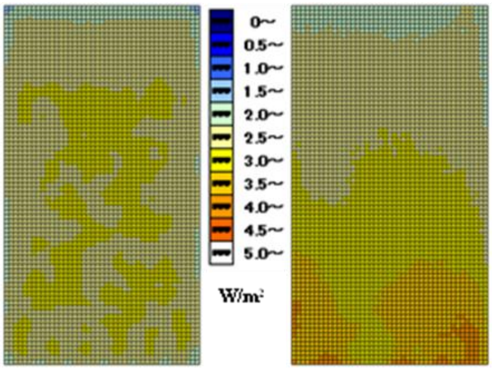

(a) Simulation result (b) Measurement result

Fig. 4: *Energy distribution of light guide plate*

Conclusions

We fabricated an unprecedented UV surface illuminator and assessed its capacity as a light source for reactivating photocatalysts. Bump shape and allocation for uniform illumination of UV light were derived through simulation, achieving uniformity ratio improvement from 35% to 91%. The light guide plate for ultraviolet light was fabricated through application of visual-light diffuser fabrication techniques, i.e., the UV-LIGA process and UV diffraction exposure. The fabricated light guide plate presented performance comparable to simulation results, with a minimum value exceeding analysis results, though the uniformity ratio did not reach the simulation results.

References

[1] T. Tanaka, T. Nomura, Y. Funabiki, T. Kitadani, K. Idei, K. Yamashita, D. Noda, and T. Hattori, Proceedings of the 2006 IEEE International Symposium on Micro-Nano Mechatronics and Human Science, Nagoya, Japan, pp. 480-485 (2006).

[2] Y. Sawa, T. Tanaka, T. Kitadani, H. Ueno, Y. Itoigawa, K. Yamashita, D. Noda, and T. Hattori, Microsyst. Technol., 14, pp. 1559-1565 (2008).

Fabrication of the 3 Dimension Resist Microstructure Using X-ray Diffraction and Applying to LIGA Process

Daiji Noda[1], Kyo Tanabiki[1], Yoshitaka Sawa[2], and Tadashi Hattori[1]
[1]Laboratory of Advanced Science and Technology for Industry, University of Hyogo
[2]Sawa Plating Co., Ltd.

Abstract

The LIGA process consists of lithography, electroforming and molding has attracted attention in microstructure fabrication techniques. At the molding process of LIGA process, it is difficult to pull out from the mold that is assumed of especially high aspect ratio structure. However, release from mold is improved by tapered structure. In this research, we proposed that the diffraction exposure technique which makes use of diffraction phenomenon. Diffraction is caused by providing a clearance between a resist structure and an X-ray mask. The fabricated structure was the lines and intermediate space whose processed width was 200 μm and designated the taper angle 5 degrees as set point. The experiment parameters were done by distance of gap, dose of X-ray and slit width. It is controlled that discovering the conditions for taper angle of 5 degrees and inspecting the relationship between taper angle and mold releasability by electroforming and the molding of the LIGA process. We have fabricated a mold with taper angle of 2.5 degrees by electroforming. The Ni mold could partially copy the master pattern well.

Introduction

Today, People are surrounded by abundant cellular phones and other information processing equipment, including computers, liquid crystal televisions, portable music players, automobiles, and so on. With these products, it is understandable that the market demands higher performance. In order to meet such demands, the development of parts with reduced size and increased performance is under way. For size reduction and performance improvement, micro-structures and micro-systems are attracting engineers' attention. The fabrication of micro-structures has progressed technical improvements in the fields of machining and Micro Electro Mechanical Systems (MEMS) technology.

Sensors are fabricated through established semiconductor processing technology, which uses a planar processing technique. But, actuators of complex shape require the use of micro 3D structure processing technique. At present, the most promising fabrication technology for micro 3D structures is the LIGA process [1]. This process is a combination of technologies such as a metal mold master making the deep X-ray lithography with the sub-micrometers pattern formation, electroforming of nickel mold, and precise molding that use the metal mold that comparatively have generality.

Removing a cast from mold in molding of LIGA process, especially in the case of high aspect ratio structures, requires an elaborate design. Otherwise, it is impossible to remove the cast without breaking the structure. The mold releasing property of a structure improves if structure is tapered. In this paper, we have proposed a method of achieving a tapered shape, by means of a gap provided for X-ray diffraction between X-ray mask and resist structure for mold master. The structures reported in this paper feature lines and intermediate spaces. Target values were 200 μm in processing width, 5 degrees in taper angle, and large effective area of over 40 × 45 mm^2.

Experimental method

To fabricate for high aspect ratio 3D structures, we have used the NewSUBARU synchrotron radiation facility of University of Hyogo. For X-ray lithography, beamline 2 (BL-2) has a potential of large area patterning across up to full-A4-size area with a highly uniform pattern thickness. Due to its high directivity, synchrotron radiation light is commonly used to create 2.5-dimensional structures. However, it is possible to cause X-ray diffraction by providing a large gap between X-ray mask and resist structure. Exposure using of the diffraction enables the fabrication of a tapered 3D structure [2].

In this research, for the purpose of substrate preparation, a polymethylmethacrylate (PMMA) sheet with 200 μm in thickness, which is a positive type photoresist, was affixed to a silicon substrate by the bonding method, a method of forming a photoresist. In this method, a PMMA solution, which serves as adhesive, is fed between a PMMA sheet of desired thickness and a silicon wafer, or substrate; pressure is then applied to the PMMA sheet with a machine press to spread the PMMA solution to a uniform thickness, and the PMMA sheet is bonded to the silicon substrate by polymerization of the solution to form a resist. Figure 1 shows an outline of the X-ray diffraction method used for creating lines and intermediate spaces. For the diffraction of X-ray exposure, two types of simple jig were made and used to enable gap adjustment by replacing the spacer. The two jigs differed in spacer thickness for gap adjustment. One was capable of adjusting the gap between 40 and 80 mm, while the other was enabled adjustment from 120 to 150 mm gap.

In this paper, parameters for diffraction were used

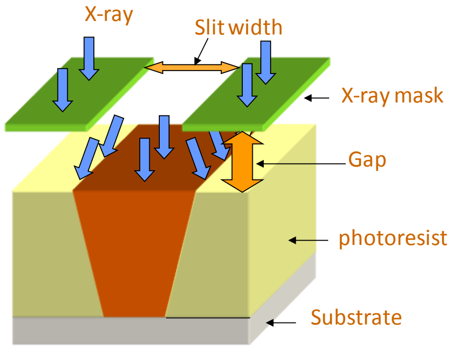

Fig. 1: *Image diagram of tapered structure and outline of X-ray diffraction*

slit width, dose of X-ray and gap between X-ray mask and resist structure, which were varied. These quantities were selected as parameters, since it was believed that slit width and gap would affect diffraction and the dose of X-ray would exert an effect on processing width as well as on diffraction. The cross section of the structure was observed with a scanning electron microscopy (SEM) for evaluation of processing width. The top and bottom widths of the tapered groove were measured by SEM, and the taper angle was determined by calculation.

Results and discussions

The processing width and taper angle of the tapered groove were observed with different values of the three parameters [3]. Figure 2 shows results of upside and downside widths and taper angle obtained at varying gaps as a graph. Both processing width and taper angle increased with increasing gap. A possible reason for the increased processing width is that the increased gap caused greater diffraction, resulting in X-ray exposure of some areas of the resist structure, which were not otherwise X-ray exposed when the gap was small. If the gap is further increased, diffracted synchrotron radiation light beams may interfere with one another after passage through slits. The reason for the increases in taper angle may also be that the increased gap contributed to greater diffraction. These results ascertain that the gap has an influence on diffraction. Next, upside and downside widths and taper angle of the tapered groove at varying dose of X-ray was changed under the conditions of 7 μm slit width and 40 mm gap. Finally, slit widths was changed. These results suggest that varying the gap between X-ray mask and resist structure and slit width has a substantial effect on controlling taper angle.

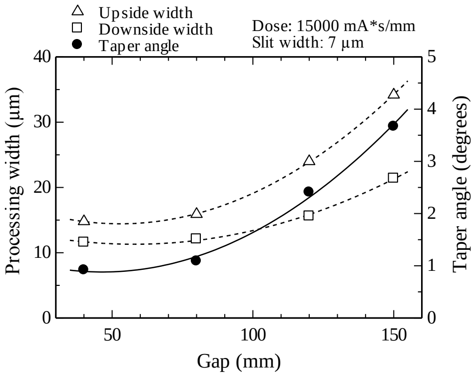

Fig. 2: *Dependence of gap on processing widths and taper angle*

We fabricated Ni mold with taper angle of about 2.5 degrees using electroforming. We used a nickel sulfamate plating bath to transfer the master mold shape by Ni electroforming because of high speed electroforming with lower electro-deposition stress generation. The fabricated Ni mold was about 1 mm in thickness and 40 mm × 45 mm size. Therefore, we could obtain Ni mold of partially copy the master pattern.

Conclusions

Removing a cast from a mold in molding of the LIGA process, especially in the case of a high aspect ratio microstructure, requires an elaborate design. Otherwise, it is impossible to remove the cast without breaking the micro structure. The mold releasing property of a structure improves if the micro structure has tapered. In this study, high aspect ratio tapered micro structures were fabricated using the NewSUBARU BL2 owned by our University for X-ray lithography involving diffraction.

Changes in top and bottom widths and taper angle of tapered grooves were measured at varying gaps, slit widths and dose of X-ray. At an increased dose of X-ray, processing width increased, while no significant changes were observed in taper angle. Furthermore, it was possible to achieve a taper angle of 3.7 degrees under the conditions of 150 mm gap between X-ray mask and resist structure, 15,000 mA·s/mm dose of X-ray and 7 μm slit width.

With the taper angle of 2.5 degrees, we have fabricated a Ni mold by electroforming. In future, we intend to discover necessary conditions for achieving the target taper angle of 5 degrees, and to study relationships between tapered shapes and mold release property through electroforming and molding by the LIGA process.

References

[1] E. W. Becker, W. Ehrfeld, P. Hagmann, A. Maner and D. Munchmeyer, Microelecron. Eng., **4**, pp. 35-56 (1986).

[2] T. Tanaka, T. Nomura, Y. Funabiki, T. Kitadani, K. Idei, K. Yamashita, D. Noda and T. Hattori, Proceedings of the 2006 IEEE International Symposium on Micro-Nano Mechatronics and Human Science, Nagoya, Japan, pp. 480-485 (2006).

[3] Y. Sawa, K. Tanabiki, D. Noda, and T. Hattori, J. Solid Mech. Mater. Eng., **3**, 5, pp. 721-728 (2009).